Bifurcations of Stationary Solutions in an Interacting Pair of E-I Neural Fields[*]

Stefanos E. Folias[†] and G. Bard Ermentrout[†]

Abstract. Persistent activity has been identified as a neural correlate of working memory [J. M. Fuster and G. E. Alexander, *Science*, 173 (1971), pp. 652–654; S. Funahashi, C. J. Bruce, and P. S. Goldman-Rakic, *J. Neurophysiol.*, 61 (1989), pp. 331–349; P. S. Goldman-Rakic, *Neuron*, 14 (1995), pp. 477–485]. In neural field theory, stationary bumps are localized states of neural activity that have been used to model this persistent activity. In [S. E. Folias and G. B. Ermentrout, *Phys. Rev. Lett.*, 107 (2011), 228103], we proposed that the persistent activity may be modeled by interacting neural field layers which support persistent activity when each layer in isolation cannot. In this paper, we study the existence, linear stability, and bifurcations of various stationary bumps in a pair of Amari neural fields and in a pair of excitatory-inhibitory (E-I) neural fields on one-dimensional spatial domains. Both support stationary bumps composed of a bump in each layer with (i) identical profiles, (ii) identical centers but different profiles, and (iii) spatially offset centers, and we identify a direct relationship between the two models through the spatial structure of the eigenfunctions for the linearization of the neural field equations about a specific type of stationary bump. Traveling bumps, breathers, and other spatiotemporal phenomena are also found.

Key words. Wilson–Cowan equations, stationary bumps, pattern formation, neural field equations

AMS subject classifications. 37N25, 92B20, 35B36, 47N20, 34K21, 37G35, 35Q92

DOI. 10.1137/110860094

1. Introduction. Wilson–Cowan-type or neural field equations [44, 1, 35, 18, 19, 17, 13, 20] have been studied extensively in recent years; however, analytical treatments have mainly focused on models of one or more populations of neurons distributed across the same spatial domain or feature space. The prevalence of reciprocal connectivity between different layers, brain regions, or neuronal pools indicates that the analysis of *interacting* neural fields is an important direction in which to advance neural field theory. A limited number of studies have examined interacting neural fields. Traveling bumps were studied in a double-ring network driven by homogeneous inputs to two different pools of neurons in a model of the head-direction system [45]. Each "ring" is a single population distributed along a one-dimensional periodic domain introduced in [30] as a reduction of the two-population excitatory-inhibitory (E-I) ring model [6]. Stationary bumps induced by localized inputs in a double-ring network [34] and traveling fronts on a pair of infinite lines [10] were studied in a pair of neural fields with synaptic depression to model left-eye/right-eye ocular dominance regions in a layer of visual cortex. See also [8, 9].

In this paper, we systematically study the existence and stability of various types of stationary bumps in an interacting pair of E-I neural fields and consider (i) a pair of E-I

[†]Department of Mathematics, University of Pittsburgh, Pittsburgh, PA (stefanos@pitt.edu, bard@pitt.edu).
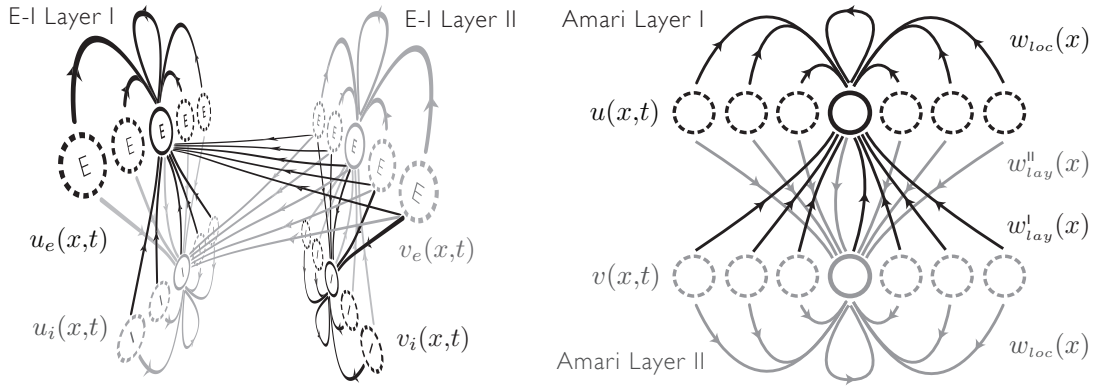
Figure 1. *Two classes of networks for an interacting pair of excitatory-inhibitory (E-I) neural fields. Left: A pair of E-I layers, each containing both E and I populations of mutually connected neurons. The two E-I layers interact through interlayer synaptic connections that project from the E population in each layer to both E and I populations in the opposite layer (connections from Layer II to Layer I shown only for clarity). Right: A pair of interacting Amari layers where excitation and inhibition are represented effectively through the weight function w_{loc} governing the local connections within each layer; the layers interact through interlayer synaptic connections w_{lay}^{I} and w_{lay}^{II}. Thus, each one-population "Amari layer" in the interacting pair of Amari layers effectively represents each two-population E-I layer in the interacting pair of E-I layers. Adapted from Folias & Ermentrout, Phys. Rev. Lett., 107 (2011), 228103. © 2011 by the American Physical Society.*

neural fields and (ii) the reduction to a pair of Amari neural fields, each representing the E and I dynamics effectively in a single population [1]. Some of the results herein have appeared previously in [24], where, as an application, we proposed that interacting activity bumps maintained by active *interlayer* connections between the layers could, on one hand, be representative of the persistent activity during working memory tasks and, on the other hand, explain why bumps are not typically seen in in vitro slice preparations. In vivo studies show that a number of different brain regions concurrently exhibit persistent activity during working memory tasks including prefrontal cortex [27, 25, 26], parietal cortex [12, 11], thalamus [28], caudate nucleus [33], and globus pallidus [40]. Other computational studies have examined interacting layers for the initiation or maintenance of persistent activity in working memory, e.g., [5, 4, 43]; however, modeling with neural fields treats the persistent activity as localized bumps whose existence and stability can be studied analytically [35, 42, 38, 7, 24, 21].

An interacting pair of E-I neural fields. We introduce a model for an *interacting pair of E-I neural fields*, as depicted in Figure 1 (left),

$$
\begin{array}{ll}
\text{(Layer I)} & \begin{aligned}
\tau_e \partial_t u_e &= -u_e + \left[w_{ee}^{loc} * f_e(u_e) - w_{ei}^{loc} * f_i(u_i) \right] + \left[w_{ee}^{lay} * f_e(v_e) \right], \\
\tau_i \partial_t u_i &= -u_i + \left[w_{ie}^{loc} * f_e(u_e) - w_{ii}^{loc} * f_i(u_i) \right] + \left[w_{ie}^{lay} * f_e(v_e) \right],
\end{aligned}
\end{array}
$$

(1)

$$
\begin{array}{ll}
\text{(Layer II)} & \begin{aligned}
\tau_e \partial_t v_e &= -v_e + \left[w_{ee}^{loc} * f_e(v_e) - w_{ei}^{loc} * f_i(v_i) \right] + \left[w_{ee}^{lay} * f_e(u_e) \right], \\
\tau_i \partial_t v_i &= -v_i + \left[w_{ie}^{loc} * f_e(v_e) - w_{ii}^{loc} * f_i(v_i) \right] + \left[w_{ie}^{lay} * f_e(u_e) \right],
\end{aligned}
\end{array}
$$

where $\left(w * f(u) \right)(x,t) = \int_{\mathbb{R}} w(x-y) f\left(u(y,t) \right) dy$, which describes the evolution of the activity

$(u_e, u_i)^{\mathrm{T}}$ and $(v_e, v_i)^{\mathrm{T}}$ along a pair of one-dimensional layers of neural tissue ($x \in \mathbb{R}$), each composed of an E-I pair of populations, respectively. The layers are governed by *local* (*loc*) synaptic connections and interact through *interlayer* (*lay*) synaptic connections given by the synaptic weight functions w_{uv}^l for $u,v \in \{e,i\}, l \in \{loc, lay\}$, which are assumed to be distance dependent, i.e., even-symmetric and homogeneous (having a translationally invariant spatial profile). The two E-I layers have identical *local* (or *intra*layer) connectivity within each layer, and, although the *interlayer* connections between the layers generally can differ, we restrict our analysis in the E-I model to the case of *reciprocally symmetric* interlayer coupling where they are identical. We take firing rate functions f_e and f_i to be Heaviside functions with thresholds θ_e and θ_i, respectively, and, in the absence of interlayer coupling, each isolated E-I neural field (local connections only) thus reduces to the form studied in [7].

An interacting pair of Amari neural fields. The pair of E-I neural fields (1) naturally reduces to an *interacting pair of Amari neural fields* $(u(x,t), v(x,t))^{\mathrm{T}}$ evolving according to

(2)
$$\begin{aligned} \text{(Layer I)} \qquad & \tau \partial_t u = -u + w_{loc} * f(u) + w_{lay}^{\mathrm{I}} * f(v), \\ \text{(Layer II)} \qquad & \tau \partial_t v = -v + w_{loc} * f(v) + w_{lay}^{\mathrm{II}} * f(u). \end{aligned}$$

$f(u) = H(u - \theta)$ is a Heaviside function with firing threshold θ. Depicted in Figure 1 (right), the activity $(u, v)^{\mathrm{T}}$ in the pair of one-dimensional neural layers ($x \in \mathbb{R}$) is governed by local (*intralayer*) synaptic connections w_{loc} and *interlayer* projections w_{lay}^{I} and w_{lay}^{II}, which can be either *reciprocally symmetric* ($w_{lay}^{\mathrm{I}} \equiv w_{lay}^{\mathrm{II}} \equiv w_{lay}$) or *reciprocally asymmetric* ($w_{lay}^{\mathrm{I}} \neq w_{lay}^{\mathrm{II}}$). The following assumptions [41, 42] reduce a single E-I neural field ($w_{ee}^{lay} = w_{ie}^{lay} = 0$) to an Amari neural field ($w_{lay}^{\mathrm{I}} = w_{lay}^{\mathrm{II}} = 0$) [1]: (i) the I population is in quasisteady state relative to the E population ($\tau_i = 0$), (ii) no I-to-I coupling ($w_{ii}^{loc} = 0$), (iii) a linear firing rate for the I population ($f_i(u_i) = u_i$) and a Heaviside firing rate for the E population ($f_e(u_e) = H(u_e - \theta)$). The pair of E-I neural fields (1) analogously reduces to (2) with $u = u_e$, $v = v_e$, $\tau = \tau_e$,

$$w_{loc} = w_{ee}^{loc} - w_{ei}^{loc} * w_{ie}^{loc}, \qquad w_{lay} = w_{ee}^{lay} - w_{ei}^{loc} * w_{ie}^{lay}.$$

Organization of the paper. In section 2, we study stationary solutions in the interacting pair of Amari neural fields (2) and discuss solitary bumps in section 2.1 and periodic bumps in section 2.2. Generally we assume the case of reciprocally symmetric interlayer coupling ($w_{lay}^{\mathrm{I}} = w_{lay}^{\mathrm{II}} = w_{lay}$); however, in section 2.1.3, we additionally consider solitary bumps in the case of reciprocally asymmetric interlayer coupling ($w_{lay}^{\mathrm{I}} \neq w_{lay}^{\mathrm{II}}$). Note that these results also extend to the case of periodic bumps, though we have omitted them here for brevity. In section 3, we consider the existence and linear stability of stationary bumps in the pair of interacting E-I neural fields in (1) with Heaviside firing rates and demonstrate that various bifurcations of these bumps give rise to different types of solutions which have relationships to solutions in the interacting pair of Amari neural fields (2) with Heaviside firing rate. Finally, in section 3.3, we demonstrate, in a *single* E-I neural field layer, that it is possible for a stable stationary bump to exist in the case that the spatial extent of the excitatory connections exceeds that of the inhibitory connections and, furthermore, where the effective Amari weight function $w_{loc} = w_{ee}^{loc} - w_{ei}^{loc} * w_{ie}^{loc}$ is not of Mexican hat form, i.e., in a nonlateral inhibition regime. In the single-layer Amari neural field, lateral inhibition is necessary to stabilize a stationary bump. Although lateral inhibition in the single E-I neural field layer helps to

stabilize a stationary bump, this result shows (in two senses) that lateral inhibition is, in fact, *not* necessary to stabilize a stationary bump. Additionally, we describe another unstable solution, a superthreshold bump in the excitatory population only, and mention how this type of solution can extend in three ways to the pair of interacting E-I neural fields.

2. An interacting pair of Amari neural fields. With the exception of subsection 2.1.3, in section 2 we consider an interacting pair of identical Amari neural field layers (2) with *reciprocally symmetric* interlayer synaptic coupling ($w_{lay}^{I} = w_{lay}^{II} = w_{lay}$),

$$
(3) \qquad
\begin{aligned}
\tau \partial_t u &= -u + w_{loc} * H(u - \theta) + w_{lay} * H(v - \theta), \\
\tau \partial_t v &= -v + w_{loc} * H(v - \theta) + w_{lay} * H(u - \theta),
\end{aligned}
$$

defined for x along the infinite line. The Heaviside firing rate has firing threshold θ, and, without loss of generality, we set $\tau = 1$. The two classes of solutions of (3) we study are stationary *solitary* bumps in section 2.1 and stationary *periodic* bumps in section 2.2. In section 2.1.3 we study (2) in the case of reciprocally *asymmetric* interlayer connections as indicated in (22). We mention that elements of section 2.1 have appeared previously in [24], and the analysis of a *syntopic bump with equal widths* is presented here in full as it is both a central result and a simplest case that extends directly to the analogous results for the other types of stationary bumps studied herein. New results for this case have also been included.

Synaptic weight functions. The distance-dependent synaptic weight functions w_{loc}, w_{lay} are assumed to be even-symmetric and homogeneous (i.e., translationally invariant) in each one-dimensional layer ($x \in \mathbb{R}$), with $w_{loc}(x), w_{lay}(x) \to 0$ as $x \to \infty$. We generally assume local synaptic connections w_{loc} of Mexican hat form (see Figure 4(IV); negative and positive values effectively represent the net distribution of local excitatory and inhibitory connections within the layer); however, as a special case in Figure 3(b), we consider an inverted Mexican hat of the form in Figure 4(III). For interlayer connections w_{lay}, we allow both excitatory (positive) weight functions and variants of the Mexican hat–type weight functions (see Figure 4). In subsection 2.1.3, we relax the restriction to reciprocal symmetry in the interlayer connections and consider a special subclass of *reciprocally asymmetric* interlayer coupling ($w_{lay}^{I} \neq w_{lay}^{II}$).

The interlayer synaptic coupling determines a relationship between the coordinate systems for each layer; we define a *universal coordinate system* for both layers (i) using the local connections to determine the length scale in each layer and (ii) using the center point of the even-symmetric interlayer weight functions to identify the origin in Layer II based on the connections to the origin in Layer I and vice-versa. For numerical calculations and simulations, we take the local and interlayer synaptic connections to be of the form

$$
(4) \qquad w_l(x) = \frac{A_l^e}{2\sigma_l^e} e^{-|x|/\sigma_l^e} - \frac{A_l^i}{2\sigma_l^i} e^{-|x|/\sigma_l^i}, \qquad l \in \{loc, lay\},
$$

which has the following useful integral (which is odd-symmetric since w_l is even):

$$
W_l(x) \equiv \int_0^x w_l(y)\, dy = \tfrac{1}{2} A_l^e \left(1 - e^{-x/\sigma_l^e} \right) - \tfrac{1}{2} A_l^i \left(1 - e^{-x/\sigma_l^i} \right), \qquad x \geq 0, \, l \in \{loc, lay\}.
$$

2.1. Stationary solitary bumps. We consider two types of stationary solutions for the pair of Amari layers (3) composed of a superthreshold solitary bump $u(x, t) = \mathcal{U}(x)$ in Layer I and $v(x, t) = \mathcal{V}(x)$ in Layer II with the activity patterns interacting through the interlayer coupling. Another type of stationary solution is composed of a stationary bump in only one of the two layers with subthreshold activity in the other layer. We omit details but mention that the point spectrum here reduces to that of a bump in the single Amari layer in isolation (see section 3.3 for a related analysis).

We introduce new terms for two types of stationary activity bumps that can be characterized by the spatial location of the activity bumps in each layer with respect to the universal coordinate system. We define the term *syntopic bump* to refer to a stationary solution in which a single or periodic stationary bump is present in each layer and shares a common center with respect to the universal coordinate system; the width of the bump in each layer need not be the same, and we consider the separate cases of *equal widths* and *different widths*. Based on the Greek roots *syn* and *topos* meaning *together in place*, the term *syntopic* is the spatial analogue of *synchronous*, which means *together in time*. Conversely, we define the term *allotopic bump*, based on the Greek root *allo* meaning *other*, to describe a solitary or periodic bump solution in which the bump(s) in each layer exist(s) in a different spatial location. Note that the terms *syntopic* and *allotopic* are used in biology, perhaps esoterically, to characterize, for example, (i) organisms which occupy the *same* or *different* microhabitats or (ii) the interaction of two drugs acting at the *same* or *different* sites on a receptor [29, 39].

In section 2.1.1, we study the existence and linear stability of syntopic bumps with equal widths in the reciprocally symmetric interacting pair of Amari layers (3) and demonstrate that they give rise to both (i) syntopic bumps with different widths and (ii) allotopic bumps as the result of pitchfork bifurcations with respect to two different eigenmodes of the linearization. In section 2.1.2, we develop the existence and linear stability analysis of allotopic bumps, and, in section 2.1.3, we extend the existence and stability of syntopic bumps to the case of reciprocally asymmetric interlayer coupling $(w_{lay}^{\mathsf{I}} \neq w_{lay}^{\mathsf{II}})$, in which a syntopic bump is composed of bumps that generically have different widths in the two layers.

2.1.1. Syntopic bumps. In this section, we examine the existence and linear stability of syntopic bumps in the interacting pair of Amari neural fields (3). We also discuss bifurcations of a syntopic bump (with equal widths) with respect to certain eigenmodes that give rise to new solutions: (i) a *syntopic bump with different widths* and (ii) an *allotopic bump*.

Existence of a syntopic bump with equal widths. For a syntopic bump, we assume $(u(x, t), v(x, t))^{\mathrm{T}} = (\mathcal{U}_s(x), \mathcal{V}_s(x))^{\mathrm{T}}$ with $\mathcal{U}_s(x) = \mathcal{V}_s(x)$ satisfying the threshold conditions

$$(5) \qquad \mathcal{U}_s(0) = \mathcal{V}_s(0) = \theta, \qquad \mathcal{U}_s(a) = \mathcal{V}_s(a) = \theta$$

that determine the *syntopic bump width a*, and we require that

$$\mathcal{U}_s(x), \mathcal{V}_s(x) > \theta, \quad x \in (0, a), \qquad \mathcal{U}_s(x), \mathcal{V}_s(x) < \theta \quad \text{otherwise,}$$

with $\mathcal{U}_s(x), \mathcal{V}_s(x) \longrightarrow 0$ as $x \to \pm\infty$. Setting the time derivatives to 0 in (3) and assuming
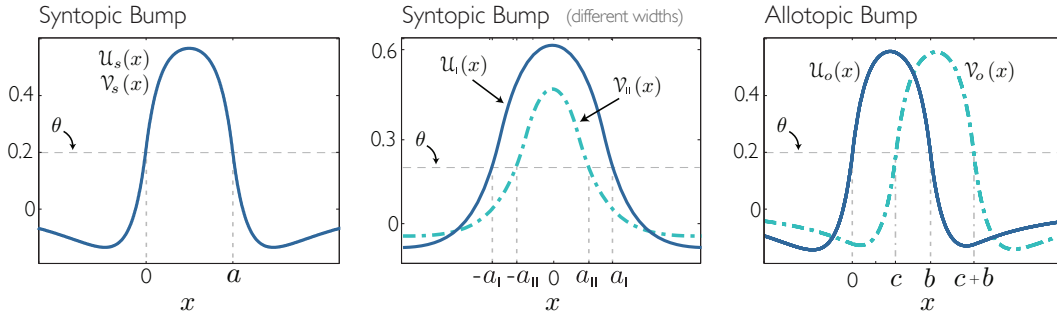
Figure 2. *Stationary bumps $(u(x,t), v(x,t))^{\mathrm{T}} = (\mathcal{U}(x), \mathcal{V}(x))^{\mathrm{T}}$ in the pair of Amari neural fields (3). Left: A "syntopic bump with equal widths" $(\mathcal{U}_s(x), \mathcal{V}_s(x))^{\mathrm{T}}$ satisfying $\mathcal{V}_s(x) = \mathcal{U}_s(x)$ is characterized as a stationary bump in each layer, with bump width a, sharing the same center. Parameters: $A^e_{lay} = 0.5, \sigma^e_{lay} = 2.2, A^i_{lay} = 0.4, a = 5.7$. Middle: A "syntopic bump with different widths" $(\mathcal{U}_{\mathrm{I}}(x), \mathcal{V}_{\mathrm{II}}(x))^{\mathrm{T}}$ where the bump in each layer shares the same center but has different halfwidths a_{I} and a_{II} in Layers I and II, respectively. Parameters: $A^e_{lay} = 0.6, \sigma^e_{lay} = 1.6, A^i_{lay} = 0.8, a_{\mathrm{I}} = 1.72, a_{\mathrm{II}} = 0.86$. This type of bump can bifurcate from the syntopic bump in a pitchfork bifurcation with respect to a particular eigenmode of the linearization and is generally found to be unstable. Right: An "allotopic bump" $(\mathcal{U}_o(x), \mathcal{V}_o(x))^{\mathrm{T}}$ where the bumps in each layer have width b and are spatially offset with distance c. This solution bifurcates from the syntopic bump in a pitchfork bifurcation with respect to a different eigenmode. Parameters: $A^e_{lay} = 0.5, \sigma^e_{lay} = 2.6, A^i_{lay} = 0.4, b = 5.16, c = 3.35$. Fixed parameters common to all panels: $A^e_{loc} = \sigma^e_{loc} = A^i_{loc} = 1, \sigma^i_{loc} = 5, \sigma^i_{lay} = 2, \theta = 0.2$. The figure is adapted from Folias and Ermentrout, Phys. Rev. Lett., 107 (2011), 228103. © 2011 by the American Physical Society.*

$\mathcal{U}_s(x) = \mathcal{V}_s(x)$ satisfies (5), the *profile* of the stationary syntopic bump is expressed as

$$(6) \qquad \mathcal{U}_s(x) = \Big[W_{loc}(x) - W_{loc}(x-a)\Big] + \Big[W_{lay}(x) - W_{lay}(x-a)\Big]$$

$$(7) \qquad \Rightarrow \quad \mathcal{U}'_s(x) = \Big[w_{loc}(x) - w_{loc}(x-a)\Big] + \Big[w_{lay}(x) - w_{lay}(x-a)\Big].$$

Threshold compatibility conditions (5) guarantee the existence of a syntopic bump if

$$(8) \qquad \theta = W_{loc}(a) + W_{lay}(a)$$

provided the solution $\mathcal{U}_s(x) \equiv \mathcal{V}_s(x)$ crosses threshold θ only at $x = 0$ and $x = a$.

Existence of syntopic bumps with different widths. The reciprocally symmetric pair of interacting Amari equations (3) additionally support syntopic bumps where the bump in each layer has a different width (but the same center). Here it is more convenient to take the syntopic bump to be centered about the origin (see Figure 2). Let a_{I} and a_{II} denote the *halfwidths* of the stationary bump in Layer I and Layer II, respectively. Existence for this class of syntopic bumps is given as a special case of condition (26) in section 2.1.3 for an interacting pair of Amari layers with asymmetric interlayer coupling by setting $W^{\mathrm{I}}_{lay} \equiv W^{\mathrm{II}}_{lay} \equiv W_{lay}$ and $a_{\mathrm{I}} \neq a_{\mathrm{II}}$. Consequently, the existence condition for a syntopic bump with different widths is

$$(9) \qquad \begin{aligned} \theta &= W_{loc}(2a_{\mathrm{I}}) + W_{lay}(a_{\mathrm{I}} + a_{\mathrm{II}}) - W_{lay}(a_{\mathrm{I}} - a_{\mathrm{II}}), \\ \theta &= W_{loc}(2a_{\mathrm{II}}) + W_{lay}(a_{\mathrm{I}} + a_{\mathrm{II}}) + W_{lay}(a_{\mathrm{I}} - a_{\mathrm{II}}) \end{aligned}$$

provided the bumps in each layer satisfy the threshold behavior described in section 2.1.3. An explicit formula for the profile $(u(x,t), v(x,t))^{\mathrm{T}} = (\mathcal{U}_{\mathrm{I}}(x), \mathcal{U}_{\mathrm{II}}(x))^{\mathrm{T}}$ of the syntopic bump
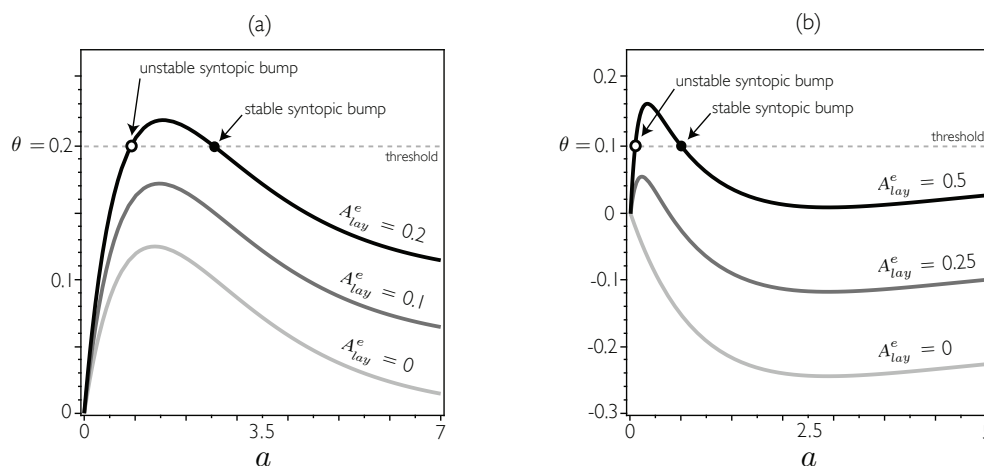
Figure 3. *Saddle-node bifurcation for a syntopic bump (with equal widths). The panels show plots of $\Theta(a) \equiv W_{loc}(a) + W_{lay}(a)$ in (8) for various values of A^e_{lay} with $A^i_{lay} = 0$ for the local and interlayer weight functions of the form (4); intersection points with θ indicate solutions of the existence equation (8). Setting $A^e_{lay} = 0$ causes the Amari layers to decouple, and no stable stationary bumps exist for $\theta = 0.2$. Increasing the excitatory interlayer coupling strength $A^e_{lay} > 0$ leads to a saddle-node bifurcation of syntopic bumps, and, in this case, the larger syntopic bump that emerges is stable (from linear stability analysis). As A^e_{lay} increases further through 0.4, the width of the stable syntopic bump becomes infinite, corresponding to the uniform excited state. In the two panels (a) w_{loc} is of Mexican hat form (see Figure 4(IV)), and parameters are $A^e_{loc} = A^i_{loc} = \sigma^e_{loc} = 1, \sigma^i_{loc} = 2, A^i_{lay} = 0, \sigma^e_{lay} = 0.5, \theta = 0.2$, and (b) w_{loc} is an inverted Mexican hat (see Figure 4(III)), and parameters are $A^e_{loc} = 0.25, A^i_{loc} = 0.7, \sigma^e_{loc} = 4, \sigma^i_{loc} = 1, A^i_{lay} = 0, \sigma^e_{lay} = 0.1, \theta = 0.1$. Panel (a) appeared in Folias & Ermentrout, Phys. Rev. Lett., 107 (2011), 228103. © 2011 by the American Physical Society.*

with differing widths is given in (24)–(25) with $W^{\mathrm{I}}_{lay} \equiv W^{\mathrm{II}}_{lay} \equiv W_{lay}$. The solutions, which are discussed below in Figure 6, were generally found to be unstable and can serve as separatrices in the flow, e.g., separating trajectories that approach rest or a solution composed of a single bump in one layer and subthreshold activity in the other layer. Such a solution arises, for example, when each layer can support a bump in isolation and when a bump in one layer can exist without necessarily generating superthreshold activity in the other layer. Note that equations (9) reduce to (8) for the *syntopic bump with equal widths* if $a_{\mathrm{I}} \equiv a_{\mathrm{II}} \equiv a/2$.

Saddle-node bifurcation of syntopic bumps with equal widths. Given the number of parameters in (3), a variety of scenarios lead to the existence of a stationary syntopic bump. We concentrate on an important extension of bumps in a single Amari layer [1] and consider the case in which the local Mexican hat connections w_{loc} in each Amari layer in (3) do *not* support a stationary bump solution (with $w_{lay} = 0$) so that $W_{loc}(a) < \theta$ for all $a > 0$. It is possible to overcome the deficiency in the local excitation by engaging the excitatory interlayer connections ($w_{lay} > 0$) as demonstrated in Figure 3. Furthermore, we demonstrate this in two different cases of local connections w_{loc} which in Figure 3(a) are of Mexican hat form (as shown in Figure 4(IV)) and in Figure 3(b) are of the form shown in Figure 4(III). Activity must be present in each layer to engage these interlayer connections, and the existence of the bump depends on the presence of active interlayer connections; the syntopic bump decays to rest when the interlayer connections are removed in simulations.

In a scenario that contrasts the above, the parameters for the local connections can be chosen such that each Amari layer in isolation supports a stable bump. Inclusion of interlayer connections leads to a variety of scenarios regarding the existence of syntopic bumps and bumps only in one layer. If the interlayer connections are sufficiently weak, it is possible to have a stationary bump in one layer without necessarily exciting the other layer. If a stable syntopic bump coexists, then different sets of initial conditions can approach the two solutions.

Linear stability of a syntopic bump with equal widths. To study the linear stability of the syntopic bump $(\mathcal{U}_s, \mathcal{V}_s)^{\mathrm{T}}$ with equal widths, where $\mathcal{V}_s(x) = \mathcal{U}_s(x)$, we consider the evolution of arbitrary, small perturbations $(\tilde{\varphi}, \tilde{\psi})^{\mathrm{T}}$ to the bump by setting

$$u(x,t) = \mathcal{U}_s(x) + \tilde{\varphi}(x,t), \qquad v(x,t) = \mathcal{V}_s(x) + \tilde{\psi}(x,t).$$

Linearizing about the syntopic bump, the perturbations evolve at linear order according to

$$(10) \qquad
\begin{aligned}
\partial_t \tilde{\varphi} &= -\tilde{\varphi} + w_{loc} * \big[\, \delta(\mathcal{U}_s - \theta)\,\tilde{\varphi}\,\big] + w_{lay} * \big[\, \delta(\mathcal{V}_s - \theta)\,\tilde{\psi}\,\big], \\
\partial_t \tilde{\psi} &= -\tilde{\psi} + w_{loc} * \big[\, \delta(\mathcal{V}_s - \theta)\,\tilde{\psi}\,\big] + w_{lay} * \big[\, \delta(\mathcal{U}_s - \theta)\,\tilde{\varphi}\,\big].
\end{aligned}$$

Separating variables $\tilde{\varphi}(x,t) = \varphi(x)e^{\lambda t}$ and $\tilde{\psi}(x,t) = \psi(x)e^{\lambda t}$, we obtain the spectral problem

$$(11) \qquad
\begin{aligned}
\lambda \varphi &= -\varphi + \mathcal{N}_{loc}[\mathcal{U}_s]\,\varphi + \mathcal{N}_{lay}[\mathcal{U}_s]\,\psi, \\
\lambda \psi &= -\psi + \mathcal{N}_{loc}[\mathcal{U}_s]\,\psi + \mathcal{N}_{lay}[\mathcal{U}_s]\,\varphi
\end{aligned}$$

for λ and $(\varphi(x), \psi(x))^{\mathrm{T}}$, where the operator $\mathcal{N}_l[\mathcal{U}]$ is given, for $l \in \{loc, lay\}$, by

$$(12) \qquad
\begin{aligned}
\mathcal{N}_l[\mathcal{U}]\,\phi\,(x) &= w_l * \Big[\delta(\mathcal{U} - \theta)\,\phi\Big](x) = \int_{\mathbb{R}} w_l(x-y)\,\delta\big(\mathcal{U}(y) - \theta\big)\,\phi(y)\,dy \\
&= \frac{w_l(x - a_{\mathrm{L}})}{|\mathcal{U}'(a_{\mathrm{L}})|}\,\phi(a_{\mathrm{L}}) + \frac{w_l(x - a_{\mathrm{R}})}{|\mathcal{U}'(a_{\mathrm{R}})|}\,\phi(a_{\mathrm{R}})
\end{aligned}$$

and the stationary bump $\mathcal{U}(x) > \theta$ for $x \in (a_{\mathrm{L}}, a_{\mathrm{R}})$. Since $\mathcal{N}_{loc}$ and $\mathcal{N}_{lay}$ are compact operators, the essential spectrum is given by $\lambda = -1 < 0$ and does not give rise to instability. Moreover, all linearizations in section 2 have the same essential spectrum, and, since it plays no role in instability, we omit further mention of this. From symmetry conditions, $|\mathcal{U}_s'(0)| = |\mathcal{U}_s'(a)|$, which is calculated from (7) to be

$$(13) \qquad \mathcal{U}_s'(0) = \big[w_{loc}(0) - w_{loc}(a)\big] + \big[w_{lay}(0) - w_{lay}(a)\big] > 0.$$

To simplify notation we define $\hat{w}_l(x) = w_l(x)/|\mathcal{U}_s'(0)|$. Consequently, the point spectrum of (11) comprises eigenvalues λ associated with eigenfunctions $(\varphi(x), \psi(x))^{\mathrm{T}}$ satisfying

$$\begin{aligned}
\lambda \varphi(x) &= -\varphi(x) + \big[\hat{w}_{loc}(x)\varphi(0) + \hat{w}_{loc}(x-a)\varphi(a)\big] + \big[\hat{w}_{lay}(x)\psi(0) + \hat{w}_{lay}(x-a)\psi(a)\big], \\
\lambda \psi(x) &= -\psi(x) + \big[\hat{w}_{loc}(x)\psi(0) + \hat{w}_{loc}(x-a)\psi(a)\big] + \big[\hat{w}_{lay}(x)\varphi(0) + \hat{w}_{lay}(x-a)\varphi(a)\big].
\end{aligned}$$

Setting $x = 0$ and $x = a$ in the above system yields the compatibility condition

$$(14) \qquad \big(\mathrm{M}_s - \mathrm{I}_4\big)\boldsymbol{v} = \lambda \boldsymbol{v}$$

for λ and $\boldsymbol{v} = (\varphi(0), \varphi(a), \psi(0), \psi(a))^{\mathrm{T}}$, where I_4 denotes the 4×4 identity and

$$
\mathrm{M}_s(a) = \begin{bmatrix} \hat{w}_{loc}(0) & \hat{w}_{loc}(a) & \hat{w}_{lay}(0) & \hat{w}_{lay}(a) \\ \hat{w}_{loc}(a) & \hat{w}_{loc}(0) & \hat{w}_{lay}(a) & \hat{w}_{lay}(0) \\ \hat{w}_{lay}(0) & \hat{w}_{lay}(a) & \hat{w}_{loc}(0) & \hat{w}_{loc}(a) \\ \hat{w}_{lay}(a) & \hat{w}_{lay}(0) & \hat{w}_{loc}(a) & \hat{w}_{loc}(0) \end{bmatrix}, \qquad \boldsymbol{v}(a) = \begin{pmatrix} \varphi(0) \\ \varphi(a) \\ \psi(0) \\ \psi(a) \end{pmatrix}.
$$

Using a similarity transformation, we express $\mathrm{Q}^{-1}(\mathrm{M}_s - \mathrm{I}_4)\mathrm{Q} = \Lambda_s$, where Λ_s is the block diagonal matrix shown below, the details of which are collected in Appendix A:

$$
\Lambda_s = \begin{bmatrix} \Lambda_+ & 0 \\ 0 & \Lambda_- \end{bmatrix}, \qquad \Lambda_\pm = \begin{bmatrix} -1 + \hat{w}_{loc}(0) \pm \hat{w}_{loc}(a) & \hat{w}_{lay}(0) \pm \hat{w}_{lay}(a) \\ \hat{w}_{lay}(0) \pm \hat{w}_{lay}(a) & -1 + \hat{w}_{loc}(0) \pm \hat{w}_{loc}(a) \end{bmatrix}.
$$

The eigenvalues of $(\mathrm{M}_s - \mathrm{I}_4)$ and Λ_s are the same and are given by $\lambda_\pm^+(a)$ and $\lambda_\pm^-(a)$, where

(15)
$$
\begin{aligned}
\lambda_\pm^+(a) &= -1 + \left[\hat{w}_{loc}(0) + \hat{w}_{loc}(a)\right] \pm \left[\hat{w}_{lay}(0) + \hat{w}_{lay}(a)\right], \\
\lambda_\pm^-(a) &= -1 + \left[\hat{w}_{loc}(0) - \hat{w}_{loc}(a)\right] \pm \left[\hat{w}_{lay}(0) - \hat{w}_{lay}(a)\right].
\end{aligned}
$$

From $\hat{w}_l(x) = w_l(x)/|\mathcal{U}_s'(0)|$, with $\mathcal{U}_s'(0)$ given in (13), the 0 eigenvalue is revealed,

$$
\lambda_+^-(a) = -1 + \frac{1}{|\mathcal{U}_s'(0)|}\left(\left[w_{loc}(0) - w_{loc}(a)\right] + \left[w_{lay}(0) - w_{lay}(a)\right]\right) = 0,
$$

and reflects the translation invariance of the syntopic bump. Setting $\gamma(a) = |\mathcal{U}_s'(0)|$, which is calculated in (13), the other eigenvalues can be expressed accordingly as

$$
\lambda_+^+(a) = \tfrac{2}{\gamma}\left(w_{loc}(a) + w_{lay}(a)\right), \qquad \lambda_-^+(a) = \tfrac{2}{\gamma}\left(w_{loc}(a) - w_{lay}(0)\right),
$$

$$
\lambda_+^-(a) = 0, \qquad\qquad \lambda_-^-(a) = -\tfrac{2}{\gamma}\left(w_{lay}(0) - w_{lay}(a)\right).
$$

The associated eigenfunctions are calculated and collected in Appendix A.

In all cases, since $\gamma > 0$, stability of the stationary syntopic bump requires

$$
w_{loc}(a) < -w_{lay}(a), \qquad w_{loc}(a) < w_{lay}(0), \qquad w_{lay}(a) < w_{lay}(0).
$$

Condition $\lambda_+^+ < 0$ implies $w_{loc}(a) + w_{lay}(a) < 0$, which means that stable stationary bumps do not exist in the case where both of the local and interlayer synaptic connections are purely excitatory $(w_{loc}(x) > 0, w_{lay}(x) > 0)$.

Example of analysis used to compile Table 1. Assume the interlayer connections are purely excitatory $(w_{lay}(x) > 0)$, even-symmetric, and monotonically decreasing for $x > 0$. Since $w_{lay}(a) < w_{lay}(0)$ and $\gamma > 0$, it follows that $\lambda_-^- < 0$ is automatically satisfied. Furthermore, $\lambda_-^+ < 0$ is redundant since it is superseded by $\lambda_+^+ < 0$ (since $-w_{lay}(a) < 0 < w_{lay}(0)$). Thus, stability of the syntopic bump reduces to the condition $\lambda_+^+ < 0$. (Full analysis omitted.)

Saddle-node bifurcation of syntopic bumps with equal widths ($\lambda_+^+ = 0$). In Figure 3, a pair of syntopic bumps emerges when the function $\Theta(a) = W_{loc}(a) + W_{lay}(a)$ forms a
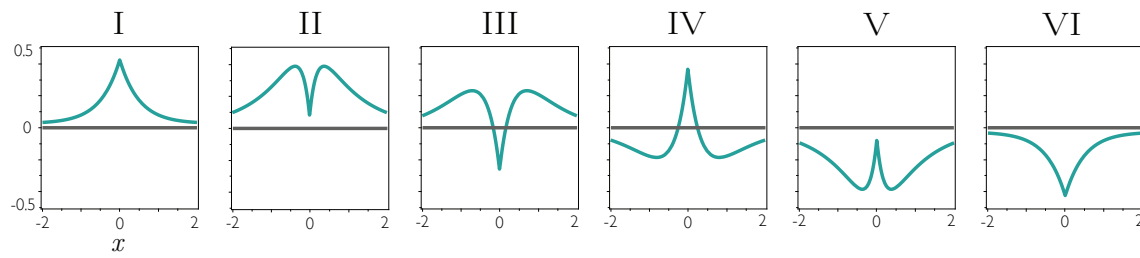
Figure 4. *Various types of even-symmetric profiles for the synaptic weight functions $w_{loc}(x)$ and $w_{lay}(x)$ which can be generated by* (4). *Regions above the horizontal are positive and represent net excitatory connections; regions below the horizontal are negative, representing net inhibitory connections. We assume that $w_l(x) > 0$ in cases* I *and* II *and* $w_l(x) < 0$ *in cases* V *and* VI; *the only two zero-crossings of* w_l *are shown in cases* III *and* IV *where* $\iota \in \{loc, lay\}$.

Table 1
We characterize which eigenvalues determine the linear stability of the stationary bump according to the profile of the weight functions $w_{loc}(x)$ and $w_{lay}(x)$ for the different types shown in Figure 4. *The numerals along the side of the table denote the* local *weight function $w_{loc}(x)$, and the numerals along the* top *of the table denote the* interlayer *weight function $w_{lay}(x)$. In each table element, the statement in the first row lists definitive inequalities for particular eigenvalues, and the second row lists the one or two eigenvalues that control the stability of the syntopic bump. If one eigenvalue is positive, the syntopic syntopic bump is unstable and such cases are simply labeled* UNSTABLE. *If both weight functions are purely negative, stationary bumps necessarily do not exist and such cases are labeled* NO BUMPS.

Eigenvalues and stability of the syntopic bump for different weight functions					
	I	II	III	IV	V	VI
I	$\lambda^+_+>0$ UNSTABLE	$\lambda^+_+>0$ UNSTABLE	$\lambda^-_->0$ UNSTABLE	$\lambda^-_-<0$ λ^+_+,λ^-_-	$\lambda^+_->\lambda^+_+$ λ^+_-,λ^-_-	$\lambda^+_->0,\lambda^-_->0$ UNSTABLE
II	$\lambda^+_+>0$ UNSTABLE	$\lambda^+_+>0$ UNSTABLE	$\lambda^-_->0$ UNSTABLE	$\lambda^-_-<0$ λ^+_+,λ^-_-	$\lambda^+_->\lambda^+_+$ λ^+_-,λ^-_-	$\lambda^+_->0,\lambda^-_->0$ UNSTABLE
III	$\lambda^-_-<0,\lambda^+_+>\lambda^+_-$ λ^+_+	$\lambda^+_+>\lambda^+_-$ λ^+_+,λ^-_-	$\lambda^-_->0$ UNSTABLE	$\lambda^-_-<0$ λ^+_+,λ^-_-	$\lambda^+_->\lambda^+_+$ λ^+_-,λ^-_-	$\lambda^-_->0$ UNSTABLE
IV	$\lambda^-_-<0,\lambda^+_+>\lambda^+_-$ λ^+_+	$\lambda^+_+>\lambda^+_-$ λ^+_+,λ^-_-	$\lambda^-_->0$ UNSTABLE	$\lambda^-_-<0$ λ^+_+,λ^-_-	$\lambda^+_->\lambda^+_+$ λ^+_-,λ^-_-	$\lambda^-_->0$ UNSTABLE
V	$\lambda^-_-<0,\lambda^+_+>\lambda^+_-$ λ^+_+	$\lambda^+_+>\lambda^+_-$ λ^+_+,λ^-_-	$\lambda^-_->0$ UNSTABLE	$\lambda^-_-<0$ λ^+_+,λ^-_-	NO BUMPS	NO BUMPS
VI	$\lambda^-_-<0,\lambda^+_+>\lambda^+_-$ λ^+_+	$\lambda^+_+>\lambda^+_-$ λ^+_+,λ^-_-	$\lambda^-_->0$ UNSTABLE	$\lambda^-_-<0$ λ^+_+,λ^-_-	NO BUMPS	NO BUMPS

tangency with the horizontal line $\Theta = \theta$. Since this is a local maximum of $\Theta(a)$, it follows that $\Theta'(a) = w_{loc}(a) + w_{lay}(a) = 0$; hence, $\lambda^+_+(a) = 0$ at the saddle-node bifurcation point.

Bifurcation to a syntopic bump with different widths ($\lambda^+_- = 0$). In the dual Amari layers (3), syntopic bumps with equal widths and those with different widths can coexist, and both types can emerge and vanish in saddle-node bifurcations. However, a syntopic bump with equal widths can also undergo a pitchfork bifurcation when $\lambda^+_- = 0$ and give rise to a pair of syntopic bumps with different widths. We now demonstrate this by showing (i) that perturbing
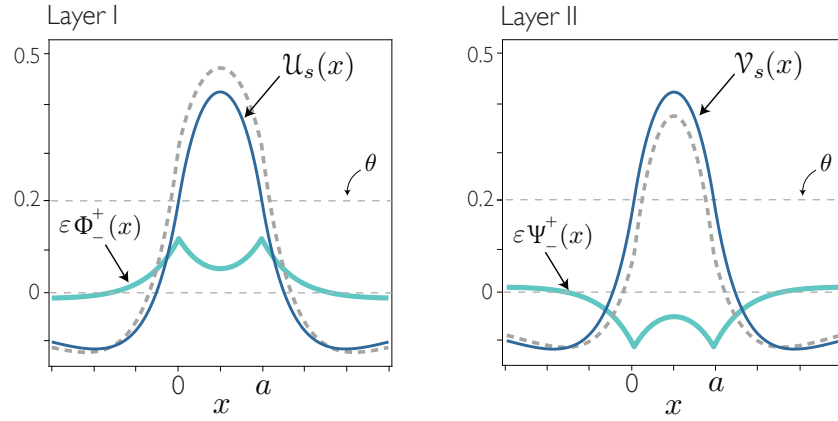
Figure 5. *At the pitchfork bifurcation point $(\sigma_{lay}^e, a) \approx (1.5, 2.5)$, where $\lambda_-^+(a) = 0$, the associated eigenfunction is represented by the light-colored solid curve in each layer, with component $\Phi_-^+(x)$ in Layer I and $\Psi_-^+(x)$ in Layer II, which have been additionally scaled by $\varepsilon = 0.1$. The darker solid curves represent the stationary syntopic bump $(\mathcal{U}_s(x), \mathcal{V}_s(x))^{\mathrm{T}}$ at the bifurcation point. The dashed gray curves in Layer I represent $\mathcal{U}_s(x) + \varepsilon \Phi_-^+(x)$, whereas the dashed gray curve in Layer II represents $\mathcal{V}_s(x) + \varepsilon \Psi_-^+(x)$. The dashed gray curves illustrate that a small perturbation with respect to the eigenfunction $(\Phi_-^+(x), \Psi_-^+(x))^{\mathrm{T}}$ leads to an even-symmetric enhancement (reduction) of the bump in Layer I (Layer II). For this set of parameter values in (3) with reciprocally symmetric interlayer connections, the pitchfork bifurcation is subcritical as indicated both by numerical simulations of (3) as well as numerically solving the existence equations (9) for a syntopic bump with different widths. Fixed parameters: $A_{loc}^e = \sigma_{loc}^e = A_{loc}^i = 1, \sigma_{loc}^i = 5, A_{lay}^e = 0.55, A_{lay}^i = 0.8, \sigma_{lay}^i = 2, \theta = 0.2$.*

with respect to the eigenfunction $(\Phi_-^+(x), \Psi_-^+(x))^{\mathrm{T}}$ that destabilizes in the bifurcation reflects similar geometric structure and (ii) that $\lambda_-^+ = 0$ coincides with the emergence of a pair of syntopic bumps with different widths when solving (9) simultaneously.

The eigenfunction $(\varphi(x), \psi(x))^{\mathrm{T}}$ associated with eigenvalue λ_-^+ has the following structure:

$$\begin{pmatrix} \varphi(x) \\ \psi(x) \end{pmatrix} = \begin{pmatrix} \Phi_-^+(x) \\ \Psi_-^+(x) \end{pmatrix} \equiv \frac{1}{(1 + \lambda_-^+)} \begin{pmatrix} \Omega_+^{loc}(x) - \Omega_+^{lay}(x) \\ -\Omega_+^{loc}(x) + \Omega_+^{lay}(x) \end{pmatrix}$$

and is illustrated in Figure 5 together with its effect as a perturbation of the syntopic bump. The function $\Omega_+^l(x)$ is even for $l \in \{loc, lay\}$ and is given in Appendix A. The functions $\Phi_-^+(x)$ and $\Psi_-^+(x)$ are even-symmetric and are equal but of opposite sign. Consequently, the eigenfunction produces a locally positive perturbation to the bump in one layer and a locally negative perturbation to the bump in the other layer, as shown in Figure 5. Hence, we expect a solution bifurcating from the syntopic bump with equal widths to reflect the spatial structure of the eigenfunction by exhibiting an *enhancement* of the bump in one layer and a *reduction* of the bump in the other layer, consistent with a *syntopic bump with different widths*.

To confirm the direct connection between the 0-eigenvalue ($\lambda_-^+ = 0$) and the emergence of the syntopic bumps with different widths, we numerically solved (9) in the vicinity of the bifurcation point to investigate the existence of syntopic bumps with different widths to see if they emerge/collide at the bifurcation point with the syntopic bump with equal widths. In all cases, a pair of syntopic bumps with different widths was found to emerge from the syntopic bump with equal widths precisely when $\lambda_-^+ = 0$ (and $\nu_-^+ = 0$ for the syntopic bumps with
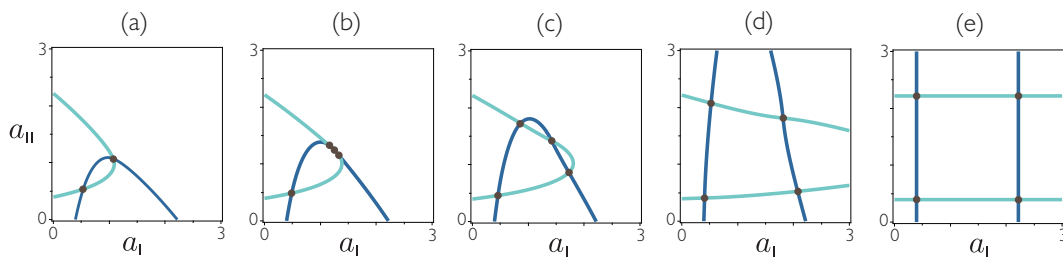
Figure 6. *A subcritical pitchfork bifurcation occurs when $\lambda_+^- = 0$ and gives rise to a pair of syntopic bumps with different widths ($a_I \neq a_{II}$) which are represented by off-diagonal points. Points along the diagonal represent syntopic bumps with equal widths ($a_I = a_{II}$). All figures show graphs of the zero sets for the two functions in (9) where points of intersection represent syntopic bumps. (a) $(A_{lay}^e, \sigma_{lay}^e) = (0.5, 1.4)$ and $\lambda_+^- \approx 0.072$, (b) $(A_{lay}^e, \sigma_{lay}^e) = (0.55, 1.5)$ and $\lambda_+^- \approx -0.013$, (c) $(A_{lay}^e, \sigma_{lay}^e) = (0.6, 1.6)$ and $\lambda_+^- \approx -0.069$, (d) $(A_{lay}^e, \sigma_{lay}^e) = (0.7, 1.75)$ and $\lambda_+^- \approx -0.158$, and (e) $(A_{lay}^e, \sigma_{lay}^e) = (0.8, 2.0)$ and $\lambda_+^- \approx -0.162$ in which case $w_{lay}(x) \equiv 0$. Fixed parameters are $A_{loc}^e = \sigma_{loc}^e = A_{loc}^i = 1, \sigma_{loc}^i = 5, A_{lay}^i = 0.8, \sigma_{lay}^i = 2, \theta = 0.2$.*

different widths in section 2.1.3). One example is shown in Figure 6 where the bifurcation point occurs between panel (a) and panel (b). The dark and light curves represent the solutions of each of the equations in (9), and intersection points (denoted by black dots) identify syntopic bumps. Syntopic bumps with equal widths lie on the diagonal where $a_I = a_{II}$. In Figure 6(a) both syntopic bumps with equal widths are unstable, with the larger syntopic bump having $\lambda_+^+ > 0$ as its only positive eigenvalue. In Figure 6, moving from (a) to (b) causes eigenvalue λ_-^+ to become negative, thereby stabilizing the large syntopic bump with equal widths in (b). Simultaneously, as the parameters increase through the bifurcation point, two syntopic bumps with different widths emerge in a (subcritical) pitchfork bifurcation from the syntopic bump with equal widths indicated by the two off-diagonal dots in Figure 6(b).

Parameters A_{lay}^e and σ_{lay}^e continue to increase so that as panel (e) is reached, the interlayer coupling is "turned off" ($w_{lay}(x) = 0$) due to the E and I components in (4) becoming equal ($A_{lay}^e = A_{lay}^i$ and $\sigma_{lay}^e = \sigma_{lay}^i$). Since the layers are decoupled, the solutions in the two layers are independent. For the parameters in Figure 6(e), the local connections w_{loc} in isolation support a pair of bumps, one smaller and unstable, and one larger and stable. Consequently, the four solutions in Figure 6(e) are the four permutations for constructing a syntopic bump in the pair of Amari layers from the two bumps that exist due only to the local connections within each Amari layer, and the sequence captures the transition from the bifurcation point to this uncoupled state. Interestingly, each syntopic bump with different widths here is formed by the small, unstable bump in one layer and the large, stable bump in the other layer.

It is also possible for a simultaneous pair of saddle-node bifurcations of syntopic bumps with different widths to occur, one pair appearing on either side of the syntopic bump with equal widths in the (a_I, a_{II})-plane. One such example occurs in the vicinity of the point $A_{loc}^e = \sigma_{loc}^e = A_{loc}^i = 1, \sigma_{loc}^i = 5, A_{lay}^e = 0.4, \sigma_{lay}^i = 2.21, A_{lay}^i = 0.5, \sigma_{lay}^i = 2$. There is a larger (stable) and a smaller (unstable) syntopic bump with equal widths and two pairs of syntopic bumps with different widths (all unstable due to various positive eigenvalues). Keeping other parameters fixed but setting $\sigma_{lay}^e = 2.15$ causes two of the syntopic bumps (one from each pair) to collide with the syntopic bump with equal widths in a pitchfork bifurcation.

Bifurcation to an allotopic bump ($\lambda_-^- = 0$). Destabilization of the syntopic bump
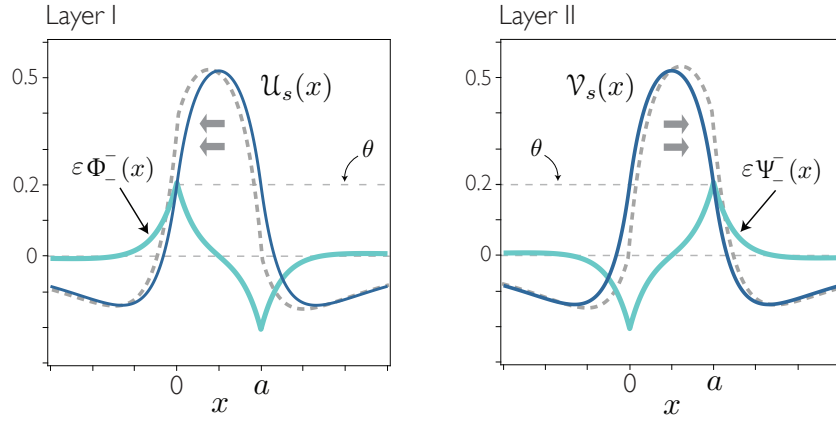
Figure 7. *At the pitchfork bifurcation point* $(\sigma_{lay}^e, a) \approx (1.844, 3.96)$, *the eigenfunction corresponding to* $\lambda_-(a) = 0$ *is represented by the light-colored solid curve in each layer, with component* $\Phi_-(x)$ *in Layer* I *and* $\Psi_-(x)$ *in Layer* II, *each scaled by* $\varepsilon = 0.2$. *The darker solid curves represent the stationary syntopic bump* $(\mathcal{U}_s(x)), \mathcal{V}_s(x))^{\mathrm{T}}$ *at the bifurcation point. The dashed gray curves in Layer* I *represent* $\mathcal{U}_s(x) + \varepsilon \Phi_-(x)$, *whereas the dashed gray curve in Layer* II *represents* $\mathcal{V}_s(x) + \varepsilon \Psi_-(x)$. *The gray curves illustrate that a small perturbation with respect to the eigenfunction* $(\Phi_-(x), \Psi_-(x))^{\mathrm{T}}$ *in* (16) *produces equal but opposite lateral shifts to the bump in each layer while simultaneously breaking the even symmetry of the syntopic bump. For this set of parameter values, the pitchfork bifurcation is subcritical, as indicated both by numerical simulations of the dynamical system* (3) *as well as by numerically solving the existence equations* (19) *for an allotopic bump. Fixed parameters are* $A_{loc}^e = \sigma_{loc}^e = A_{loc}^i = 1, \sigma_{loc}^i = 5, A_{lay}^e = 0.45, A_{lay}^i = 0.5, \sigma_{lay}^i = 2$.

through $\lambda_- = 0$ results in a pitchfork bifurcation that gives rise to a pair of *allotopic bumps*. The eigenvector associated with λ_- is illustrated in Figure 7 and can be expressed as

$$(16) \qquad \begin{pmatrix} \varphi(x) \\ \psi(x) \end{pmatrix} = \begin{pmatrix} \Phi_-(x) \\ \Psi_-(x) \end{pmatrix} = \frac{1}{(1 + \lambda_-)} \begin{pmatrix} \Omega_-^{loc}(x) - \Omega_-^{lay}(x) \\ -\Omega_-^{loc}(x) + \Omega_-^{lay}(x) \end{pmatrix},$$

where $\Omega_-^{loc}(x), \Omega_-^{lay}(x)$ are given in Appendix A. Indicated by the dashed curves in Figure 7, we illustrate the effect of perturbing the syntopic bump with respect to this eigenmode at the bifurcation point, which has the effect of displacing the bump in the two layers in opposite directions. Accordingly, this bifurcation gives rise to a new type of stationary bump that emerges from the syntopic bump and is composed of a stationary bump in each layer, each having width b and centers that are separated by a distance c. We refer to this solution as an allotopic bump because the centers of the stationary bump in the two layers are in different locations in space. At the bifurcation point, the distance between the bumps is $c = 0$, and the allotopic bump coincides with the syntopic bump with $(b, c) = (a, 0)$. As the bifurcation parameter is increased from the bifurcation point, the distance c between the bumps increases.

In Figures 9 and 10 we describe a supercritical and a subcritical pitchfork bifurcation, respectively, with respect to the λ_- eigenmode. The bifurcation parameter is the space constant σ_{lay}^e of the excitatory interlayer connections, and the effect of its variation on the interlayer weight function is shown in Figure 8 for the two cases. To determine whether the bifurcation was super- or subcritical, (i) we studied numerical simulations of (3) in a vicinity of the bifurcation point, and (ii) we analyzed the existence and linear stability of both the syntopic and
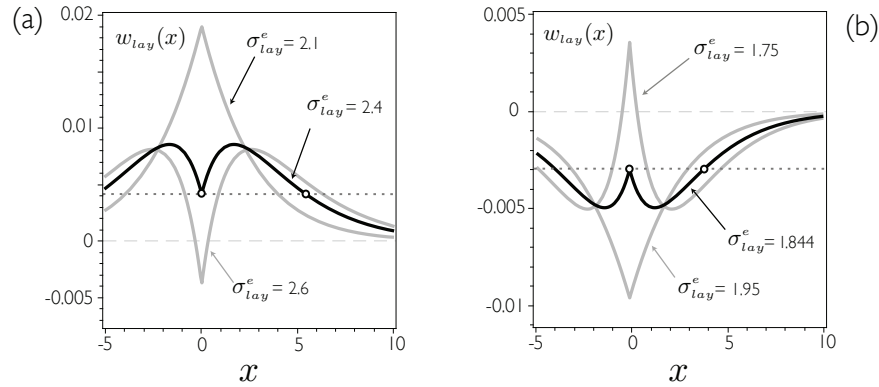
Figure 8. *Structure of the interlayer synaptic weight functions near the pitchfork bifurcation point with* (a) *and* (b) *corresponding to the two different cases shown in Figures* 9 *and* 10, *respectively. The solid black curve indicates the interlayer weight function at the bifurcation point, and the condition for a pitchfork bifurcation with respect to eigenvalue* $\lambda_-(a)$ *is given by* $w_{lay}(a) = w_{lay}(0)$, *which is satisfied at the circles that lie along the horizontal dotted line and denote the points* $(0, w_{lay}(0))$ *and* $(a, w_{lay}(a))$. *Figure* (a) *corresponds to a supercritical bifurcation with fixed parameters:* $A_{loc}^e = \sigma_{loc}^e = A_{loc}^i = 1, \sigma_{loc}^i = 5, A_{lay}^e = 0.5, A_{lay}^i = 0.4, \sigma_{lay}^i = 2$. *Figure* (b) *corresponds to a subcritical pitchfork bifurcation with fixed parameters:* $A_{loc}^e = \sigma_{loc}^e = A_{loc}^i = 1, \sigma_{loc}^i = 5, A_{lay}^e = 0.45, A_{lay}^i = 0.5, \sigma_{lay}^i = 2$.

allotopic bumps (see sections 2.1.1 and 2.1.2), numerically solved (8) and (19) in a vicinity of the bifurcation point, and calculated the eigenvalues of the syntopic and allotopic bumps. As a result, we found the expected agreement between the signs of the eigenvalues and the side of the bifurcation point where the allotopic bump appears. In the *supercritical* case in Figure 9, we calculate the ω-limit set in numerical simulations from an initial condition composed of Gaussian bumps in each layer with a small spatial offset to illustrate the emergence of the stable allotopic bump from the stable syntopic bump at the bifurcation point. In the *subcritical* case in Figure 10, the unstable allotopic bump can be detected in simulations of (3). As the bifurcation is subcritical, the parameter σ_{lay}^e was set so that there is a stable syntopic bump and a coexistent unstable allotopic bump. Starting from initial conditions formed from a small Gaussian bump in each layer with incrementally larger spatial offsets on each subsequent simulation, a critical spatial offset was reached, below which initial conditions approach the stable syntopic bump (left panel) and above which the two activity bumps in the initial condition propagate outward (right panel), continually slowing down as the interaction between the bumps decays with the growing distance. This dichotomy of behavior is due to the unstable allotopic bump acting as a separatrix that selectively diverts solutions to the syntopic bump if the initial activity bumps are sufficiently close and drives activity bumps apart if the distance between them is sufficiently large.

2.1.2. Existence and linear stability of allotopic bumps. The offset or allotopic bump (*allo* and *topic* meaning *other* and *place*) is composed of stationary bumps $\mathcal{U}_o(x)$ in Layer I and $\mathcal{V}_o(x)$ in Layer II, where the bumps have width b and are separated by a distance c. In this section, we analyze the existence and linear stability of the allotopic bump $(\mathcal{U}_o(x), \mathcal{V}_o(x))^{\mathrm{T}}$ and construct a bifurcation diagram demonstrating how a pair of allotopic bumps bifurcates from the stable-unstable pair of syntopic bumps. (Note that the subscript o denotes *offset*
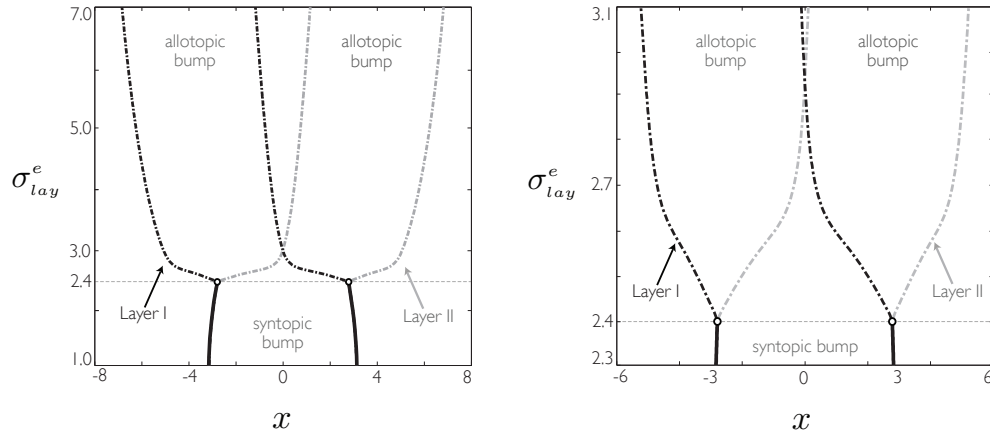
Figure 9. *Supercritical pitchfork bifurcation of a syntopic bump giving rise to a stable allotopic bump in the pair of interacting Amari neural field layers. The curves represent the threshold points of the activity bump in each layer at different values of the bifurcation parameter, and the regions between pairs of curves with similar line style represent the superthreshold regions for the activity bump in each layer. Left: The curves show the stable long-term behavior (ω-limit set) in numerical simulations where the bifurcation parameter σ_{lay}^e is varied from 1.0 to 7.0. The pitchfork bifurcation point occurs at $\sigma_{lay}^e \approx 2.4$ indicated by the dotted horizontal line where the syntopic bump destabilizes into a stable allotopic bump with the spatial offset between the bumps in each layer increasing with the bifurcation parameter. Right: Close-up of the left figure restricted to $\sigma_{lay}^e \in [2.3, 3.1]$. The bifurcation diagram for this case is shown in Figure 11. Fixed parameter: $\theta = 0.2$, $A_{loc}^e = \sigma_{loc}^e = A_{loc}^i = 1$, $\sigma_{loc}^i = 5$, $A_{lay}^e = 0.5$, $A_{lay}^i = 0.4$, $\sigma_{lay}^i = 2$.*

while we use the subscript a to denote *antisyntopic*, which occurs only in the periodic case.)

Existence of an allotopic bump. Translation invariance of the stationary allotopic bump allows for two natural coordinate systems in which to consider the spatial dependence of the allotopic bump. Although the pitchfork structure is perhaps best visualized in a spatial coordinate system wherein the origin is taken to be the center point between the two offset bumps, it is more convenient to work in a coordinate system in which the origin coincides with the threshold boundary of one of the bumps, as illustrated in Figure 2. In particular, we align the left boundary of the bump $\mathcal{U}_o(x)$ in Layer I to be the origin. The pitchfork arises from connection symmetries whereby switching the solution in each layer also forms a solution. From symmetries in the dual layer Amari network, the stationary bump $\mathcal{V}_o(x)$ in Layer II is a reflection and a spatial translation of the stationary bump $\mathcal{U}_o(x)$ in Layer I satisfying

$$(17) \qquad\qquad \mathcal{V}_o(x) = \mathcal{U}_o\big(-(x - c - b)\big).$$

Accordingly, the threshold conditions for the allotopic bump are expressed in terms of the stationary bump $\mathcal{U}_o(x)$ in Layer I and $\mathcal{V}_o(x)$ in Layer II, which satisfy

$$\mathcal{U}_o(0) = \mathcal{U}_o(b) = \theta, \qquad\qquad \mathcal{V}_o(c) = \mathcal{V}_o(c + b) = \theta,$$

and we require that $\mathcal{U}_o, \mathcal{V}_o$ are superthreshold over the following regions only,

$$\mathcal{U}_o(x) > \theta, \quad x \in (0, b), \qquad \mathcal{V}_o(x) > \theta, \quad x \in (c, c + b),$$
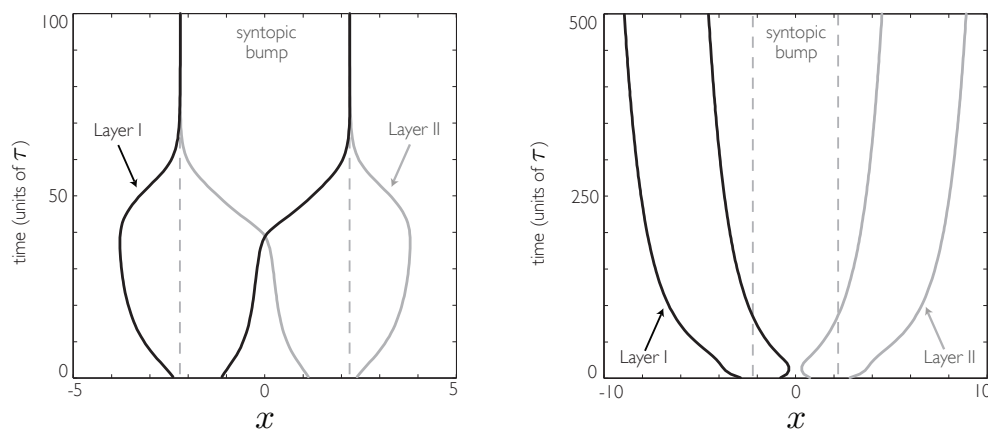
Figure 10. *Subcritical pitchfork bifurcation of a syntopic bump giving rise to an unstable allotopic bump. The bifurcation parameter $\sigma_{lay}^e = 1.0$, which is below the pitchfork bifurcation point that occurs at $\sigma_{lay}^e \approx 1.844$; the syntopic bump is linearly stable and is surrounded by an unstable allotopic bump, reflecting a subcritical bifurcation. Both panels illustrate the time evolution of the threshold points of the activity bump in each layer, starting from an initial condition composed of a Gaussian bump in each layer with a spatial offset near that of the unstable allotopic bump. Left: The spatial offset in the Gaussian initial conditions is slightly less than that of the unstable allotopic bump, and the activity bumps in each layer approach the syntopic bump after a short transient. Right: The spatial offset in the Gaussian initial conditions is slightly greater than that of the unstable allotopic bump; the activity bumps in each layer are repelled outward but continually slow down since the strength of the interlayer connections decreases as the distance between bumps increases. Note that each layer here supports a stationary bump in the absence of interlayer connections. Fixed parameters are $A_{loc}^e = 1, \sigma_{loc}^e = 1, A_{loc}^i = 1, \sigma_{loc}^i = 5, A_{lay}^e = 0.45, A_{lay}^i = 0.5, \sigma_{lay}^i = 2, \theta = 0.2$.*

and subthreshold otherwise with $\mathcal{U}_o(x), \mathcal{V}_o(x) \longrightarrow 0$ as $x \to \pm\infty$. Under the above conditions the allotopic bump can be expressed as

$$(18) \quad \begin{aligned} \mathcal{U}_o(x) &= \big[W_{loc}(x) - W_{loc}(x-b)\big] + \big[W_{lay}(x-c) - W_{lay}(x-b-c)\big], \\ \mathcal{V}_o(x) &= \big[W_{loc}(x-c) - W_{loc}(x-b-c)\big] + \big[W_{lay}(x) - W_{lay}(x-b)\big]. \end{aligned}$$

Finally, the conditions for the existence of an allotopic bump can be expressed as

$$(19) \quad \begin{aligned} \theta &= W_{loc}(b) - W_{lay}(c) + W_{lay}(c+b), \\ \theta &= W_{loc}(b) + W_{lay}(c) - W_{lay}(c-b), \end{aligned}$$

which determine the symmetric bump width b and spatial offset c, i.e., the distance between the bumps in each layer (see Figure 2(b)). Note that the odd-symmetry of $W_{loc,lay}$ was used. Equations (19) can alternatively be expressed as

$$(20) \quad \begin{aligned} 0 &= F_1(\sigma, b, c) \equiv 2W_{loc}(b) + W_{lay}(c+b) - W_{lay}(c-b) - 2\theta, \\ 0 &= F_2(\sigma, b, c) \equiv 2W_{lay}(c) - W_{lay}(c+b) - W_{lay}(c-b). \end{aligned}$$

Bifurcation curves for the syntopic and allotopic bumps. We solved the existence conditions (8) and (19) for syntopic and allotopic bumps, respectively, to generate a bifurcation diagram in the vicinity of a pair of pitchfork bifurcations with respect to the λ_-^- eigenmode
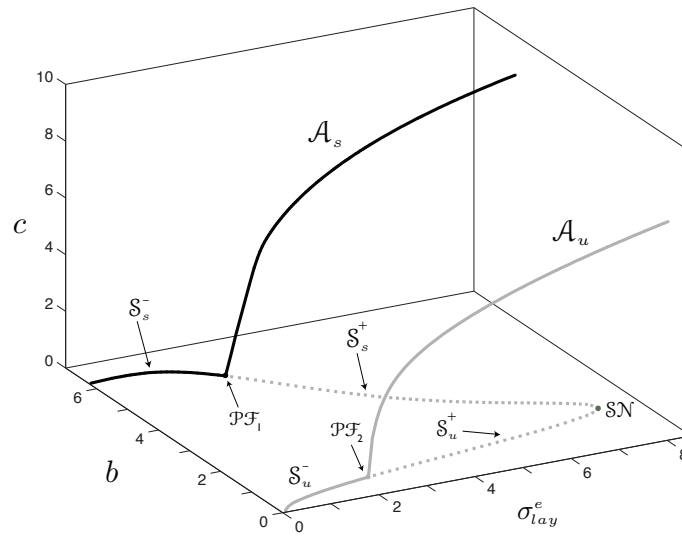
Figure 11. *Bifurcation diagram of syntopic and allotopic bumps in the dual Amari neural field (3) corresponding to parameters used in Figure 9. Syntopic bumps are represented as having width $b = a$ with spatial offset $c = 0$. As σ_{lay}^e decreases, both the stable branch $\mathcal{S}_s^-$ and unstable branch $\mathcal{S}_u^-$ of syntopic bumps undergo pitchfork bifurcations with respect to the λ_-^- eigenvalue in their linearizations (the unstable syntopic branch of bumps $\mathcal{S}_u^-$ has $\mathrm{sgn}(\lambda_+^{\pm}) = \pm1$). The bifurcation point $\mathcal{PF}_1$ for the stable syntopic bump $(\mathcal{U}_s, \mathcal{V}_s)^{\mathrm{T}}$ occurs at $(\sigma_{lay}^e, b, c) \approx (2.4, 5.57, 0)$, and the bifurcation point $\mathcal{PF}_2$ for the unstable syntopic bump occurs at $(\sigma_{lay}^e, b, c) \approx (2.26, 0.74, 0)$. A curve $\mathcal{A}_s$ of stable allotopic bumps $(\mathcal{U}_o, \mathcal{V}_o)^{\mathrm{T}}$ with bump width b bifurcates, and the distance c between the offset bumps increases monotonically with σ_{lay}^e. After the pitchfork bifurcation, the two unstable syntopic bumps collide in a saddle-node bifurcation, denoted by $\mathcal{SN}$, at $\sigma_{lay}^e \approx 7.64$ $(b = 1.76, c = 0)$. The eigenvalue structure along the branches of stationary bumps plotted in the figure is given as follows according to the ordering $(\lambda_+^+, \lambda_-^+, \lambda_+^-, \lambda_-^-)$. The curves and their eigenvalue structure are given as $\mathcal{S}_s^- : (-, -, 0, -)$, $\mathcal{S}_s^+ : (-, \pm, 0, +)$, $\mathcal{S}_u^- : (+, \pm, 0, -)$, $\mathcal{S}_u^+ : (+, +, 0, +)$, $\mathcal{A}_s : (-, -, 0, -)$, $\mathcal{A}_u : (+, -, 0, +)$. Other parameters: $A_{loc}^e = \sigma_{loc}^e = A_{loc}^i = 1, \sigma_{loc}^i = 5, A_{lay}^e = 0.5, A_{lay}^i = 0.4, \sigma_{lay}^i = 2, \theta = 0.2$. Appeared previously in Folias & Ermentrout, Phys. Rev. Lett., 107 (2011), 228103. © 2011 by the American Physical Society.*

of the linearization around each syntopic bump. The bifurcation parameter is σ_{lay}^e, and, since the excitatory and inhibitory components of the weight function are normalized, the effect of increasing σ_{lay}^e is to spread out the same amount of excitatory synaptic input over a larger region. The diagram in Figure 11 shows that for narrow and strong interlayer excitatory synaptic input ($\sigma_{lay}^e < 2$), there is a stable-unstable pair of syntopic bumps (which are given by $(b, c) = (a, 0)$ since c represents the spatial offset). As σ_{lay}^e increases, a pitchfork bifurcation occurs on each branch of syntopic bumps (at points $\mathcal{PF}_1$ and $\mathcal{PF}_2$) when $\lambda_-^- = 0$, and each gives rise to a branch of allotopic bumps (each branch represents two solutions where the solution in each layer can be switched). Linear stability analysis of the allotopic bump (below) indicates the bifurcations are supercritical in agreement with the geometry of the direction of bifurcation in Figure 11. Finally, the two syntopic bumps annihilate in a saddle-node bifurcation at $\mathcal{SN}$, while the allotopic bumps persist for larger values of σ_{lay}^e.

Failure of the implicit function theorem and eigenvalue λ_-^-. Along a curve of allotopic bumps, e.g., curve $\mathcal{A}_s$ in Figure 11, failure of the implicit function theorem reveals the related condition for a 0-eigenvalue λ_-^- at the bifurcation point. Assume the eigenvalues for the

syntopic bump at the bifurcation point $(\sigma, b, c) = (\sigma^*, b^*, 0)$ satisfy $\lambda^+_\pm < 0, \lambda^-_+ = 0$. We redefine $\sigma = \sigma^e_{lay}$ and consider the Jacobian of the function (F_1, F_2) in (20):

$$\frac{\partial(F_1, F_2)}{\partial(\sigma, b, c)} = \begin{bmatrix} \frac{\partial F_1}{\partial \sigma} & \frac{\partial F_1}{\partial b} & \frac{\partial F_1}{\partial c} \\ \frac{\partial F_2}{\partial \sigma} & \frac{\partial F_2}{\partial b} & \frac{\partial F_2}{\partial c} \end{bmatrix}.$$

For (σ, b, c) along curve $\mathcal{A}_s$ but not at a bifurcation point, $\det \mathrm{J}(\sigma, b, c) \neq 0$, where

$$\mathrm{J}(\sigma, b, c) = \begin{bmatrix} \frac{\partial F_1}{\partial b} & \frac{\partial F_1}{\partial c} \\ \frac{\partial F_2}{\partial b} & \frac{\partial F_2}{\partial c} \end{bmatrix}.$$

Failure of the implicit function theorem means $\det \mathrm{J}(\sigma, b, c) = 0$ at the bifurcation point $(\sigma, b, c) = (\sigma^*, b^*, 0)$, where

$$\det \mathrm{J}(\sigma^*, b^*, 0) = 4\Big(w_{loc}(b^*) + w_{lay}(b^*)\Big)\Big(w_{lay}(0) - w_{lay}(b^*)\Big).$$

Note that $w_{loc}(b^*) + w_{lay}(b^*) < 0$ since we are concerned with the regime where $\lambda^+_+ < 0$ in the vicinity of the bifurcation. Therefore, $\det \mathrm{J}(\sigma^*, b^*, 0) = 0$ precisely when $w_{lay}(0) - w_{lay}(b^*) = 0$, which is identical to the condition for $\lambda^- = 0$. When the pitchfork bifurcation coincides with the saddle-node bifurcation of syntopic bumps, we also have $w_{loc}(b^*) + w_{lay}(b^*) = 0$.

Linear stability of an allotopic bump. We briefly consider the linear stability of the allotopic bump $(\mathcal{U}_o, \mathcal{V}_o)^\mathrm{T}$ by setting $u(x, t) = \mathcal{U}_o(x) + \varphi(x)e^{\mu t}$ and $v(x, t) = \mathcal{V}_o(x) + \psi(x)e^{\mu t}$ in the linearization about the allotopic bump along the lines of section 2.1.1 for the syntopic bump. This leads to the spectral problem for μ and $(\varphi(x), \psi(x))^\mathrm{T}$,

$$(21) \qquad \begin{aligned} \mu\,\varphi &= -\varphi + \mathcal{N}_{loc}[\mathcal{U}_o]\,\varphi + \mathcal{N}_{lay}[\mathcal{V}_o]\,\psi, \\ \mu\,\psi &= -\psi + \mathcal{N}_{loc}[\mathcal{V}_o]\,\psi + \mathcal{N}_{lay}[\mathcal{U}_o]\,\varphi, \end{aligned}$$

and the operators for $l \in \{loc, lay\}$ and $\mathcal{U} \in \{\mathcal{U}_o, \mathcal{V}_o\}$ are given in (12).

Setting $x = 0$ and $x = b$ in the first equation and $x = c$ and $x = b + c$ in the second yields compatibility conditions for the values of $\varphi(0), \varphi(b), \psi(c), \psi(c + b)$ resulting in the equation

$$\big(\mathrm{M}_o - \mathrm{I}_4\big)\boldsymbol{v} = \mu\boldsymbol{v},$$

$$\mathrm{M}_o(b, c) = \begin{bmatrix} \mathring{w}_{loc}(0) & \overset{\times}{w}_{loc}(b) & \overset{\times}{w}_{lay}(c) & \mathring{w}_{lay}(b+c) \\ \mathring{w}_{loc}(b) & \overset{\times}{w}_{loc}(0) & \overset{\times}{w}_{lay}(b-c) & \mathring{w}_{lay}(c) \\ \mathring{w}_{lay}(c) & \overset{\times}{w}_{lay}(b-c) & \overset{\times}{w}_{loc}(0) & \mathring{w}_{loc}(b) \\ \mathring{w}_{lay}(b+c) & \overset{\times}{w}_{lay}(c) & \overset{\times}{w}_{loc}(b) & \mathring{w}_{loc}(0) \end{bmatrix}, \quad \boldsymbol{v} = \begin{pmatrix} \varphi(0) \\ \varphi(b) \\ \psi(c) \\ \psi(b+c) \end{pmatrix},$$

where we have defined $\mathring{w}_l(x) = w_l(x)/|\mathcal{U}'_o(0)|$ and $\overset{\times}{w}_l(x) = w_l(x)/|\mathcal{U}'_o(b)|$ for $l \in \{loc, lay\}$ and from symmetry conditions $|\mathcal{U}'_o(0)| = |\mathcal{V}'_o(c + b)|$ and $|\mathcal{U}'_o(b)| = |\mathcal{V}'_o(c)|$.

Using a similarity transformation, we express $Q_o^{-1}(M_o - I_4)Q_o = \Lambda_o$, where Λ_o is the block diagonal matrix shown below, the details of which are collected in Appendix B:

$$\Lambda_o = \begin{bmatrix} \Lambda_+ & 0 \\ 0 & \Lambda_- \end{bmatrix}, \qquad \Lambda_\pm = \begin{bmatrix} -1 + \mathring{w}_{loc}(0) \pm \mathring{w}_{lay}(b+c) & \overset{\times}{w}_{loc}(b) \pm \overset{\times}{w}_{lay}(c) \\ \mathring{w}_{loc}(b) \pm \mathring{w}_{lay}(c) & -1 + \overset{\times}{w}_{loc}(0) \pm \overset{\times}{w}_{lay}(b-c) \end{bmatrix}.$$

M_o and Λ_o share the same eigenvalues $\mu_\pm^+(b,c)$ and $\mu_\pm^-(b,c)$ from Λ_+ and Λ_-, respectively,

$$\mu_\pm^+(b,c) = +\tfrac{1}{2}\Big[\tfrac{1}{\gamma_\circ}\big(w_{loc}(0) + w_{lay}(b+c)\big) + \tfrac{1}{\gamma_\times}\big(w_{loc}(0) + w_{lay}(b-c)\big) - 2 \Big]$$
$$\pm \tfrac{1}{2}\sqrt{\Big[\frac{w_{loc}(0) + w_{lay}(b+c)}{\gamma_\circ} - \frac{w_{loc}(0) + w_{lay}(b-c)}{\gamma_\times} \Big]^2 + \frac{4\big[w_{loc}(b) + w_{lay}(c)\big]^2}{\gamma_\circ \gamma_\times}},$$

where $\gamma_\circ = |\mathcal{U}_o'(0)|$ and $\gamma_\times = |\mathcal{U}_o'(b)|$, and, since $\det \Lambda_- = 0$, we can reduce $\mu_\pm^-(b,c)$ further to

$$\mu_+^-(b,c) \equiv 0, \qquad \mu_-^-(b,c) = \operatorname{tr}\Lambda_- = \tfrac{1}{\gamma_\circ}\big[w_{loc}(0) - w_{lay}(b+c)\big] + \tfrac{1}{\gamma_\times}\big[w_{loc}(0) - w_{lay}(b-c)\big] - 2,$$

where $\mu_+^- \equiv 0$ reflects the translation invariance of the allotopic bump. The eigenfunctions can be calculated along the lines developed in Appendix A. The eigenvalues were evaluated numerically to determine the stability along the curves of allotopic bumps in Figure 11. When the pitchfork bifurcation occurs on the larger (stable) syntopic bump, the bifurcation is supercritical and gives rise to a stable allotopic bump; the bifurcation is also supercritical on the smaller (unstable) syntopic bump, but in this case the bifurcating allotopic bump is unstable due to other eigenvalues. Conversely, in the parameter region for Figure 10, the allotopic bump bifurcating from the stable syntopic bump is unstable, as the pitchfork bifurcation in this case is subcritical.

2.1.3. Bifurcation of syntopic bumps for reciprocally asymmetric interlayer coupling. We briefly consider the extension to an interacting pair of Amari neural fields with identical local synaptic coupling and *reciprocally asymmetric* interlayer synaptic coupling $(w_{lay}^{\mathsf{I}} \neq w_{lay}^{\mathsf{II}})$

$$(22) \qquad \begin{aligned} \tau\, \partial_t u &= -u + w_{loc} * H(u - \theta) + w_{lay}^{\mathsf{I}} * H(v - \theta), \\ \tau\, \partial_t v &= -v + w_{loc} * H(v - \theta) + w_{lay}^{\mathsf{II}} * H(u - \theta). \end{aligned}$$

Existence of a syntopic bump for asymmetric interlayer coupling. A syntopic bump in (22) is composed of an even-symmetric, stationary bump in each layer with the same *centers* $(x = 0)$ in the universal coordinate system; however, generically, the bumps in each layer have *different widths* due to the asymmetry in the interlayer coupling. Thus, we set $(u(x,t), v(x,t))^{\mathrm{T}} = (\mathcal{U}_{\mathsf{I}}(x), \mathcal{V}_{\mathsf{II}}(x))^{\mathrm{T}}$ and let a_{I} and a_{II} denote the *stationary bump halfwidths* in Layer I and Layer II, respectively. The existence conditions for a_{I} and a_{II} then satisfy

$$(23) \qquad \mathcal{U}_{\mathsf{I}}(-a_{\mathsf{I}}) = \mathcal{U}_{\mathsf{I}}(a_{\mathsf{I}}) = \theta, \qquad \mathcal{V}_{\mathsf{II}}(-a_{\mathsf{II}}) = \mathcal{V}_{\mathsf{II}}(a_{\mathsf{II}}) = \theta,$$

$$\mathcal{U}_{\mathsf{I}}(x) > \theta, \quad x \in (-a_{\mathsf{I}}, a_{\mathsf{I}}), \qquad \mathcal{V}_{\mathsf{II}}(x) > \theta, \quad x \in (-a_{\mathsf{II}}, a_{\mathsf{II}}),$$

with $\mathcal{U}_{\mathsf{I}}$ and $\mathcal{V}_{\mathsf{II}}$ subthreshold otherwise and $\mathcal{U}_{\mathsf{I}}(x), \mathcal{V}_{\mathsf{II}}(x) \longrightarrow 0$ as $x \to \pm\infty$.

Provided the thresholding conditions are satisfied, the stationary syntopic bump $(\mathcal{U}_\mathsf{I}, \mathcal{V}_\mathsf{II})$ in the case of asymmetric interlayer coupling can be expressed as

$$(24) \qquad \mathcal{U}_\mathsf{I}(x) = \big[W_{loc}(x + a_\mathsf{I}) - W_{loc}(x - a_\mathsf{I})\big] + \big[W_{lay}^\mathsf{I}(x + a_\mathsf{II}) - W_{lay}^\mathsf{I}(x - a_\mathsf{II})\big],$$

$$(25) \qquad \mathcal{V}_\mathsf{II}(x) = \big[W_{loc}(x + a_\mathsf{II}) - W_{loc}(x - a_\mathsf{II})\big] + \big[W_{lay}^\mathsf{II}(x + a_\mathsf{I}) - W_{lay}^\mathsf{II}(x - a_\mathsf{I})\big],$$

where $W_l^u(x) \equiv \int_0^x w_l^u(y)\, dy$ for $u \in \{\mathsf{I},\mathsf{II}\}$ and $l \in \{loc, lay\}$. Setting $x = a_\mathsf{I}$ in (24) and $x = a_\mathsf{II}$ in (25), the threshold conditions result in the following compatibility condition for a_I and a_II for the existence of a *syntopic bump with different widths*:

$$(26) \qquad \begin{aligned} \theta &= W_{loc}(2a_\mathsf{I}) + W_{lay}^\mathsf{I}(a_\mathsf{I} + a_\mathsf{II}) - W_{lay}^\mathsf{I}(a_\mathsf{I} - a_\mathsf{II}), \\ \theta &= W_{loc}(2a_\mathsf{II}) + W_{lay}^\mathsf{II}(a_\mathsf{I} + a_\mathsf{II}) + W_{lay}^\mathsf{II}(a_\mathsf{I} - a_\mathsf{II}). \end{aligned}$$

This is provided $\mathcal{U}_\mathsf{I}$ and $\mathcal{V}_\mathsf{II}$ cross threshold only at the points $\pm a_\mathsf{I}$ and $\pm a_\mathsf{II}$, respectively.

Special case ($w_{lay}^\mathsf{I} \equiv w_{lay}^\mathsf{II} \equiv w_{lay}$) for syntopic bump with different widths. Existence of syntopic bumps with *different widths* in the case of *reciprocally symmetric* interlayer coupling ($w_{lay}^\mathsf{I} \equiv w_{lay}^\mathsf{II} \equiv w_{lay}$) can be treated as a special case of (26) for the existence of syntopic bumps with different widths in the case of *reciprocally asymmetric* interlayer coupling by setting $W_{lay}^\mathsf{I} \equiv W_{lay}^\mathsf{II} \equiv W_{lay}$ in (26) but allowing $a_\mathsf{I} \neq a_\mathsf{II}$. This results in (9). Furthermore, by making the substitutions described above, the linear stability analysis that is developed below reduces analogously as a special case for syntopic bumps with different widths in (3) which has reciprocally symmetric interlayer coupling.

Linear stability of a syntopic bump for asymmetric interlayer coupling. Without loss of generality, we set $\tau = 1$ and consider the linear stability of a syntopic bump with different widths $(\mathcal{U}_\mathsf{I}, \mathcal{V}_\mathsf{II})^\mathrm{T}$ by setting $u(x,t) = \mathcal{U}_\mathsf{I}(x) + \varphi(x)e^{\nu t}$ and $v(x,t) = \mathcal{V}_\mathsf{II}(x) + \psi(x)e^{\nu t}$ in the linearization about the syntopic bump, leading to the spectral problem for ν and $(\varphi(x), \psi(x))^\mathrm{T}$

$$(27) \qquad \begin{aligned} \nu\varphi &= -\varphi + \mathcal{N}_{loc}[\mathcal{U}_\mathsf{I}]\varphi + \mathcal{N}_{lay}[\mathcal{V}_\mathsf{II}]\psi, \\ \nu\psi &= -\psi + \mathcal{N}_{loc}[\mathcal{V}_\mathsf{II}]\psi + \mathcal{N}_{lay}[\mathcal{U}_\mathsf{I}]\varphi, \end{aligned}$$

with $\mathcal{N}_l[\mathcal{U}]$ defined in (12). Setting $x = \pm a_\mathsf{I}$ in the first equation and $x = \pm a_\mathsf{II}$ in the second yields the following compatibility matrix equation for the values of $\varphi(-a_\mathsf{I}), \varphi(a_\mathsf{I}), \psi(-a_\mathsf{II}), \psi(a_\mathsf{II})$:

$$\big(\mathrm{M}_{\mathrm{asym}} - \mathrm{I}_4\big)\boldsymbol{v} = \nu\,\boldsymbol{v},$$

$$\mathrm{M}_{\mathrm{asym}}(a_\mathsf{I}, a_\mathsf{II}) = \begin{bmatrix} \tilde{w}_{loc}(0) & \tilde{w}_{loc}(2a_\mathsf{I}) & \breve{w}_{lay}^\mathsf{I}(a_\mathsf{I} - a_\mathsf{II}) & \breve{w}_{lay}^\mathsf{I}(a_\mathsf{I} + a_\mathsf{II}) \\ \tilde{w}_{loc}(2a_\mathsf{I}) & \tilde{w}_{loc}(0) & \breve{w}_{lay}^\mathsf{I}(a_\mathsf{I} + a_\mathsf{II}) & \breve{w}_{lay}^\mathsf{I}(a_\mathsf{I} - a_\mathsf{II}) \\ \tilde{w}_{lay}^\mathsf{II}(a_\mathsf{I} - a_\mathsf{II}) & \tilde{w}_{lay}^\mathsf{II}(a_\mathsf{I} + a_\mathsf{II}) & \breve{w}_{loc}(0) & \breve{w}_{loc}(2a_\mathsf{II}) \\ \tilde{w}_{lay}^\mathsf{II}(a_\mathsf{I} + a_\mathsf{II}) & \tilde{w}_{lay}^\mathsf{II}(a_\mathsf{I} - a_\mathsf{II}) & \breve{w}_{loc}(2a_\mathsf{II}) & \breve{w}_{loc}(0) \end{bmatrix}, \quad \boldsymbol{v} = \begin{pmatrix} \varphi(-a_\mathsf{I}) \\ \varphi(a_\mathsf{I}) \\ \psi(-a_\mathsf{II}) \\ \psi(a_\mathsf{II}) \end{pmatrix},$$

where $|\mathcal{U}_\mathsf{I}'(-a_\mathsf{I})| = |\mathcal{U}_\mathsf{I}'(a_\mathsf{I})|$ and $|\mathcal{V}_\mathsf{II}'(-a_\mathsf{II})| = |\mathcal{V}_\mathsf{II}'(a_\mathsf{II})|$ by even symmetry and we have defined

$$\tilde{w}_{loc}(x) = \frac{w_{loc}(x)}{|\mathcal{U}_\mathsf{I}'(a_\mathsf{I})|}, \qquad \breve{w}_{loc}(x) = \frac{w_{loc}(x)}{|\mathcal{V}_\mathsf{II}'(a_\mathsf{II})|}, \qquad \tilde{w}_{lay}^\mathsf{I}(x) = \frac{w_{lay}^\mathsf{I}(x)}{|\mathcal{U}_\mathsf{I}'(a_\mathsf{I})|}, \qquad \breve{w}_{lay}^\mathsf{II}(x) = \frac{w_{lay}^\mathsf{II}(x)}{|\mathcal{V}_\mathsf{II}'(a_\mathsf{II})|}.$$

Using a similarity transformation, we express $Q^{-1}(M_{asym} - I_4)Q = \Lambda_{asym}$, where Λ_{asym} is the block diagonal matrix shown below, the details of which are collected in Appendix C:

$$\Lambda_{asym} = \begin{bmatrix} \Lambda_+ & 0 \\ 0 & \Lambda_- \end{bmatrix}, \qquad \Lambda_{\pm} = \begin{bmatrix} -1 + \tilde{w}_{loc}(0) \pm \tilde{w}_{loc}(2a_{\mathsf{I}}) & \breve{w}^{\mathsf{I}}_{lay}(a_{\mathsf{I}} - a_{\mathsf{II}}) \pm \breve{w}^{\mathsf{I}}_{lay}(a_{\mathsf{I}} + a_{\mathsf{II}}) \\ \tilde{w}^{\mathsf{II}}_{lay}(a_{\mathsf{I}} - a_{\mathsf{II}}) \pm \tilde{w}^{\mathsf{II}}_{lay}(a_{\mathsf{I}} + a_{\mathsf{II}}) & -1 + \breve{w}_{loc}(0) \pm \breve{w}_{loc}(2a_{\mathsf{II}}) \end{bmatrix}.$$

M_{asym} and Λ_{asym} have the same eigenvalues $\nu_{\pm}^+$ and $\nu_{\pm}^-$ (from Λ_+ and Λ_-, respectively),

$$\begin{aligned}
\nu_{\pm}^+(a_{\mathsf{I}}, a_{\mathsf{II}}) = & +\tfrac{1}{2}\Big[\, \tfrac{1}{\gamma_{\mathsf{I}}}\big(w_{loc}(0) + w_{loc}(2a_{\mathsf{I}})\big) + \tfrac{1}{\gamma_{\mathsf{II}}}\big(w_{loc}(0) + w_{loc}(2a_{\mathsf{II}})\big) - 2 \,\Big] \\
& \pm \tfrac{1}{2}\Big\{ \big[\tfrac{1}{\gamma_{\mathsf{I}}}\big(w_{loc}(0) + w_{loc}(2a_{\mathsf{I}})\big) - \tfrac{1}{\gamma_{\mathsf{II}}}\big(w_{loc}(0) + w_{loc}(2a_{\mathsf{II}})\big)\big]^2 \\
& \quad + \tfrac{4}{\gamma_{\mathsf{I}}\gamma_{\mathsf{II}}}\big[w^{\mathsf{I}}_{lay}(a_{\mathsf{I}} - a_{\mathsf{II}}) + w^{\mathsf{I}}_{lay}(a_{\mathsf{I}} + a_{\mathsf{II}})\big]\big[w^{\mathsf{II}}_{lay}(a_{\mathsf{I}} - a_{\mathsf{II}}) + w^{\mathsf{II}}_{lay}(a_{\mathsf{I}} + a_{\mathsf{II}})\big] \Big\}^{1/2},
\end{aligned}$$

where $\gamma_{\mathsf{I}} = |\mathcal{U}'_{\mathsf{I}}(a_{\mathsf{I}})| = |\mathcal{U}'_{\mathsf{I}}(-a_{\mathsf{I}})|$ and $\gamma_{\mathsf{II}} = |\mathcal{V}'_{\mathsf{II}}(a_{\mathsf{II}})| = |\mathcal{V}'_{\mathsf{II}}(-a_{\mathsf{II}})|$, and, since $\det \Lambda_- = 0$,

$$\nu_+^-(b, c) \equiv 0, \qquad \nu_-^-(b, c) = \mathsf{tr}\, \Lambda_- = \tfrac{1}{\gamma_{\mathsf{I}}}\big[w_{loc}(0) - w_{loc}(2a_{\mathsf{I}})\big] + \tfrac{1}{\gamma_{\mathsf{II}}}\big[w_{loc}(0) - w_{loc}(2a_{\mathsf{II}})\big] - 2,$$

where $\nu_+^- \equiv 0$ reflects the translation invariance of the syntopic bump. The eigenvalues $\nu_{\pm}^{\pm}$ are also valid for syntopic bumps with different widths in (3) with reciprocally *symmetric* coupling (discussed in section 2.1.1) by taking $w^{\mathsf{I}}_{lay} = w^{\mathsf{II}}_{lay} = w_{lay}$ but maintaining $a_{\mathsf{I}} \neq a_{\mathsf{II}}$.

Numerical simulations. We examined an extension from the reciprocally symmetric case by varying a single parameter to introduce an asymmetry in the interlayer connections, e.g., one of the amplitudes or space constants associated with one of the interlayer weight functions. The asymmetry in the value of this parameter between the two layers generates a disparity in the strength or the spatial extent of the interlayer connections, and we examined its effect on syntopic and allotopic bumps in the reciprocally asymmetric case. A syntopic bump with equal widths in the reciprocally symmetric case becomes a syntopic bump with different widths as the disparity in the interlayer coupling is increased; the syntopic bump remains stationary, and the bumps in each layer share the same center. Interestingly, the bifurcation with respect to the ν^- eigenmode for $\mathsf{tr}\, \Lambda_- < 0$ (analogous to λ_- in section 2.1.2, associated with the allotopic bump) instead gives rise to a *traveling* allotopic bump, and the speed of the traveling allotopic bump was found to increase with the disparity of the asymmetry in the interlayer coupling from speed 0 in the reciprocally symmetric case. Note that these results were also found to extend to the case of *periodic* bumps, but we omit them here.

Figure 12 shows the evolution from the same initial conditions composed of two spatially offset Gaussian bumps in each layer. The disparity in the interlayer coupling is generated by setting the parameters $A^e_{lay\mathsf{I}} = 0.375$ and $A^e_{lay\mathsf{II}} = 0.5$ apart, and we control the bifurcation with respect to ν^- by varying $\sigma^e_{lay\mathsf{I}}$ (which also contributes to the disparity in the asymmetry). In the right panel in Figure 12 we have set $\sigma^e_{lay\mathsf{I}}$ beyond the bifurcation point so that the syntopic bump is unstable due to $\nu^- > 0$; the plot shows the transient approach of the activity bump in each layer to a traveling allotopic bump with the bumps offset as indicated by the different locations in the threshold points of the activity bump in each layer. Conversely, in the left panel in Figure 12, we set $\sigma^e_{lay\mathsf{I}}$ just prior to the bifurcation point so that $\nu^- < 0$, rendering the syntopic bump stable; the plot shows an initial transient where the activity bumps travel before they slow down and approach the stable syntopic bump.
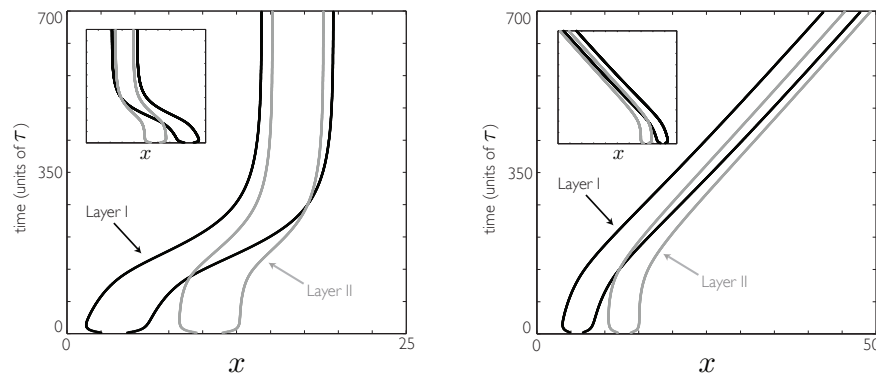
Figure 12. *Bifurcation in numerical simulations of a syntopic bump giving rise to a traveling allotopic bump in an interacting pair of Amari neural fields. The bifurcation occurs with respect to eigenvalue ν_-^-, which here is analogous to the eigenvalue λ_-^- that gives rise to the stationary allotopic bump in the reciprocally symmetric case (2). Regions contained between pairs of curves with similar line style indicate the superthreshold regions for the activity bump in each layer. The bifurcation point occurs at $\sigma_{layI}^e \approx 2.45$. Left: For $\sigma_{layI}^e = 2.2$, starting from an initial condition composed of a localized bump in each layer with a large spatial offset, the bumps travel for a brief duration of time during the transient, with the distance between their centers decreasing to 0 as the activity bumps approach the stable stationary syntopic bump. Right: Setting $\sigma_{layI}^e = 2.5$ so that the stationary syntopic bump is unstable and starting from the same initial condition with a localized bump in each layer separated by a spatially offset, the figure shows the activity bumps approach a purportedly stable traveling allotopic bump. Insets: Switching the initial positioning of the offset bumps leads the bumps to propagate in the opposite direction. Fixed parameters are $A_{loc}^e = \sigma_{loc}^e = A_{loc}^i = 1, \sigma_{loc}^i = 5, A_{layI}^e = 0.375, A_{layII}^e = 0.5, A_{layI}^i = A_{layII}^i = 0.4, \sigma_{layII}^e = \sigma_{layI}^i = \sigma_{layII}^i = 2, \theta = 0.2.*

2.2. Stationary periodic bumps.

We now investigate the existence and linear stability of stationary periodic bumps with period L in the interacting pair of Amari neural fields and show that syntopic and allotopic bumps naturally extend to stationary periodic bumps. A *syntopic periodic bump*, denoted by $\big(\mathcal{P}_s(x), \mathcal{Q}_s(x)\big)^{\mathrm{T}}$, is illustrated in Figure 13(a). The emergence of a syntopic periodic bump is similar to that of a syntopic solitary bump in section 2.1.1. A syntopic periodic bump can undergo a pitchfork bifurcation to an *allotopic periodic bump*, denoted by $\big(\mathcal{P}_o(x), \mathcal{Q}_o(x)\big)^{\mathrm{T}}$ (the $_o$ for *offset*), the existence and linear stability of which is examined in section 2.2.2. A third type of stationary periodic bump, denoted by $\big(\mathcal{P}_a(x), \mathcal{Q}_a(x)\big)^{\mathrm{T}}$, is composed of an L-periodic stationary bump in each layer with a spatial offset c that is exactly half a period ($c = L/2$); we refer to this as an *antisyntopic periodic bump*, which is an allusion as it is the spatial analogue of the *antisynchronous* solution in coupled oscillator theory (see Figure 13(c)). The spatial structure of the eigenmodes in the linearization about the syntopic periodic bump is analogous to the case of a syntopic solitary bump. The pitchfork bifurcation to an allotopic periodic bump is similar; however, in the periodic case, the curve of allotopic bumps can terminate in a pitchfork bifurcation on a branch of antisyntopic periodic bumps (see Figure 14). Moreover, the extension to reciprocally asymmetric interlayer coupling analogously gives rise to a traveling allotopic bump, though we omit these results here. In some parameter regions and for sufficiently large periods L, numerical simulations showed it was possible to approach a stationary solution having a double or triple bump within each period (results not included). We mention that periodic bumps, in a related case, were treated in a PDE with Heaviside nonlinearity [16].
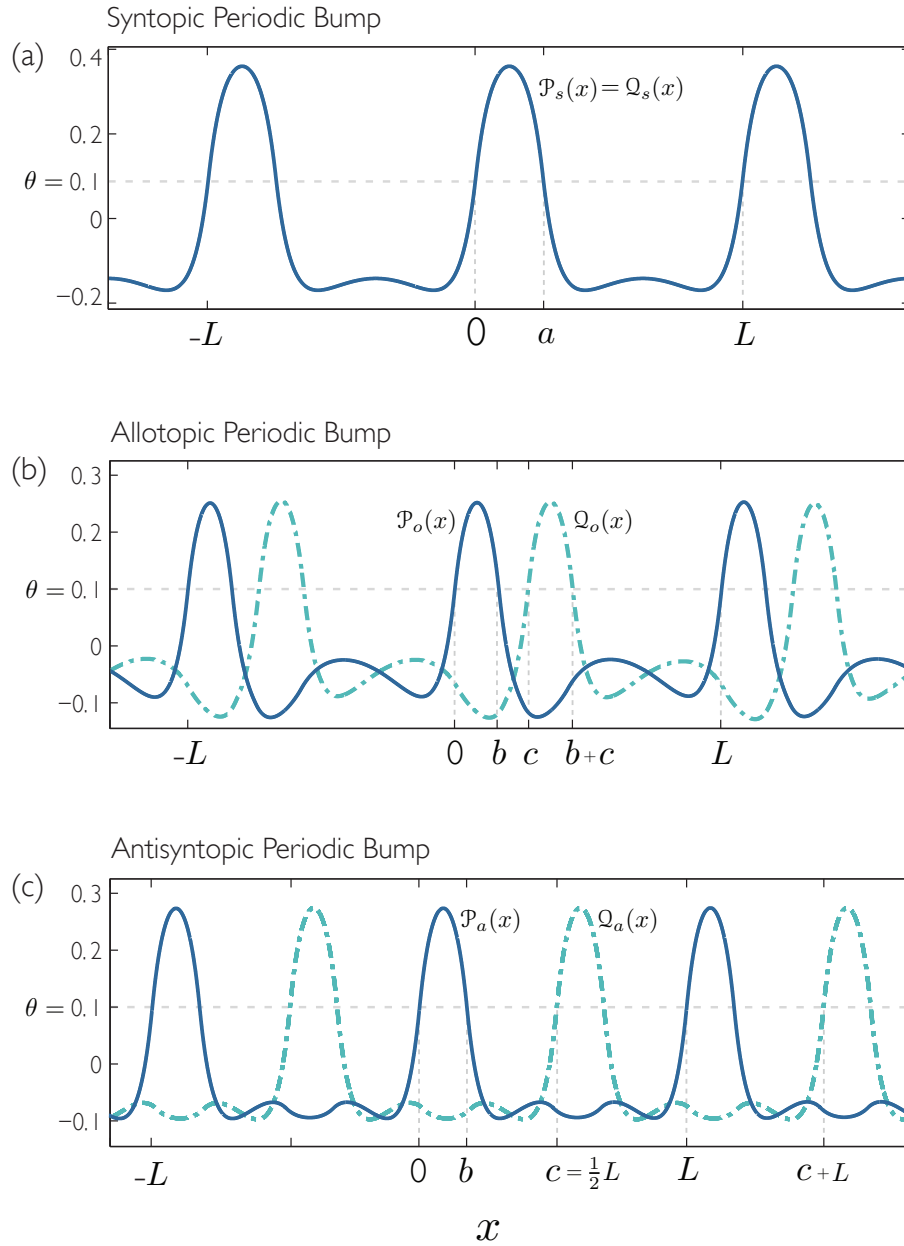
Figure 13. *Various types of stationary periodic bumps in the interacting pair of Amari neural fields where $\mathcal{P}$ is the bump in Layer I and $\mathcal{Q}$ is the bump in Layer II. (a) The stable syntopic periodic bump $\left(\mathcal{P}_s(x), \mathcal{Q}_s(x)\right)^{\mathrm{T}}$ where $\sigma_{lay}^e = 2$, with bump width $a = 3.76$ (or $b = a$, $c = 0$). (b) The stable allotopic (offset) periodic bump $\left(\mathcal{P}_o(x), \mathcal{Q}_o(x)\right)^{\mathrm{T}}$, where $\sigma_{lay}^e = 8$, $b = 2.50$, $c = 3.87$. (c) The antisyntopic periodic bump $\left(\mathcal{P}_a(x), \mathcal{Q}_a(x)\right)^{\mathrm{T}}$, where $\sigma_{lay}^e = 19$, $b = 2.66$, $c = 7.5 = L/2$. Fixed parameters are $A_{loc}^e = \sigma_{loc}^e = 1$, $A_{loc}^i = 1.5$, $\sigma_{loc}^i = 3$, $A_{lay}^i = 0.1$, $\sigma_{lay}^i = 1$, $\theta = 0.1$, and period $L = 15$. The sequence from (a) $\sigma_{lay}^e = 2$ to (b) $\sigma_{lay}^e = 8$ to (c) $\sigma_{lay}^e = 19$ illustrates a supercritical pitchfork bifurcation at $\sigma_{lay}^e \approx 3.17$ of a stable syntopic periodic bump giving rise to a stable allotopic periodic bump; the stable allotopic periodic bump ultimately collides with the unstable antisyntopic periodic bump in a supercritical pitchfork bifurcation that renders the antisyntopic periodic bump stable for $\sigma_{lay}^e \gtrsim 18.34$. The three panels correspond to different points along the bifurcation diagram in Figure 14.*
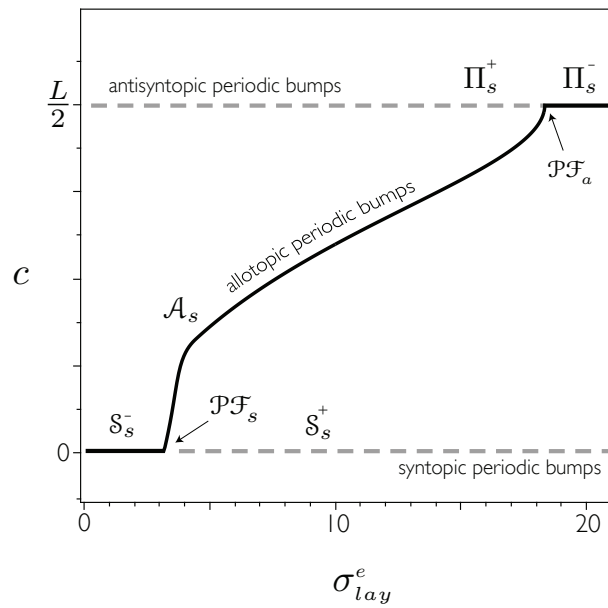
Figure 14. *Bifurcation diagram joining curves of syntopic ($\mathcal{S}_s$), allotopic ($\mathcal{A}_s$), and antisyntopic (Π_s) periodic bumps with period $L = 15$. The diagram illustrates that a pitchfork bifurcation occurs at $\mathcal{PF}_s$ where $\sigma_{lay}^e \approx 3.17$ along branch $\mathcal{S}_s^-$ of stable syntopic periodic bumps and gives rise to curve $\mathcal{A}_s$ of stable allotopic periodic bumps. The distance c between the bumps grows along branch $\mathcal{A}_s$ as σ_{lay}^e increases until $c = L/2$, where the branch of allotopic bumps terminates at a pitchfork bifurcation with branch Π_s^+ of unstable antisyntopic periodic bumps at point $\mathcal{PF}_a$ where $\sigma_{lay}^e \approx 18.34$. Continuing for $\sigma_{lay}^e \gtrsim 18.34$ is branch Π_s^- of stable antisyntopic periodic bumps. The solid (dashed) lines indicate stable (unstable) solutions. Fixed parameters are $A_{loc}^e = \sigma_{loc}^e = 1$, $A_{loc}^i = 1.5$, $\sigma_{loc}^i = 3$, $A_{lay}^e = 0.5$, $A_{lay}^i = 0.1$, $\sigma_{lay}^i = 1$, $\theta = 0.1$. See Figure 13 for related bump profiles.*

2.2.1. Syntopic periodic bumps. The profile of a stationary *syntopic periodic bump with equal widths and period L*, $(u(x,t), v(x,t))^{\mathrm{T}} = (\mathcal{P}_s(x), \mathcal{Q}_s(x))^{\mathrm{T}}$, where $\mathcal{Q}_s(x) = \mathcal{P}_s(x)$ satisfies

$$\mathcal{P}_s(0 + nL) = \mathcal{P}_s(a + nL) = \theta, \quad n \in \mathbb{Z}, \qquad \mathcal{P}_s(x) > \theta, \quad x \in \bigcup_{n \in \mathbb{Z}} (0 + nL, a + nL),$$

with $\mathcal{P}_s(x) < \theta$ otherwise. Consequently, $\mathcal{P}_s(x)$ can be expressed (setting $y = \eta - nL$) as

$$(28) \qquad \mathcal{P}_s(x) = \sum_{n=-\infty}^{\infty} \int_{0+nL}^{a+nL} \left[w_{loc}(x - \eta) + w_{lay}(x - \eta) \right] d\eta$$

$$(29) \qquad = \int_0^a \left[\sum_{n=-\infty}^{\infty} w_{loc}(x - y - nL) + \sum_{n=-\infty}^{\infty} w_{lay}(x - y - nL) \right] dy$$

$$(30) \qquad = \int_0^a \left[w_{loc}^{per}(x - y) + w_{lay}^{per}(x - y) \right] dy$$

$$(31) \qquad = \left[W_{loc}^{per}(x) - W_{loc}^{per}(x - a) \right] + \left[W_{lay}^{per}(x) - W_{lay}^{per}(x - a) \right],$$

where in (30) we defined the even-symmetric and L-periodic function $w_l^{per}(x)$ as

$$(32) \qquad w_l^{per}(x) = \sum_{n=-\infty}^{\infty} w_l(x - nL) \quad \Longrightarrow \quad W_l^{per}(x) = \int_0^x w_l^{per}(y)dy.$$

Consequently, the existence condition for a syntopic periodic bump with period L is

$$(33) \qquad \theta = W_{loc}^{per}(a) + W_{lay}^{per}(a)$$

provided the solution $\mathcal{P}_s$ crosses threshold only at $x = 0$ and $x = a$ in $[0, L]$.

Calculation of w_l^{per} and W_l^{per} for the exponential function. For simulations, we consider

$$w_l(x) = \frac{A_l^e}{2\sigma_l^e} e^{-|x|/\sigma_l^e} - \frac{A_l^i}{2\sigma_l^i} e^{-|x|/\sigma_l^i}, \qquad l \in \{loc, lay\}.$$

The L-periodic kernel $w_l^{per}(x)$ in (32) can be expressed using geometric series as

$$w_l^{per}(x) = \frac{A_l^e}{2\sigma_l^e}\left(\frac{e^{(x-L)/\sigma_l^e} + e^{-x/\sigma_l^e}}{1 - e^{-L/\sigma_l^e}}\right) - \frac{A_l^i}{2\sigma_l^i}\left(\frac{e^{(x-L)/\sigma_l^i} + e^{-x/\sigma_l^i}}{1 - e^{-L/\sigma_l^i}}\right), \quad x \in [0, L].$$

The antiderivative $W_l^{per}(x) = \int_0^x w_l^{per}(y)dy$, for $x \in [-L, 2L]$, is given explicitly by

$$W_l^{per}(x) = \begin{cases} -\mathcal{W}_l^{per}(-x), & x \in [-L, 0), \\ \mathcal{W}_l^{per}(x), & x \in [0, L], \\ \mathcal{W}_l^{per}(x - L) + A_l^e - A_l^i, & x \in (L, 2L], \end{cases}$$

where, restricted to $x \in [0, L]$, the expression for $\mathcal{W}_l^{per}(x)$, for $l \in \{loc, lay\}$, is given by

$$\mathcal{W}_l^{per}(x) = \frac{A_l^e}{2}\left(1 + \frac{e^{(x-L)/\sigma_l^e} - e^{-x/\sigma_l^e}}{1 - e^{-L/\sigma_l^e}}\right) - \frac{A_l^i}{2}\left(1 + \frac{e^{(x-L)/\sigma_l^i} - e^{-x/\sigma_l^i}}{1 - e^{-L/\sigma_l^i}}\right).$$

Linear stability of a syntopic periodic bump. To study the linear stability of a stationary syntopic periodic bump $(\mathcal{P}_s, \mathcal{Q}_s)^\mathrm{T}$, where $\mathcal{Q}_s = \mathcal{P}_s$, we restrict ourselves to the evolution of L-periodic perturbations $(\tilde{\varphi}, \tilde{\psi})^\mathrm{T}$ of the bump by setting $(u, v)^\mathrm{T} = (\mathcal{P}_s, \mathcal{Q}_s)^\mathrm{T} + e^{\lambda t}(\varphi, \psi)^\mathrm{T}$. Although such a restriction does not allow the full range of perturbations, it does match the dynamics in numerical simulations of a single bump on a periodically repeating domain. Linearizing about the syntopic bump accordingly leads to the spectral problem

$$(34) \qquad \begin{aligned} \lambda\varphi &= -\varphi + \mathcal{N}_{loc}^{per}[\mathcal{P}_s]\,\varphi + \mathcal{N}_{lay}^{per}[\mathcal{P}_s]\,\psi, \\ \lambda\psi &= -\psi + \mathcal{N}_{loc}^{per}[\mathcal{P}_s]\,\psi + \mathcal{N}_{lay}^{per}[\mathcal{P}_s]\,\varphi, \end{aligned}$$

where the operators $\mathcal{N}_l^{per}[\mathcal{P}]$ for $l \in \{loc, lay\}$ and $\mathcal{P}(x) > \theta$ for $x \in (a_\mathrm{L}, a_\mathrm{R})$ are given by

$$(35) \qquad \mathcal{N}_l^{per}[\mathcal{P}]\,\phi = w_l^{per} * \left[\delta(\mathcal{P} - \theta)\,\phi\right] = \frac{w_l^{per}(x - a_\mathrm{L})}{|\mathcal{P}'(a_\mathrm{L})|}\,\phi(a_\mathrm{L}) + \frac{w_l^{per}(x - a_\mathrm{R})}{|\mathcal{P}'(a_\mathrm{R})|}\,\phi(a_\mathrm{R}).$$

From symmetry conditions $|\mathcal{P}'_s(0)| = |\mathcal{P}'_s(a)| = \left[w_{loc}^{per}(0) - w_{loc}^{per}(a)\right] + \left[w_{lay}^{per}(0) - w_{lay}^{per}(a)\right] > 0$. The spectral problem (34) has a structure similar to that of (11), and its solutions follow

analogously from calculations in section 2.1.1 with the periodic weight function w_l^{per} instead of w_l, the solitary bump $\mathcal{U}_s$ replaced with the periodic bump $\mathcal{P}_s$, and the width a calculated from (33). Setting $\zeta = |\mathcal{P}'_s(0)|$, the two pairs of eigenvalues $\lambda_\pm^+(a)$ and $\lambda_\pm^-(a)$ are given by

$$\lambda_+^+(a) = \tfrac{2}{\zeta}\big(w_{loc}^{per}(a) + w_{lay}^{per}(a)\big), \qquad \lambda_-^+(a) = \tfrac{2}{\zeta}\big(w_{loc}^{per}(a) - w_{lay}^{per}(0)\big),$$

$$\lambda_+^-(a) = 0, \qquad\qquad\qquad\qquad \lambda_-^-(a) = -\tfrac{2}{\zeta}\big(w_{lay}^{per}(0) - w_{lay}^{per}(a)\big).$$

The associated eigenfunctions can be calculated along the lines of Appendix A.

2.2.2. Allotopic periodic bumps. Analogous to section 2.1.2, a stationary allotopic periodic bump has the form $(u(x,t), v(x,t))^{\mathrm{T}} = (\mathcal{P}_o(x), \mathcal{Q}_o(x))^{\mathrm{T}}$, where $\mathcal{Q}_o(x) = \mathcal{P}_o\big(-(x-c-b)\big)$.

Existence of an allotopic periodic bump with period L. The stationary bumps $\mathcal{P}_o(x)$ in Layer I and $\mathcal{Q}_o(x)$ in Layer II satisfy the threshold conditions

$$\mathcal{P}_o(0 + nL) = \mathcal{P}_o(b + nL) = \theta, \qquad \mathcal{Q}_o(c + nL) = \mathcal{Q}_o(c + b + nL) = \theta, \qquad n \in \mathbb{Z},$$

and $\mathcal{P}_o, \mathcal{Q}_o$ are superthreshold over

$$\mathcal{P}_o(x) > \theta, \quad x \in \bigcup_{n \in \mathbb{Z}} (0 + nL, a + nL), \qquad \mathcal{Q}_o(x) > \theta, \quad x \in \bigcup_{n \in \mathbb{Z}} (c + nL, b + c + nL),$$

and are subthreshold otherwise (see Figure 13). It is assumed that $(0, b), (c, b + c) \subset [0, L]$ and that $\mathcal{P}_o, \mathcal{Q}_o$ satisfy periodic boundary conditions at $x = 0$ and $x = L$. Under the above conditions, the allotopic bump profile and the existence conditions can be expressed as in section 2.1.2 using (18) and (20) with W_l replaced with W_l^{per} which determine the bump width b and spatial offset c (see Figure 13(b)).

Linear stability for an allotopic periodic bump with period L. The analysis for an allotopic periodic bump follows analogously from the solitary bump case in section 2.1.2 with w_l replaced by w_l^{per}, $\mathcal{U}$ replaced by $\mathcal{P}$, and b and c calculated for an allotopic periodic bump. Regarding the branch of stable allotopic periodic bumps $\mathcal{A}_s$ in Figure 14, the direction of bifurcation, the linear stability analysis, and the numerical simulations were all in agreement. Not shown in Figure 14 is a branch of *unstable* allotopic periodic bumps that bifurcates from a coexistent branch of *unstable* syntopic periodic bumps (analogous to the solid gray curves in Figure 11).

2.2.3. Antisyntopic periodic bumps. Next we consider the existence and linear stability of an antisyntopic periodic bump, characterized as an allotopic bump with the distance c between the bumps spanning half a period ($c = \frac{L}{2}$). The term antisyntopic periodic bump is an allusion to the antisynchronous solution arising in coupled oscillator theory. From symmetry and periodicity, the antisyntopic periodic bump is given by $(u(x,t), v(x,t))^{\mathrm{T}} = (\mathcal{P}_a(x), \mathcal{Q}_a(x))^{\mathrm{T}}$ where $\mathcal{Q}_a(x) = \mathcal{P}_a\big(-(x - b - \frac{L}{2})\big)$, and $(\mathcal{P}_a, \mathcal{Q}_a)^{\mathrm{T}}$ satisfies the same conditions as the allotopic bump $(\mathcal{P}_o, \mathcal{Q}_o)^{\mathrm{T}}$ with $c = \frac{L}{2}$. The antisyntopic periodic bump is a special type of allotopic periodic bump because the periodic bumps in each layer are even-symmetric about their maxima due to the symmetry of the L-periodic weight functions w_{loc}^{per} and w_{lay}^{per}.

Existence equations for an antisyntopic periodic bump with period L. The existence conditions for the antisyntopic periodic bump are the same as those for the allotopic periodic

bump with $c = \frac{L}{2}$ where L is the period, and it is helpful to use the alternate form (cf. (20)), which, for the antisyntopic periodic bump, translates to

$$(36) \qquad 2W_{loc}^{per}(b) + W_{lay}^{per}\left(\tfrac{L}{2} + b\right) - W_{lay}^{per}\left(\tfrac{L}{2} - b\right) = 2\theta,$$

$$(37) \qquad 2W_{lay}^{per}\left(\tfrac{L}{2}\right) - W_{lay}^{per}\left(\tfrac{L}{2} + b\right) - W_{lay}^{per}\left(\tfrac{L}{2} - b\right) = 0.$$

The periodic bump width b is the only unknown; however, system (36)–(37) is not over-constrained because (37) is automatically satisfied. The proof is straightforward and is outlined as follows. Since w_l^{per} for $l \in \{loc,lay\}$ is L-periodic and even-symmetric about 0, then w_l^{per} is even-symmetric about $L/2$. This further implies that W_l^{per} is odd-symmetric about $L/2$, and it is straightforward to show that $W_l^{per}\left(\frac{L}{2}\right) - W_l^{per}\left(\frac{L}{2} - b\right) = -\left[W_l^{per}\left(\frac{L}{2}\right) - W_l^{per}\left(\frac{L}{2} + b\right)\right]$. This is equivalent to (37) and is identically satisfied under the above assumptions. Thus (36) solely determines existence of the antisyntopic periodic bump with period L.

Linear stability of an antisyntopic periodic bump. Linearizing about the antisyntopic periodic bump $(\mathcal{P}_a, \mathcal{Q}_a)$ and restricting to the class of L-periodic perturbations by setting $(u,v)^{\mathrm{T}} = (\mathcal{P}_a, \mathcal{Q}_a)^{\mathrm{T}} + e^{\lambda t}(\varphi, \psi)^{\mathrm{T}}$ yields the following spectral problem for ν and $(\varphi(x), \psi(x))^{\mathrm{T}}$:

$$(38) \qquad \begin{aligned} \nu\varphi &= -\varphi + \mathcal{N}_{loc}^{per}[\mathcal{P}_a]\varphi + \mathcal{N}_{lay}^{per}[\mathcal{Q}_a]\psi, \\ \nu\psi &= -\psi + \mathcal{N}_{loc}^{per}[\mathcal{Q}_a]\psi + \mathcal{N}_{lay}^{per}[\mathcal{P}_a]\varphi, \end{aligned}$$

where $\mathcal{N}_l^{per}[\mathcal{P}]$ for $l \in \{loc,lay\}$ and $\mathcal{P} \in \{\mathcal{P}_a, \mathcal{Q}_a\}$ is defined in (35). From symmetry conditions, $|\mathcal{P}_a'(0)| = |\mathcal{P}_a'(0 + nL)| = |\mathcal{P}_a'(b + nL)| = |\mathcal{Q}_a'(\frac{L}{2} + nL)| = |\mathcal{Q}_a'(b + \frac{L}{2} + nL)|$ for all $n \in \mathbb{Z}$.

Setting $x = 0$ and $x = b$ in the first equation and $x = \frac{L}{2}$ and $x = b + \frac{L}{2}$ in the second equation of (38) results in the compatibility matrix equation

$$\left(\mathrm{M}_a - \mathrm{I}_4\right)\boldsymbol{v} = \nu\boldsymbol{v},$$

$$\mathrm{M}_a = \begin{bmatrix} \mathring{w}_{loc}^{per}(0) & \mathring{w}_{loc}^{per}(b) & \mathring{w}_{lay}^{per}(\tfrac{L}{2}) & \mathring{w}_{lay}^{per}(\tfrac{L}{2}+b) \\ \mathring{w}_{loc}^{per}(b) & \mathring{w}_{loc}^{per}(0) & \mathring{w}_{lay}^{per}(\tfrac{L}{2}-b) & \mathring{w}_{lay}^{per}(\tfrac{L}{2}) \\ \mathring{w}_{lay}^{per}(\tfrac{L}{2}) & \mathring{w}_{lay}^{per}(\tfrac{L}{2}-b) & \mathring{w}_{loc}^{per}(0) & \mathring{w}_{loc}^{per}(b) \\ \mathring{w}_{lay}^{per}(\tfrac{L}{2}+b) & \mathring{w}_{lay}^{per}(\tfrac{L}{2}) & \mathring{w}_{loc}^{per}(b) & \mathring{w}_{loc}^{per}(0) \end{bmatrix}, \quad \boldsymbol{v} = \begin{pmatrix} \varphi(0) \\ \varphi(b) \\ \psi(\tfrac{L}{2}) \\ \psi(\tfrac{L}{2}+b) \end{pmatrix},$$

where $\mathring{w}_l^{per}(x) = w_l^{per}(x)/|\mathcal{P}_a'(0)|$. Since $\mathring{w}_l^{per}$ is even-symmetric about $\frac{L}{2}$, then $\mathring{w}_l^{per}(\frac{L}{2} - b) = \mathring{w}_l^{per}(\frac{L}{2} + b)$ and matrix M_a has the same block structure as matrix M_s in Appendix A. Setting $\xi = |\mathcal{P}_a'(0)| = [w_{loc}^{per}(0) - w_{loc}^{per}(b)] + [w_{lay}^{per}\left(\frac{L}{2}\right) - w_{lay}^{per}\left(b + \frac{L}{2}\right)] > 0$, the four eigenvalues ν are

$$\nu_+^+(b) = \tfrac{2}{\xi}\left(w_{loc}^{per}(b) + w_{lay}^{per}(b + \tfrac{L}{2})\right), \qquad \nu_-^+(b) = \tfrac{2}{\xi}\left(w_{loc}^{per}(b) - w_{lay}^{per}(\tfrac{L}{2})\right),$$

$$\nu_+^-(b) = 0, \qquad\qquad\qquad\qquad \nu_-^-(b) = -\tfrac{2}{\xi}\left(w_{lay}^{per}(\tfrac{L}{2}) - w_{lay}^{per}(b + \tfrac{L}{2})\right).$$

The eigenfunctions are calculated following the procedure illustrated in Appendix A. The eigenvalues can be used to determine the stability along the curve Π_s in Figure 14 and the expression for $\nu_-^- = 0$ is indeed satisfied numerically at the point where the branch $\mathcal{A}_s$ of allotopic periodic bumps terminates in a pitchfork bifurcation with the branch Π_s^- of antisyntopic periodic bumps.

3. A pair of interacting E-I neural fields. We now consider the evolution of an interacting pair of E-I neural fields $(u_e(x,t), u_i(x,t))^{\mathrm{T}}$ and $(v_e(x,t), v_i(x,t))^{\mathrm{T}}$

$$(39) \quad \text{(Layer I)} \qquad \begin{aligned} \partial_t u_e &= -u_e + F_e^{loc}(u_e, u_i) + F_e^{lay}(v_e), \\ \tau \partial_t u_i &= -u_i + F_i^{loc}(u_e, u_i) + F_i^{lay}(v_e), \end{aligned}$$

$$(40) \quad \text{(Layer II)} \qquad \begin{aligned} \partial_t v_e &= -v_e + F_e^{loc}(v_e, v_i) + F_e^{lay}(u_e), \\ \tau \partial_t v_i &= -v_i + F_i^{loc}(v_e, v_i) + F_i^{lay}(u_e), \end{aligned}$$

where $\tau = \tau_i/\tau_e$, with identical *local* synaptic connectivity w_{uv}^{loc} for $u,v \in \{e,i\}$ (cf. [7]),

$$F_e^{loc}(u,v) = w_{ee}^{loc} * H(u - \theta_e) - w_{ei}^{loc} * H(v - \theta_i),$$

$$F_i^{loc}(u,v) = w_{ie}^{loc} * H(u - \theta_e) - w_{ii}^{loc} * H(v - \theta_i),$$

and reciprocally symmetric *interlayer* synaptic coupling w_{ue}^{lay} for $u \in \{e,i\}$, which projects from the E population in each layer to both the E and I populations in the opposite layer so that

$$F_e^{lay}(u) = w_{ee}^{lay} * H(u - \theta_e), \qquad F_i^{lay}(u) = w_{ie}^{lay} * H(u - \theta_e).$$

θ_e and θ_i are the firing thresholds in the excitatory and inhibitory populations, respectively. All weight functions $w_{uv}^l(x)$ for $u,v \in \{e,i\}$ and $l \in \{loc,lay\}$ are assumed to be even-symmetric, positive, and monotonically decreasing to 0 as $x \longrightarrow \infty$, and, for calculations, we use

$$w_{uv}^l(x) = \frac{A_{uv}^l}{2\sigma_{uv}^l} e^{(-|x|/\sigma_{uv}^l)}, \qquad u,v \in \{e,i\}, \quad l \in \{loc,lay\}.$$

3.1. Existence of syntopic bumps. Since the two E-I subnetworks are identical and the interlayer connections are reciprocally symmetric, a stationary syntopic bump has the form $(u_e(x,t), u_i(x,t), v_e(x,t), v_i(x,t))^{\mathrm{T}} = (\mathcal{U}_e^s(x), \mathcal{U}_i^s(x), \mathcal{V}_e^s(x), \mathcal{V}_i^s(x))^{\mathrm{T}}$, where the bumps in the two layers are identical so that $(\mathcal{V}_e^s, \mathcal{V}_i^s)^{\mathrm{T}} = (\mathcal{U}_e^s, \mathcal{U}_i^s)^{\mathrm{T}}$. We require $\mathcal{U}_e^s(x) > \theta_e$ over $(-a,a)$ and $\mathcal{U}_i^s(x) > \theta_i$ over $(-b,b)$ with $\mathcal{U}_e^s, \mathcal{U}_i^s$ subthreshold otherwise, satisfying $\mathcal{U}_e^s(x), \mathcal{U}_i^s(x) \longrightarrow 0$ as $x \to \pm\infty$. The profiles $\mathcal{U}_e^s, \mathcal{U}_i^s$ must then satisfy the threshold conditions

$$(41) \qquad \mathcal{U}_e^s(-a) = \mathcal{U}_e^s(a) = \theta_e, \qquad \mathcal{U}_i^s(-b) = \mathcal{U}_i^s(b) = \theta_i$$

to determine the existence of the *syntopic bump halfwidths* a and b for the E and I populations, respectively. By defining $W_{uv}^l(x) = \int_0^x w_{uv}^l(y)dy$, for $l \in \{loc,lay\}$ and $u,v \in \{e,i\}$, and

$$(42) \qquad \mathcal{W}_{uv}^l(x\,;\alpha) = W_{uv}^l(x + \alpha) - W_{uv}^l(x - \alpha),$$

the *stationary syntopic bump* $(\mathcal{U}_e^s(x), \mathcal{U}_i^s(x), \mathcal{V}_e^s(x), \mathcal{V}_i^s(x))^{\mathrm{T}}$ can then be expressed as

$$(43) \qquad \mathcal{U}_e^s(x) = \mathcal{W}_{ee}^{loc}(x\,;a) - \mathcal{W}_{ei}^{loc}(x\,;b) + \mathcal{W}_{ee}^{lay}(x\,;a), \qquad \mathcal{V}_e^s(x) = \mathcal{U}_e^s(x),$$

$$(44) \qquad \mathcal{U}_i^s(x) = \mathcal{W}_{ie}^{loc}(x\,;a) - \mathcal{W}_{ii}^{loc}(x\,;b) + \mathcal{W}_{ie}^{lay}(x\,;a), \qquad \mathcal{V}_i^s(x) = \mathcal{U}_i^s(x).$$

Consequently, the existence condition (41) for a and b can be expressed as

$$(45) \qquad \begin{aligned} \mathcal{U}_e^s(a) &= \theta_e, \\ \mathcal{U}_i^s(b) &= \theta_i, \end{aligned} \quad \Longrightarrow \quad \begin{aligned} \mathcal{W}_{ee}^{loc}(a\,;a) - \mathcal{W}_{ei}^{loc}(a\,;b) + \mathcal{W}_{ee}^{lay}(a\,;a) &= \theta_e, \\ \mathcal{W}_{ie}^{loc}(b\,;a) - \mathcal{W}_{ii}^{loc}(b\,;b) + \mathcal{W}_{ie}^{lay}(b\,;a) &= \theta_i, \end{aligned}$$

guaranteeing existence of the syntopic bump provided all assumptions are satisfied.

3.2. Linear stability of syntopic bumps.

Linearizing about the syntopic bump and setting

$$u_e(x,t) = \mathcal{U}_e^s(x) + \varphi_e(x)e^{\lambda t}, \qquad\qquad v_e(x,t) = \mathcal{V}_e^s(x) + \psi_e(x)e^{\lambda t},$$
$$u_i(x,t) = \mathcal{U}_i^s(x) + \varphi_i(x)e^{\lambda t}, \qquad\qquad v_i(x,t) = \mathcal{V}_i^s(x) + \psi_i(x)e^{\lambda t}$$

yields the following spectral problem for λ and $\boldsymbol{\phi}(x) = (\varphi_e(x), \varphi_i(x), \psi_e(x), \psi_i(x))^{\mathrm{T}}$:

$$(46) \qquad\qquad \lambda\varphi_e = -\varphi_e + \mathcal{N}_{ee}^{loc}\varphi_e - \mathcal{N}_{ei}^{loc}\varphi_i + \mathcal{N}_{ee}^{lay}\psi_e,$$

$$(47) \qquad\qquad \tau\lambda\varphi_i = -\varphi_i + \mathcal{N}_{ie}^{loc}\varphi_e - \mathcal{N}_{ii}^{loc}\varphi_i + \mathcal{N}_{ie}^{lay}\psi_e,$$

$$(48) \qquad\qquad \lambda\psi_e = -\psi_e + \mathcal{N}_{ee}^{loc}\psi_e - \mathcal{N}_{ei}^{loc}\psi_i + \mathcal{N}_{ee}^{lay}\varphi_e,$$

$$(49) \qquad\qquad \tau\lambda\psi_i = -\psi_i + \mathcal{N}_{ie}^{loc}\psi_e - \mathcal{N}_{ii}^{loc}\psi_i + \mathcal{N}_{ie}^{lay}\varphi_e.$$

The operators in (46)–(49), where $l \in \{loc,lay\}$, $u,v \in \{e,i\}$ with $\alpha_e = a$, $\alpha_i = b$, are given by

$$\mathcal{N}_{uv}^l\phi(x) = \int_{\mathbb{R}} w_{uv}^l(x-y)\,\delta\big(\mathcal{U}_v^s(y) - \theta_v\big)\phi(y)\,dy = \frac{w_{uv}^l(x+\alpha_v)}{\left|\frac{d\mathcal{U}_v^s}{dx}(-\alpha_v)\right|}\phi(-\alpha_v) + \frac{w_{uv}^l(x-\alpha_v)}{\left|\frac{d\mathcal{U}_v^s}{dx}(\alpha_v)\right|}\phi(\alpha_v).$$

The operators $\mathcal{N}_{uv}^l$ are compact and the essential spectrum is $\{-1, -\tau^{-1}\}$, which does not lead to instability. The point spectrum is calculated by substituting $x = \pm a$ into (46), (48) and $x = \pm b$ into (47), (49) and deriving the compatibility matrix equation

$$(\mathrm{M}_{\mathrm{EI}}^s - \mathrm{I}_{\mathrm{EI}})\,\boldsymbol{v} = \lambda\boldsymbol{v},$$

which determines the eigenvalues λ and associated vectors $\boldsymbol{v}$, where

$$\boldsymbol{v} = \big(\varphi_e(-a), \varphi_e(a), \varphi_i(-b), \varphi_i(b), \psi_e(-a), \psi_e(a), \psi_i(-b), \psi_i(b)\big)^{\mathrm{T}}.$$

Substituting the elements of $\boldsymbol{v}$ into (46)–(49) determines the *eigenfunction* $\boldsymbol{\phi}(x)$ for λ. The $8{\times}8$ matrix $\mathrm{I}_{\mathrm{EI}} = \mathsf{diag}\,(1, 1, \tau^{-1}, \tau^{-1}, 1, 1, \tau^{-1}, \tau^{-1})$ and $\mathrm{M}_{\mathrm{EI}}^s$ are given by

$$\mathrm{M}_{loc} = \begin{bmatrix} \hat{w}_{ee}^{loc}(0) & \hat{w}_{ee}^{loc}(2a) & -\hat{w}_{ei}^{loc}(a-b) & -\hat{w}_{ei}^{loc}(a+b) \\ \hat{w}_{ee}^{loc}(2a) & \hat{w}_{ee}^{loc}(0) & -\hat{w}_{ei}^{loc}(a+b) & -\hat{w}_{ei}^{loc}(a-b) \\ \frac{1}{\tau}\hat{w}_{ie}^{loc}(a-b) & \frac{1}{\tau}\hat{w}_{ie}^{loc}(a+b) & -\frac{1}{\tau}\hat{w}_{ii}^{loc}(0) & -\frac{1}{\tau}\hat{w}_{ii}^{loc}(2b) \\ \frac{1}{\tau}\hat{w}_{ie}^{loc}(a+b) & \frac{1}{\tau}\hat{w}_{ie}^{loc}(a-b) & -\frac{1}{\tau}\hat{w}_{ii}^{loc}(2b) & -\frac{1}{\tau}\hat{w}_{ii}^{loc}(0) \end{bmatrix},$$

$$\mathrm{M}_{\mathrm{EI}}^s = \begin{bmatrix} \mathrm{M}_{loc} & \mathrm{M}_{lay} \\ \mathrm{M}_{lay} & \mathrm{M}_{loc} \end{bmatrix},$$

$$\mathrm{M}_{lay} = \begin{bmatrix} \hat{w}_{ee}^{lay}(0) & \hat{w}_{ee}^{lay}(2a) & 0 & 0 \\ \hat{w}_{ee}^{lay}(2a) & \hat{w}_{ee}^{lay}(0) & 0 & 0 \\ \frac{1}{\tau}\hat{w}_{ie}^{lay}(a-b) & \frac{1}{\tau}\hat{w}_{ie}^{lay}(a+b) & 0 & 0 \\ \frac{1}{\tau}\hat{w}_{ie}^{lay}(a+b) & \frac{1}{\tau}\hat{w}_{ie}^{lay}(a-b) & 0 & 0 \end{bmatrix},$$

and, to simplify expressions in the matrices, for $l \in \{loc,lay\}$ and $v \in \{e,i\}$ we have defined

$$(50) \qquad \hat{w}_{ve}^l(x) = \frac{w_{ve}^l(x)}{\gamma_e}, \qquad \hat{w}_{vi}^l(x) = \frac{w_{vi}^l(x)}{\gamma_i}, \qquad \gamma_e = \left|\frac{d}{dx}\mathcal{U}_e^s(a)\right|, \qquad \gamma_i = \left|\frac{d}{dx}\mathcal{U}_i^s(b)\right|.$$
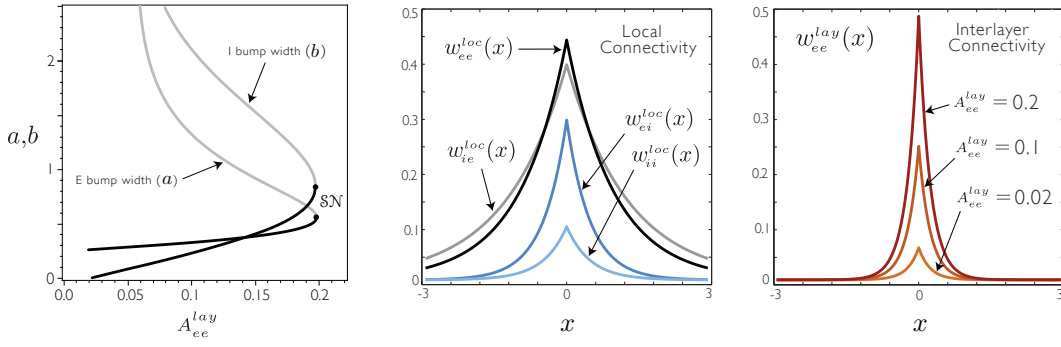
Figure 15. *Left: Bifurcation diagram for the existence of syntopic bumps in the pair of interacting E-I layers where the bifurcation parameter is the strength of interlayer coupling A_{ee}^{lay} to the excitatory population and there are no interlayer connections to the inhibitory population ($A_{ie}^{lay} = 0$). Solid black (gray) lines denote stable (unstable) syntopic bumps, with one curve representing the dependence of the halfwidth a of the (identical) bumps in the excitatory layers and the other curve showing the dependence of the halfwidth b of the (identical) bumps in the inhibitory layers. SN denotes a saddle-node bifurcation of syntopic bumps which occurs at $\sigma_{ee}^{lay} \approx 0.197$, and the stable branch of syntopic bumps terminates at $\sigma_{ee}^{lay} \approx 0.024$ where b approaches 0. Middle: Graphs of the local synaptic weight functions for the fixed parameters. Right: Graphs of the weight function w_{ee}^{lay} for different values of the bifurcation parameter σ_{ee}^{lay} spanning the range of existence of the syntopic bumps in the bifurcation diagram. Fixed parameters: $A_{ee}^{loc} = 0.9, \sigma_{ee}^{loc} = 1, A_{ie}^{loc} = 1.05, \sigma_{ie}^{loc} = 1.3, A_{ei}^{loc} = 0.3, \sigma_{ei}^{loc} = 0.5, A_{ii}^{loc} = 0.12, \sigma_{ii}^{loc} = 0.5, \sigma_{ee}^{lay} = 0.1, A_{ie}^{lay} = 0, \theta_e = 0.2, \theta_i = 0.2, \tau = 1.$*

Eigenvalues. In Appendix D, we show that $(\mathrm{M}_{\mathrm{EI}}^s - \mathrm{I}_{\mathrm{EI}})$ is similar to $\Lambda_{\mathrm{EI}} = \mathsf{diag}(\Lambda_1, \Lambda_2, \Lambda_3, \Lambda_4)$ where the 2×2 submatrices Λ_n, for $n = 1, \dots, 4$, yield the following four pairs of eigenvalues:

$$\lambda_1^\pm = +\tfrac{1}{2}\Big[\tfrac{1}{\gamma_e}\big(w_{ee}^{loc}(0) + w_{ee}^{loc}(2a) + w_{ee}^{lay}(0) + w_{ee}^{lay}(2a)\big) + \tfrac{1}{\gamma_i \tau}\big(-w_{ii}^{loc}(0) - w_{ii}^{loc}(2b)\big) - 1 - \tfrac{1}{\tau}\Big]$$
$$\pm \tfrac{1}{2}\Big\{\Big[\tfrac{1}{\gamma_e}\big(w_{ee}^{loc}(0) + w_{ee}^{loc}(2a) + w_{ee}^{lay}(0) + w_{ee}^{lay}(2a)\big) - \tfrac{1}{\gamma_i \tau}\big(-w_{ii}^{loc}(0) - w_{ii}^{loc}(2b)\big) - 1 + \tfrac{1}{\tau}\Big]^2$$
$$+ \tfrac{4}{\gamma_e \gamma_i \tau}\big[-w_{ei}^{loc}(a-b) - w_{ei}^{loc}(a+b)\big]\big[w_{ie}^{loc}(a-b) + w_{ie}^{loc}(a+b) + w_{ie}^{lay}(a+b) + w_{ie}^{lay}(a-b)\big]\Big\}^{1/2},$$

$$\lambda_2^\pm = +\tfrac{1}{2}\Big[\tfrac{1}{\gamma_e}\big(w_{ee}^{loc}(0) - w_{ee}^{loc}(2a) + w_{ee}^{lay}(0) - w_{ee}^{lay}(2a)\big) + \tfrac{1}{\gamma_i \tau}\big(-w_{ii}^{loc}(0) + w_{ii}^{loc}(2b)\big) - 1 - \tfrac{1}{\tau}\Big]$$
$$\pm \tfrac{1}{2}\Big\{\Big[\tfrac{1}{\gamma_e}\big(w_{ee}^{loc}(0) - w_{ee}^{loc}(2a) + w_{ee}^{lay}(0) - w_{ee}^{lay}(2a)\big) - \tfrac{1}{\gamma_i \tau}\big(-w_{ii}^{loc}(0) + w_{ii}^{loc}(2b)\big) - 1 + \tfrac{1}{\tau}\Big]^2$$
$$+ \tfrac{4}{\gamma_e \gamma_i \tau}\big[-w_{ei}^{loc}(a-b) + w_{ei}^{loc}(a+b)\big]\big[w_{ie}^{loc}(a-b) - w_{ie}^{loc}(a+b) + w_{ie}^{lay}(a+b) - w_{ie}^{lay}(a-b)\big]\Big\}^{1/2},$$

$$\lambda_3^\pm = +\tfrac{1}{2}\Big[\tfrac{1}{\gamma_e}\big(w_{ee}^{loc}(0) + w_{ee}^{loc}(2a) - w_{ee}^{lay}(0) - w_{ee}^{lay}(2a)\big) + \tfrac{1}{\gamma_i \tau}\big(-w_{ii}^{loc}(0) - w_{ii}^{loc}(2b)\big) - 1 - \tfrac{1}{\tau}\Big]$$
$$\pm \tfrac{1}{2}\Big\{\Big[\tfrac{1}{\gamma_e}\big(w_{ee}^{loc}(0) + w_{ee}^{loc}(2a) - w_{ee}^{lay}(0) - w_{ee}^{lay}(2a)\big) - \tfrac{1}{\gamma_i \tau}\big(-w_{ii}^{loc}(0) - w_{ii}^{loc}(2b)\big) - 1 + \tfrac{1}{\tau}\Big]^2$$
$$+ \tfrac{4}{\gamma_e \gamma_i \tau}\big[-w_{ei}^{loc}(a-b) - w_{ei}^{loc}(a+b)\big]\big[w_{ie}^{loc}(a-b) + w_{ie}^{loc}(a+b) - w_{ie}^{lay}(a+b) - w_{ie}^{lay}(a-b)\big]\Big\}^{1/2},$$

$$\lambda_4^\pm = +\tfrac{1}{2}\Big[\tfrac{1}{\gamma_e}\big(w_{ee}^{loc}(0) - w_{ee}^{loc}(2a) - w_{ee}^{lay}(0) + w_{ee}^{lay}(2a)\big) + \tfrac{1}{\gamma_i \tau}\big(-w_{ii}^{loc}(0) + w_{ii}^{loc}(2b)\big) - 1 - \tfrac{1}{\tau}\Big]$$
$$\pm \tfrac{1}{2}\Big\{\Big[\tfrac{1}{\gamma_e}\big(w_{ee}^{loc}(0) - w_{ee}^{loc}(2a) - w_{ee}^{lay}(0) + w_{ee}^{lay}(2a)\big) - \tfrac{1}{\gamma_i \tau}\big(-w_{ii}^{loc}(0) + w_{ii}^{loc}(2b)\big) - 1 + \tfrac{1}{\tau}\Big]^2$$
$$+ \tfrac{4}{\gamma_e \gamma_i \tau}\big[-w_{ei}^{loc}(a-b) + w_{ei}^{loc}(a+b)\big]\big[w_{ie}^{loc}(a-b) - w_{ie}^{loc}(a+b) - w_{ie}^{lay}(a+b) + w_{ie}^{lay}(a-b)\big]\Big\}^{1/2}.$$

Eigenfunctions and spatial structure. In Appendix D, Table 3 lists the four associated pairs of eigenfunctions $\phi_n^\pm(x)$ for $n = 1, \dots, 4$ which have either even- or odd-symmetry.
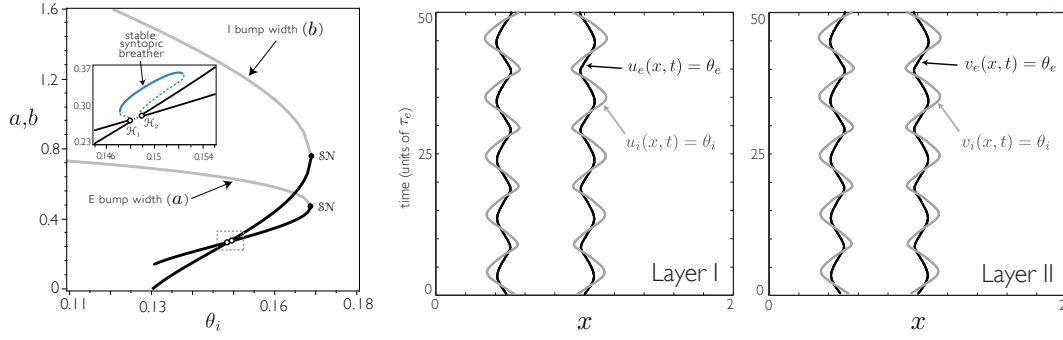
Figure 16. *Left: Bifurcation diagram for the existence of syntopic bumps in the pair of interacting E-I layers where the bifurcation parameter is the threshold of the inhibitory population θ_i. Solid black (gray) curves represent stable (unstable) syntopic bumps with the two curves showing the dependence of the halfwidths a and b on the bifurcation parameter θ_i. $\mathcal{SN}$ denotes a saddle-node bifurcation of syntopic bumps which occurs at $\theta_i \approx 0.1687$, and the stable branch of syntopic bumps terminates at $\theta_i \approx 0.13$ where b approaches 0. The dashed-lined box identifies the region highlighted by the inset, which shows a pair of Hopf bifurcations, denoted by $\mathcal{H}_1$ and $\mathcal{H}_2$, that have destabilized a segment of the branch of stable syntopic bumps (black dotted line) due to the complex conjugate pair of eigenvalues $\lambda_1^{\pm}$ whose real part is positive over the interval of θ_i. $\mathcal{H}_1$ occurs at $\theta_i \approx 0.14815$, and $\mathcal{H}_2$ occurs at $\theta_i \approx 0.14895$. The solid blue curve denotes a branch of stable syntopic breathers which were found in numerical simulations to persist over the approximate interval $(0.1474, 0.1525)$. Simulations suggest that the Hopf bifurcations are subcritical with an unstable solution (dashed blue line) that is detectable in the flow and diverts solutions either to the stable (stationary) syntopic bump or to the stable syntopic breather. Note that the blue curves are for schematic purposes to indicate the interval over which the breathers exist in simulations. Middle and right: The syntopic breather for $\theta_i = 0.15$ which is composed of identical breathers in each layer, with the solid black (gray) curves denoting the threshold boundaries for the activity bump in the excitatory (inhibitory) populations. Fixed parameters: $A_{ee}^{loc} = 1, \sigma_{ee}^{loc} = 0.9, A_{ie}^{loc} = 1.3, \sigma_{ie}^{loc} = 1.4, A_{ei}^{loc} = 0.3, \sigma_{ei}^{loc} = 0.5, A_{ii}^{loc} = 0.2, \sigma_{ii}^{loc} = 0.5, A_{ee}^{lay} = 0.05, \sigma_{ee}^{lay} = 0.25, A_{ie}^{lay} = 0.01, \sigma_{ie}^{lay} = 0.12, \theta_e = 0.15, \tau = 1.$*

The spatial profiles in the two layers are the same but have either equal or opposite signs. Comparing Tables 2 and 3 identifies the relationship between the eigenfunctions in the dual Amari layers (associated with $\lambda_{\pm}^{\pm}$) and those in the dual E-I layers (associated with $\lambda_n^{\pm}$):

- eigenmodes for $\lambda_1^{\pm}$ and λ_+^+ are *even-symmetric* and the layers have the *same* sign;
- eigenmodes for $\lambda_2^{\pm}$ and λ_+^- are *odd-symmetric* and the layers have the *same* sign;
- eigenmodes for $\lambda_3^{\pm}$ and λ_-^+ are *even-symmetric* and the layers have *opposite* signs;
- eigenmodes for $\lambda_4^{\pm}$ and λ_-^- are *odd-symmetric* and the layers have *opposite* signs.

In what follows, we demonstrate the relationship between the spatial structure of the destabilizing eigenmode and that of the bifurcating solution.

Saddle-node bifurcation of syntopic bumps ($\lambda_1^+ = 0$). Figure 15 shows a bifurcation diagram for a saddle-node bifurcation of a syntopic bump occurring when the interlayer coupling strength A_{ee}^{lay} increases through a critical value. Thus, in the absence of interlayer coupling, each layer alone does not support a stationary bump. The stable syntopic bumps are the smaller bumps on the lower branch of the diagram; in simulations, the upper branch of unstable syntopic bumps acts a separatrix driving solutions outward to the all-excited state.

Hopf bifurcation of the $\lambda_1^{\pm}$ eigenmode to a syntopic breather. When the $\lambda_1^{\pm}$ mode destabilizes in a Hopf bifurcation, it can give rise to a stable *syntopic breather*, i.e., an identical breather in each E-I layer. Hopf bifurcations to stable and unstable breathers were found
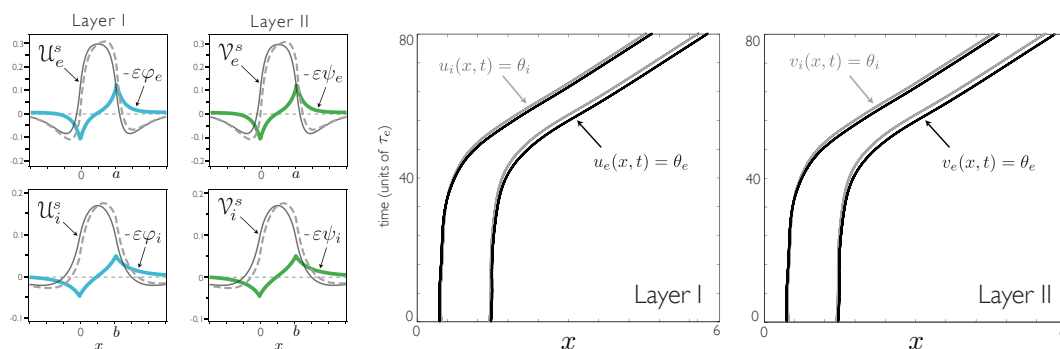
Figure 17. *Destabilization of the syntopic bump with respect to the λ_2^+ eigenmode leading to a traveling syntopic bump. Left: Graph of the eigenfunction for λ_2^+ (colored thick curves), the syntopic bump (solid black curves), and the result of a small perturbation to the syntopic bump (dashed gray curves). Middle and right: Evolution of the activity bumps from a small perturbation of the syntopic bump, with black (gray) lines denoting the E(I) populations. τ is set to $\tau = 4.5$ just beyond the bifurcation point at $\tau^* \approx 4.025$ so that the syntopic bump is unstable. Fixed parameters: $A_{ee}^{loc} = 0.8, A_{ie}^{loc} = A_{ei}^{loc} = A_{ii}^{loc} = 1, \sigma_{ee}^{loc} = 0.2, \sigma_{ie}^{loc} = 0.6, \sigma_{ei}^{loc} = 0.5, \sigma_{ii}^{loc} = 0.8, A_{ee}^{lay} = 0.25, A_{ie}^{lay} = 0.05, \sigma_{ee}^{lay} = 0.4, \sigma_{ie}^{lay} = 0.15, \theta_e = \theta_i = 0.1.*

in many parameter regions. In Figure 16 we generate a bifurcation diagram for a saddle-node bifurcation of syntopic bumps and demonstrate in simulations that a subcritical Hopf bifurcation gives rise to a sharp loss of stability and approach to a stable syntopic breather.

Bifurcation ($\lambda_2^+ = 0$) to a traveling syntopic bump. For the parameters listed in Figure 17, the persistent 0-eigenvalue associated with translation invariance of the bump is given by $\lambda_2^- = 0$. By varying the relative time constant τ, it was possible to destabilize the syntopic bump with respect to the $\lambda_2^+ = 0$ eigenmode and give rise to a constant-speed *traveling syntopic bump* where the solutions in the two layers are identical; however, the bumps in the E and I populations are spatially offset, with E leading I. In Appendix D, we show that one of $\lambda_2^\pm$ always yields the persistent 0-eigenvalue associated with translation invariance of the syntopic bump since $\det \Lambda_2 = 0$. The associated eigenmode is odd-symmetric, and the layers have the same sign, producing identical horizontal translations of the bumps in each layer. (Note that since $\det \Lambda_2 = 0$, eigenvalues $\lambda_2^\pm$ can be redefined as $\lambda_2^+ = \operatorname{tr} \Lambda_2$ and $\lambda_2^- \equiv 0$.)

Pitchfork bifurcation ($\lambda_3^+ = 0$) to a syntopic bump with different widths. Destabilization of the syntopic bump with respect to the λ_3^+ eigenmode can lead to a stable *stationary syntopic bump with different widths* as shown in Figure 18. Numerical simulations at these parameter values suggest the bifurcation is subcritical with a sharp loss of stability and there is a small region of bistability between the two types of syntopic bumps.

Pitchfork bifurcation ($\lambda_4^+ = 0$) to an allotopic bump. Destabilization of the syntopic bump with respect to the λ_4^+ eigenmode can lead to a stable *stationary allotopic bump*, as shown in Figure 19. Note that the bifurcation parameter is σ_{ee}^{lay}, which is analogous to the bifurcation parameter σ_{lay} (section 2.1.2) for the allotopic bump in the pair of Amari neural fields. Numerical simulations suggest the bifurcation is supercritical in this case.

Exotic spatiotemporal behavior. Other complicated patterns of activity were found in the dual E-I neural field model (39)–(40). One example is shown in Figure 20. A stable stationary syntopic bump exists for nearby parameter values. However, as parameters were
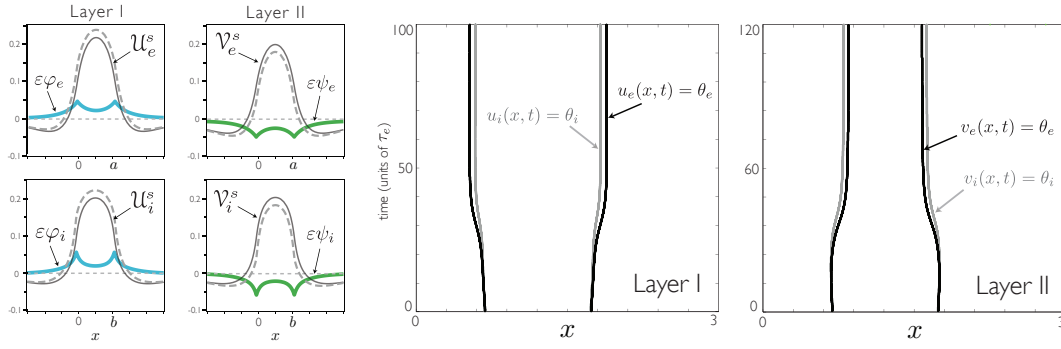
Figure 18. *Destabilization of the syntopic bump with respect to the λ_3^+ eigenmode leading to a* syntopic bump with different widths. *Left: Graph of the eigenfunction for λ_3^+ (colored thick curves), the syntopic bump (solid black curves), and the result of a small perturbation to the syntopic bump (dashed gray curves). Middle and right: Evolution of the activity bumps, from a small perturbation of the syntopic bump. σ_{ee}^{lay} is set to $\sigma_{ee}^{lay} = 0.26$ beyond the bifurcation point, which occurs at $\sigma_{ee}^{lay*} \approx 0.196$, so that the syntopic bump is unstable. Fixed parameters: $A_{ee}^{loc} = A_{ie}^{loc} = A_{ei}^{loc} = A_{ii}^{loc} = 1, \sigma_{ee}^{loc} = 0.5, \sigma_{ie}^{loc} = 0.6, \sigma_{ei}^{loc} = 0.7, \sigma_{ii}^{loc} = 0.8, A_{ee}^{lay} = A_{ie}^{lay} = 0.1, \sigma_{ie}^{lay} = 0.1, \theta_e = \theta_i = 0.1, \tau = 1$.*
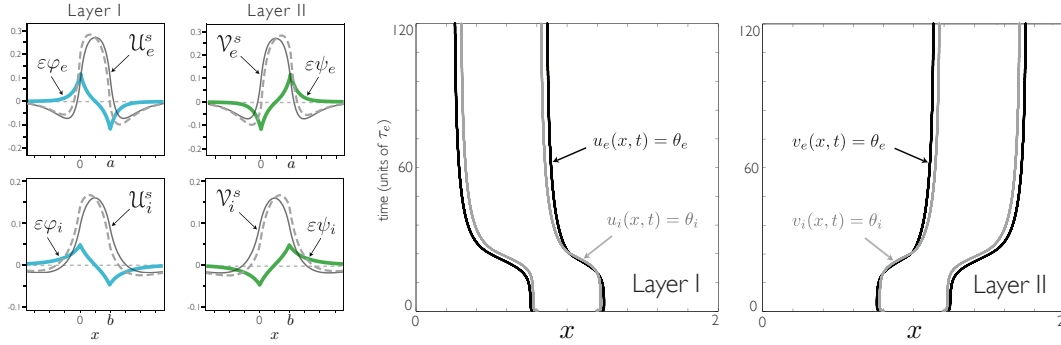

Figure 19. *Destabilization of the syntopic bump with respect to the λ_4^+ eigenmode leading to an* allotopic bump. *Left: Graph of the eigenfunction for λ_4^+ (colored thick curves), the syntopic bump (solid black curves), and result of a small perturbation to the syntopic bump (dashed gray curves). Middle and right: Evolution of the activity bumps from a small perturbation of the syntopic bump. σ_{ee}^{lay} is set to $\sigma_{ee}^{lay} = 3$, significantly beyond the bifurcation point which occurs at $\sigma_{ee}^{lay*} \approx 0.622$. Fixed parameters: $A_{ee}^{loc} = 0.8, \sigma_{ee}^{loc} = 0.2, A_{ie}^{loc} = 1, \sigma_{ie}^{loc} = 0.6, A_{ei}^{loc} = 1, \sigma_{ei}^{loc} = 0.5, A_{ii}^{loc} = 1, \sigma_{ii}^{loc} = 0.8, A_{ee}^{lay} = 0.25, A_{ie}^{lay} = 0.05, \sigma_{ie}^{lay} = 0.15, \theta_e = \theta_i = 0.1, \tau = 1$.*

varied, a dimple formed, puncturing the center of the bump through threshold in the E or I populations, violating the assumptions of a solitary bump in each population.

Nevertheless, condition (45) itself was satisfied, and, by substituting the calculated values of a and b (or using a small perturbation of a and b) into the spatial profile (43)–(44) for a syntopic bump, the result was used as an initial condition to generate the propagating waves in Figure 20, which shows a sequence of transitions in which initial localized activity gives rise to (a) a pair of traveling bumps, (b) a pair of traveling breathers, (c) a pair of traveling breathers shedding activity in their wake that quickly decays to subthreshold values, and (d) a branched propagating wave. The branched wave comes in many forms depending on parameter values and appears to be related to the "back-firing instability" in reaction-diffusion equations and
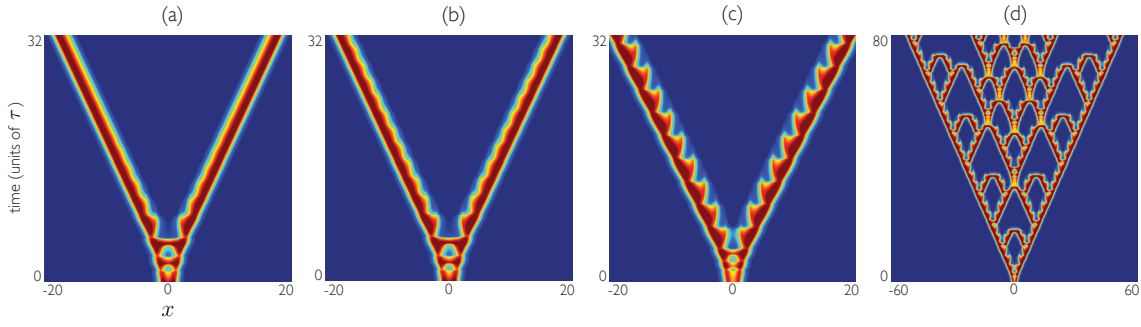
Figure 20. *Simulations of a sequence of transitions from* (a) *a pair of stable syntopic traveling bumps for* $A_{ie}^{lay} = 0.11, \sigma_{ie}^{lay} = 0.08$ *to* (b) *a pair of stable syntopic traveling breathers for* $A_{ie}^{lay} = 0.11, \sigma_{ie}^{lay} = 0.1$ *to* (c) *a pair of syntopic pulsating waves where the backs shed activity that quickly decays to subthreshold values for* $A_{ie}^{lay} = 0.11, \sigma_{ie}^{lay} = 0.3$ *to* (d) *a branched wave formed from the emission of back-propagating pulsating waves for* $A_{ie}^{lay} = 0.1024, \sigma_{ie}^{lay} = 0.3$. *Each panel shows only the E population in a single layer (all populations are similar). Blue represents subthreshold values, yellow represents threshold values* $u_e \approx \theta_e = 0.2$, *and red represents superthreshold values. The profiles* (43)–(44) *with* $(a,b) = (1.07, 0.6)$ *were used for initial data in* (a) *and* (b), *while* $(a,b) = (1.073, 0.7)$ *were used for* (c) *and* (d). *Parameters:* $A_{ee}^{loc} = 1.2, \sigma_{ee}^{loc} = 1, A_{ie}^{loc} = 0.6, \sigma_{ie}^{loc} = 1.2, A_{ei}^{loc} = 1.3, \sigma_{ei}^{loc} = 1, A_{ii}^{loc} = 0.4, \sigma_{ii}^{loc} = 1, A_{ee}^{lay} = 0.1, \sigma_{ee}^{lay} = 0.4, \theta_e = 0.2, \theta_i = 0.25, \tau = 1.$

patterns found on seashells (see [2, 3, 32]) which exhibit elements of the Sierpinski triangle. Branched waves were found previously in a neural field with threshold accommodation [15, 14].

3.3. Stationary bumps in a single E-I layer with long-range excitation. Finally, we briefly mention a novel result for the single E-I neural field layer studied in [7],

$$(51) \qquad \partial_t u_e = -u_e + F_e^{loc}(u_e, u_i), \qquad \tau \partial_t u_i = -u_i + F_i^{loc}(u_e, u_i),$$

where the right-hand sides are given in (39). Note that all of the existence and linear stability analysis in sections 3.1 and 3.2 are valid for the single layer with $w_{ee}^{lay} = w_{ie}^{lay} = 0$, and the matrix equation for the linearization reduces to the two uncoupled matrix subsystems with identical eigenvalues (i.e., $\lambda_1^\pm = \lambda_3^\pm$ and $\lambda_2^\pm = \lambda_4^\pm$ with $w_{ee}^{lay} = w_{ie}^{lay} = 0$).

At the parameter values listed in Figure 21, the single E-I layer (51) supports a stable stationary bump (composed of superthreshold bumps in both E and I populations); moreover, at these parameter values it is the only stationary bump with a superthreshold bump in both the E and I populations. As Figure 21(a) shows, it is possible to have the strength and spatial extent of the local (intralayer) excitatory $e \to e,i$ connections exceed those of the inhibitory $i \to e,i$ connections and still maintain the existence of a stable stationary bump. Using the weight functions in Figure 21(a), we computed the effective weight function in the Amari reduction $w_{loc} = w_{ee}^{loc} - w_{ei}^{loc} * w_{ie}^{loc}$, which is plotted in Figure 21(b). The effective weight function w_{loc} is purely excitatory and not of Mexican hat form. The stationary bump can be approached from a selective set of Gaussian initial data. Most initial conditions follow a short transient and decay to the rest state. For exceedingly large initially excited regions, it was possible to approach the all-excited state. In this way the system acts selectively over small to moderate initial activity bumps either to maintain them as stationary bumps or to extinguish them and return the system to rest.
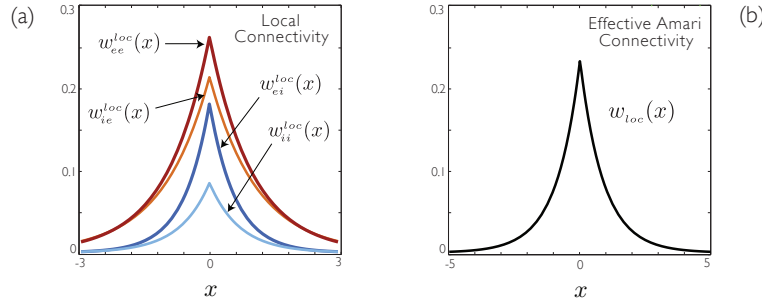
Figure 21. *Nonlateral inhibition regime.* (a) *Plots of the synaptic weight functions for parameters that support a stable stationary bump in a single E-I layer where the spatial extent of the excitatory connections exceed those of the inhibitory connections.* (b) *Plot of the effective local connection in the Amari model in the reduction from the E-I model which is calculated by* $w_{loc} = w_{ee}^{loc} - w_{ei}^{loc} * w_{ie}^{loc}$. *Parameters:* $A_{ee}^{loc} = 0.53, \sigma_{ee}^{loc} = 1, A_{ie}^{loc} = 0.45, \sigma_{ie}^{loc} = 1.1, A_{ei}^{loc} = 0.22, \sigma_{ei}^{loc} = 0.6, A_{ii}^{loc} = 0.12, \sigma_{ii}^{loc} = 0.65, \theta_e = 0.15, \theta_i = 0.15, \tau = 1.$

Another type of unstable bump exists for these parameter values which can guide solutions to the rest state: a superthreshold bump in the E population, with the I population entirely subthreshold. We consider its existence and linear stability and show it is always unstable.

Existence of an excitatory bump. We study the existence of a superthreshold stationary bump in the excitatory population only and refer to it as an *excitatory bump*. We assume the form $(u_e(x,t), u_i(x,t)) = (\mathcal{E}_e(x), \mathcal{E}_i(x))$, where the excitatory population is superthreshold $\mathcal{E}_e(x) > \theta_e$ over $(-a_\varepsilon, a_\varepsilon)$ and subthreshold otherwise, while the inhibitory population is *subthreshold* across the whole domain, i.e., $\mathcal{E}_i(x) < \theta_i$ over $(-\infty, \infty)$. The existence condition for an excitatory bump with halfwidth a_ε is $\mathcal{E}_e(-a_\varepsilon) = \mathcal{E}_e(a_\varepsilon) = \theta_e$, and we have

$$\mathcal{E}_e(x) = \mathcal{W}_{ee}^{loc}(x; a_\varepsilon), \qquad \mathcal{E}_i(x) = \mathcal{W}_{ie}^{loc}(x; a_\varepsilon) < \theta_i.$$

Consequently, the threshold condition determining a_ε is $\mathcal{E}_e(a_\varepsilon) = \mathcal{W}_{ee}^{loc}(2a_\varepsilon; a_\varepsilon) = \theta_e$, guaranteeing existence of the syntopic bump provided all assumptions are satisfied. The condition that $\mathcal{E}_i(x) < \theta_i$ is satisfied in the case of an even-symmetric weight function $w_{ie}^{loc} > 0$ which decays monotonically to 0 for $x > 0$ is determined at the center point $\mathcal{E}_i(0) = 2W_{ie}^{loc}(a_\varepsilon) < \theta_i$. For the parameters in Figure 21, an excitatory bump exists with bump halfwidth $a_\varepsilon \approx 0.417$.

Linear stability of an excitatory bump. The linearization about the excitatory bump $(\mathcal{E}_e(x), \mathcal{E}_i(x))$, by setting $(u_e, u_i)^{\mathrm{T}} = (\mathcal{E}_e, \mathcal{E}_i)^{\mathrm{T}} + (\tilde{\varphi}_e, \tilde{\varphi}_i)^{\mathrm{T}}$, results in the spectral problem

$$\lambda^\varepsilon \varphi_e = -\varphi_e + \mathcal{N}_{ee}^{loc} \varphi_e, \qquad \tau \lambda^\varepsilon \varphi_i = -\varphi_i + \mathcal{N}_{ie}^{loc} \varphi_e$$

for eigenvalues λ^ε and associated eigenfunctions $\phi(x) = (\varphi_e(x), \varphi_i(x))^{\mathrm{T}}$. The essential spectrum is given by $\lambda^\varepsilon = -1$ and is associated with functions φ_e such that $\varphi_e(-a_\varepsilon) = \varphi_e(-a_\varepsilon) = 0$. To calculate the point spectrum, the second equation above determines φ_i in terms of φ_e; then substituting $x = \pm a_\varepsilon$ into the first equation results in the compatibility matrix equation

$$(52) \qquad \begin{bmatrix} -1 + \hat{w}_{ee}^{loc}(0) & \hat{w}_{ee}^{loc}(2a_\varepsilon) \\ \hat{w}_{ee}^{loc}(2a_\varepsilon) & -1 + \hat{w}_{ee}^{loc}(0) \end{bmatrix} \begin{pmatrix} \varphi_e(-a_\varepsilon) \\ \varphi_e(a_\varepsilon) \end{pmatrix} = \lambda^\varepsilon \begin{pmatrix} \varphi_e(-a_\varepsilon) \\ \varphi_e(a_\varepsilon) \end{pmatrix},$$

where $\hat{w}_{ee}^{loc}(x) = \frac{1}{\varepsilon} w_{ee}^{loc}(x)$ and $\varepsilon = |\mathcal{E}_e'(a_\varepsilon)| = w_{ee}^{loc}(0) - w_{ee}^{loc}(2a_\varepsilon)$. The eigenvalues are thus

$$\lambda_\pm^\varepsilon = -1 + \frac{1}{\varepsilon} w_{ee}^{loc}(0) \pm \frac{1}{\varepsilon} w_{ee}^{loc}(2a_\varepsilon).$$

Eigenvalue $\lambda_+^\varepsilon = 2w_{ee}^{loc}(2a)/|\mathcal{E}'_e(a_\varepsilon)| > 0$ since $w_{ee}^{loc}(2a_\varepsilon) > 0$ for any $a_\varepsilon > 0$, and $\lambda_-^\varepsilon \equiv 0$, reflecting the translation invariance of the bump. Thus, any excitatory bump formed by a purely positive weight function w_{ee}^{loc} is always unstable since $\lambda_+^\varepsilon > 0$.

The above analysis naturally extends to the dual E-I neural field model (39)–(40), where there are two cases to study: an excitatory bump in one layer and excitatory bump in both layers. In both cases the inhibitory populations must be subthreshold. We omit the details for brevity but summarize the following: (i) for an excitatory bump in one layer only with all other populations subthreshold, the point spectrum in the linear stability analysis is equivalent to the above analysis for the single layer as all other variables are determined by the superthreshold activity in the single excitatory population; (ii) for an excitatory bump in both layers with the two inhibitory populations subthreshold, the linearization gives rise to a matrix equation of the form (14), where all of the elements of the matrix are positive; i.e., $\hat{w}_{loc}(x), \hat{w}_{lay}(x) > 0$. The eigenvalues are then given by (15), and it follows that the bump is linearly unstable since the equivalent eigenvalue $\lambda_+^+ > 0$ for any bump halfwidth a since $\hat{w}_{loc}(x), \hat{w}_{lay}(x) > 0$.

Finally, another stationary bump that can be considered is composed of an E-I bump in one layer and an excitatory bump in the other layer, requiring three halfwidths $(a_{\mathsf{I}}, b_{\mathsf{I}}, a_{\mathsf{II}})$.

4. Discussion. In this paper, we have extended both an E-I neural field and the Amari neural field models to an interacting pair of neural fields and studied the existence, linear stability, and bifurcations of a variety of the stationary bumps supported by these models. In the context of location in the brain, the interacting pair of neural fields could represent two interacting brain regions, two interacting layers of tissue within the same brain region, or even two distinct pools of neurons that interact within the same layer of neural tissue. Although the coupling between the two neural fields in general could be quite diverse, we assumed that the interlayer connections were "reciprocally symmetric," which was used to imply the the connections were identical from one layer to the other and vice versa, and, in one particular case, we introduced an asymmetry in the interlayer coupling by allowing the strength and spatial extent of connections to be different from one layer to the other. However, in both cases, the translationally invariant interlayer connections implicitly still obey the property that the center points of the even-symmetric weight functions for each of the two layers are "reciprocally connected"; i.e., a center point x_{I} in the even-symmetric connections from Layer I which project to a point x_{II} in Layer II is the same point in Layer I that receives connections from Layer II that are centered (even-symmetric) about the point x_{II}. A lateral shift in this topology from one layer to the other would induce a qualitatively different type of asymmetry, and such a shift was shown to induce traveling waves in [45].

A universal coordinate system was defined for the two layers based on the reciprocal connections and led to the definitions of *syntopic* and *allotopic* bumps for distinguishing bumps that are centered about the same or different points in the universal coordinate system. It was also possible for a syntopic bump to have the same or different widths in the two layers when the local connections in the layers were identical and the interlayer connections between the layers were identical. An important extension of stationary bumps that we considered was the ability of the interacting layers to support a syntopic bump when each layer in isolation does not support a bump, a scenario we have previously proposed [24] as a plausible explanation for the occurrence of persistent activity exhibited during working memory tasks but the lack

of activity bumps exhibited in slices in vitro. In the dual Amari and the dual E-I neural fields, the linearization about the syntopic bump with equal widths in each case gave rise to a set of eigenfunctions that were shown to be related through spatial structure. The solutions arising from destabilizing these eigenmodes exhibited spatial structure directly related to that of the eigenfunctions. All components of the eigenfunctions were either even or odd in both layers with equal or opposite signs across the two layers. Bifurcations with respect to an even eigenmode with opposite signs gave rise to a syntopic bump with different widths, whereas bifurcations with respect to an odd eigenmode with opposite signs gave rise to an allotopic bump. Interestingly, numerical simulations of reciprocally asymmetric interlayer coupling in the dual Amari neural field show that destabilizing the odd eigenmode with opposite signs can give rise to a traveling allotopic bump. Existence and linear stability was also carried out for the allotopic bump and the syntopic bump with different widths in the dual Amari neural field. Finally, in the single layer E-I model, we demonstrated that stationary bumps can be stabilized in a nonlateral inhibition regime and, in both the single and dual layer E-I models, it is possible to have superthreshold stationary bumps in the excitatory population only.

In a number of directions one could extend this work on one-dimensional domains. Multibump solutions could be studied along the lines of [36]. Synaptic delays could naturally be introduced [31], and the stability and bifurcations of both the homogeneous state and stationary bumps could be studied to see what new types of patterns may arise. The existence and stability of the traveling allotopic bump in the dual Amari neural field with reciprocally asymmetric interlayer coupling would also be interesting to study. And one could similarly study the existence and stability of traveling fronts and pulses in the dual E-I neural field. Given the ubiquity of reciprocally connected regions in the brain, there is a myriad of applications to specific neural phenomena that could be modeled by interacting neural fields with different types of local and interlayer coupling, and numerical simulations can be used when the model is no longer analytically tractable. Finally, an important step is to extend these results to two-dimensional spatial domains [23, 22, 37] to study synaptic interactions between interconnected layers of neural tissue that can be approximated as two-dimensional.

Appendix A. Structure of the matrix $\left(\mathrm{M}_s - \mathrm{I}_4\right)$ for the syntopic bump. Using the following similarity transformation, $\left(\mathrm{M}_s - \mathrm{I}_4\right)$ is similar to the block diagonal matrix Λ_s:

$$(53) \qquad \mathrm{Q}^{-1}\left(\mathrm{M}_s - \mathrm{I}_4\right)\mathrm{Q} = \Lambda_s \equiv \begin{bmatrix} \Lambda_+ & 0 \\ 0 & \Lambda_- \end{bmatrix},$$

$$\left(\mathrm{M}_s - \mathrm{I}_4\right) = \begin{bmatrix} A & B & C & D \\ B & A & D & C \\ C & D & B & A \\ D & C & A & B \end{bmatrix}, \qquad \begin{aligned} \Lambda_+ &= \begin{bmatrix} A+B & C+D \\ C+D & A+B \end{bmatrix}, \\ \Lambda_- &= \begin{bmatrix} A-B & C-D \\ C-D & A-B \end{bmatrix}, \end{aligned} \qquad \mathrm{Q} = \begin{bmatrix} 1 & 0 & 1 & 0 \\ 1 & 0 & -1 & 0 \\ 0 & 1 & 0 & 1 \\ 0 & 1 & 0 & -1 \end{bmatrix}.$$

Setting $\det\Lambda_+ = 0$ results in eigenvalues $\lambda_\pm^+$ and eigenvectors $\boldsymbol{y}_\pm^+$ of Λ_s, where

$$\lambda_\pm^+ = (\mathrm{A}+\mathrm{B}) \pm (\mathrm{C}+\mathrm{D}), \qquad \boldsymbol{y}_\pm^+ = (1, \pm 1, 0, 0)^{\mathrm{T}}.$$

Setting $\det\Lambda_- = 0$ results in eigenvalues $\lambda_\pm^-$ and eigenvectors $\boldsymbol{y}_\pm^-$ of Λ_s, where

$$\lambda_\pm^- = (\mathrm{A}-\mathrm{B}) \pm (\mathrm{C}-\mathrm{D}), \qquad \boldsymbol{y}_\pm^- = (0, 0, 1, \pm 1)^{\mathrm{T}}.$$

Table 2

Eigenfunctions for the linearization about the syntopic bump in the interacting pair of Amari neural fields discussed in section 2.1.1. The components of the eigenfunctions for $\lambda_\pm^+$ are even in both layers, but for λ_+^+ the components in the two layers have the same sign, whereas for λ_-^+ the components have the opposite sign. The components of the eigenfunctions for $\lambda_\pm^-$ are odd in both layers, but for λ_+^- the components in the two layers have the same sign, whereas for λ_-^- the components have the opposite sign.

Dual Amari—eigenfunctions for the linearization about the syntopic bump			
λ	$\begin{pmatrix}\varphi(x)\\\psi(x)\end{pmatrix}$ = expression in terms of $\Omega_\pm^{loc}, \Omega_\pm^{lay}$	$\boldsymbol{y}$	$\boldsymbol{v} = \mathrm{Q}\boldsymbol{y}$
λ_+^+	$\begin{pmatrix}\Phi_+^+(x)\\\Psi_+^+(x)\end{pmatrix} = \dfrac{1}{(1+\lambda_+^+)}\begin{pmatrix}\Omega_+^{loc}(x) + \Omega_+^{lay}(x)\\\Omega_+^{loc}(x) + \Omega_+^{lay}(x)\end{pmatrix}$	$\boldsymbol{y}_+^+ = (1,1,0,0)^{\mathrm{T}}$	$\boldsymbol{v}_+^+ = (1,1,1,1)^{\mathrm{T}}$
λ_-^+	$\begin{pmatrix}\Phi_-^+(x)\\\Psi_-^+(x)\end{pmatrix} = \dfrac{1}{(1+\lambda_-^+)}\begin{pmatrix}\Omega_+^{loc}(x) - \Omega_+^{lay}(x)\\-\Omega_+^{loc}(x) + \Omega_+^{lay}(x)\end{pmatrix}$	$\boldsymbol{y}_-^+ = (1,-1,0,0)^{\mathrm{T}}$	$\boldsymbol{v}_-^+ = (1,1,-1,-1)^{\mathrm{T}}$
λ_+^-	$\begin{pmatrix}\Phi_+^-(x)\\\Psi_+^-(x)\end{pmatrix} = \dfrac{1}{(1+\lambda_+^-)}\begin{pmatrix}\Omega_-^{loc}(x) + \Omega_-^{lay}(x)\\\Omega_-^{loc}(x) + \Omega_-^{lay}(x)\end{pmatrix}$	$\boldsymbol{y}_+^- = (0,0,1,1)^{\mathrm{T}}$	$\boldsymbol{v}_+^- = (1,-1,1,-1)^{\mathrm{T}}$
λ_-^-	$\begin{pmatrix}\Phi_-^-(x)\\\Psi_-^-(x)\end{pmatrix} = \dfrac{1}{(1+\lambda_-^-)}\begin{pmatrix}\Omega_-^{loc}(x) - \Omega_-^{lay}(x)\\-\Omega_-^{loc}(x) + \Omega_-^{lay}(x)\end{pmatrix}$	$\boldsymbol{y}_-^- = (0,0,1,-1)^{\mathrm{T}}$	$\boldsymbol{v}_-^- = (1,-1,-1,1)^{\mathrm{T}}$

The eigenvectors $\boldsymbol{v}_\pm^\pm = (\varphi(0), \varphi(a), \psi(0), \psi(a))^{\mathrm{T}}$ of $(\mathrm{M}_s - \mathrm{I}_4)$ are calculated from $\boldsymbol{v}_\pm^\pm = \mathrm{Q}\boldsymbol{y}_\pm^\pm$. This determines the values of $\varphi(0), \varphi(a), \psi(0), \psi(a)$ in the expression

$$\begin{pmatrix}\varphi(x)\\\psi(x)\end{pmatrix} = \frac{1}{(1+\lambda)}\left[\begin{pmatrix}\hat{w}_{loc}(x)\varphi(0) + \hat{w}_{loc}(x-a)\varphi(a)\\\hat{w}_{loc}(x)\psi(0) + \hat{w}_{loc}(x-a)\psi(a)\end{pmatrix} + \begin{pmatrix}\hat{w}_{lay}(x)\psi(0) + \hat{w}_{lay}(x-a)\psi(a)\\\hat{w}_{lay}(x)\varphi(0) + \hat{w}_{lay}(x-a)\varphi(a)\end{pmatrix}\right]$$

for the *eigenfunction* $(\varphi(x), \psi(x))^{\mathrm{T}}$ in section 2.1.1. The four cases $(\lambda_\pm^\pm, \boldsymbol{v}_\pm^\pm)$ produce four associated eigenfunctions $(\Phi_\pm^\pm(x), \Psi_\pm^\pm(x))^{\mathrm{T}}$ which are listed in Table 2. The eigenfunctions are expressed in terms of *even* components $\Omega_+^l(x)$ and *odd* components $\Omega_-^l(x)$,

$$\Omega_\pm^{loc}(x) = \hat{w}_{loc}(x) \pm \hat{w}_{loc}(x-a), \qquad \Omega_\pm^{lay}(x) = \hat{w}_{lay}(x) \pm \hat{w}_{lay}(x-a),$$

and $\hat{w}_l(x) = w_l(x)/|\mathcal{U}_s'(0)|$ for $l \in \{loc, lay\}$ since the weight functions w_l have even-symmetry. Consequently each eigenfunction has characteristic spatial structure (see Figures 5 and 7, for example), which plays a role in bifurcations in which the loss of stability is associated with that particular mode. Associated with the 0-eigenvalue $\lambda_+^- \equiv 0$, the spatial structure of eigenfunction $(\Phi_+^-, \Psi_+^-)^{\mathrm{T}}$ is an odd-symmetric lateral perturbation, oriented in the same direction in each layer, and corresponds to the translation mode of the system.

Eigenfunctions for the syntopic periodic bump. Note that the expressions listed in Table 2 are valid for the syntopic *periodic* bump in section 2.2.1 with $\hat{w}_l$ replaced by $\hat{w}_l^{per}$ for $l \in \{loc, lay\}$, $\mathcal{U}(a)$ replaced by $\mathcal{P}(a)$, and a calculated instead from (33).

Appendix B. Structure of the matrix $(\mathrm{M}_o - \mathrm{I}_4)$ for the allotopic bump. By the following similarity transformation, $(\mathrm{M}_o - \mathrm{I}_4)$ in section 2.1.2 is similar to the block diagonal matrix Λ_o:

$$(54) \qquad \mathrm{Q}_o^{-1}(\mathrm{M}_o - \mathrm{I}_4)\mathrm{Q}_o = \Lambda_o = \begin{bmatrix} \Lambda_+ & 0 \\ 0 & \Lambda_- \end{bmatrix},$$

$$(\mathrm{M}_o - \mathrm{I}_4) = \begin{bmatrix} A & B & H & G \\ C & D & F & E \\ E & F & D & C \\ G & H & B & A \end{bmatrix}, \qquad \mathrm{Q}_o = \begin{bmatrix} 1 & 0 & 1 & 0 \\ 0 & 1 & 0 & 1 \\ 0 & 1 & 0 & -1 \\ 1 & 0 & -1 & 0 \end{bmatrix}, \qquad \begin{aligned} \Lambda_+ &= \begin{bmatrix} A{+}G & B{+}H \\ C{+}E & D{+}F \end{bmatrix}, \\[6pt] \Lambda_- &= \begin{bmatrix} A{-}G & B{-}H \\ C{-}E & D{-}F \end{bmatrix}. \end{aligned}$$

Case: $\det(\Lambda_+ - \lambda \mathrm{I}) = 0$. Eigenvalues $\lambda_\pm^+$ and eigenvectors $\boldsymbol{y}_\pm^+ = (m_\pm^+, 1, 0, 0)^{\mathrm{T}}$ of Λ_o,

$$\lambda_\pm^+ = \tfrac{1}{2}\big[(A + G) + (D + F)\big] \pm \tfrac{1}{2}\sqrt{\big[(A + G) - (D + F)\big]^2 + 4\big[(B + H)(C + E)\big]},$$

which transform to eigenvectors $\boldsymbol{v}_\pm^+$ of $(\mathrm{M}_o - \mathrm{I}_4)$ given by $\boldsymbol{v}_\pm^- = \mathrm{Q}_o \boldsymbol{y}_\pm^+ = (m_\pm^+, 1, 1, m_\pm^+)^{\mathrm{T}}$.

Case: $\det(\Lambda_- - \lambda \mathrm{I}) = 0$. Eigenvalues $\lambda_\pm^-$ and eigenvectors $\boldsymbol{y}_\pm^- = (0, 0, m_\pm^-, 1)^{\mathrm{T}}$ of Λ_o,

$$\lambda_\pm^- = \tfrac{1}{2}\big[(A - G) + (D - F)\big] \pm \tfrac{1}{2}\sqrt{\big[(A - G) - (D - F)\big]^2 + 4\big[(B - H)(C - E)\big]},$$

which transform to eigenvectors $\boldsymbol{v}_\pm^-$ of $(\mathrm{M}_o - \mathrm{I}_4)$ given by $\boldsymbol{v}_\pm^- = \mathrm{Q}_o \boldsymbol{y}_\pm^- = (m_\pm^-, 1, -1, -m_\pm^-)^{\mathrm{T}}$. Eigenfunctions may be subsequently calculated along the lines developed in Appendix A. Note that when $\det \Lambda_- = 0$, eigenvalues $\lambda_\pm^-$ can be redefined as $\lambda_+^- \equiv 0$ and $\lambda_-^- = \mathsf{tr}\,\Lambda_-$.

Appendix C. Structure of the matrix $(\mathrm{M}_{\mathrm{asym}} - \mathrm{I}_4)$ for asymmetric interlayer coupling. Matrix $(\mathrm{M}_{\mathrm{asym}} - \mathrm{I}_4)$ in section 2.1.2 is similar to the block diagonal matrix Λ_{asym} according to

$$(55) \qquad \mathrm{Q}^{-1}(\mathrm{M}_{\mathrm{asym}} - \mathrm{I}_4)\mathrm{Q} = \Lambda_{\mathrm{asym}} = \begin{bmatrix} \Lambda_+ & 0 \\ 0 & \Lambda_- \end{bmatrix},$$

$$(\mathrm{M}_{\mathrm{asym}} - \mathrm{I}_4) = \begin{bmatrix} A & B & C & D \\ B & A & D & C \\ E & F & G & H \\ F & E & H & G \end{bmatrix}, \qquad \mathrm{Q} = \begin{bmatrix} 1 & 0 & 1 & 0 \\ 1 & 0 & -1 & 0 \\ 0 & 1 & 0 & 1 \\ 0 & 1 & 0 & -1 \end{bmatrix}, \qquad \begin{aligned} \Lambda_+ &= \begin{bmatrix} A{+}B & C{+}D \\ E{+}F & G{+}H \end{bmatrix}, \\[6pt] \Lambda_- &= \begin{bmatrix} A{-}B & C{-}D \\ E{-}F & G{-}H \end{bmatrix}. \end{aligned}$$

Case: $\det(\Lambda_+ - \lambda \mathrm{I}) = 0$. Eigenvalues $\lambda_\pm^+$ and eigenvectors $\boldsymbol{y}_\pm^- = (m_\pm^+, 1, 0, 0)^{\mathrm{T}}$ of Λ_{asym},

$$\lambda_\pm^+ = \tfrac{1}{2}\big[(A + B) + (G + H)\big] \pm \tfrac{1}{2}\sqrt{\big[(A + B) - (G + H)\big]^2 + 4\big[(C + D)(E + F)\big]},$$

which transform to eigenvectors $\boldsymbol{v}_\pm^+$ of $(\mathrm{M}_{\mathrm{asym}} - \mathrm{I}_4)$ given by $\boldsymbol{v}_\pm^- = \mathrm{Q}\boldsymbol{y}_\pm^+ = (m_\pm^+, m_\pm^+, 1, 1)^{\mathrm{T}}$.

Case: $\det(\Lambda_- - \lambda \mathrm{I}) = 0$. Eigenvalues $\lambda_\pm^-$ and eigenvectors $\boldsymbol{y}_\pm^- = (0, 0, m_\pm^-, 1)^{\mathrm{T}}$ of Λ_{asym},

$$\lambda_\pm^- = \tfrac{1}{2}\big[(A - B) + (G - H)\big] \pm \tfrac{1}{2}\sqrt{\big[(A - B) - (G - H)\big]^2 + 4\big[(C - D)(E - F)\big]},$$

which transform to eigenvectors $\boldsymbol{v}_\pm^-$ of $(\mathrm{M}_{\mathrm{asym}} - \mathrm{I}_4)$ given by $\boldsymbol{v}_\pm^- = \mathrm{Q}\boldsymbol{y}_\pm^- = (m_\pm^-, -m_\pm^-, 1, -1)^{\mathrm{T}}$. Eigenfunctions may be subsequently calculated along the lines developed in Appendix A.

Appendix D. Structure of the matrix operator $(\mathbf{M_{EI}} - \mathbf{I_{EI}})$. Two sequential similarity transforms reduce the $8{\times}8$ matrix $(\mathrm{M_{EI}} - \mathrm{I_{EI}})$ to a block diagonal matrix Λ_{EI} for calculating eigenvalues and eigenvectors, the elements of which determine the eigenfunctions (46)–(48):

$$
(\mathrm{M_{EI}} - \mathrm{I_{EI}}) =
\begin{bmatrix}
A & B & C & D & K & L & 0 & 0 \\
B & A & D & C & L & K & 0 & 0 \\
E & F & G & H & M & N & 0 & 0 \\
F & E & H & G & N & M & 0 & 0 \\
K & L & 0 & 0 & A & B & C & D \\
L & K & 0 & 0 & B & A & D & C \\
M & N & 0 & 0 & E & F & G & H \\
N & M & 0 & 0 & F & E & H & G
\end{bmatrix}.
$$

The similarity transform $\mathrm{Q}_1^{-1}\mathrm{M_{EI}}\mathrm{Q}_1 = \Pi_{\mathrm{EI}}$, with I_4 denoting the $4{\times}4$ identity matrix, shows that $\mathrm{M_{EI}}$ is similar to Π_{EI}, where

$$
\Pi_{\mathrm{EI}} =
\begin{bmatrix}
\Pi_+ & 0 \\
0 & \Pi_-
\end{bmatrix},
\qquad
\Pi_{\pm} =
\begin{bmatrix}
A \pm K & B \pm L & C & D \\
B \pm L & A \pm K & D & C \\
E \pm M & F \pm N & G & H \\
F \pm N & E \pm M & H & G
\end{bmatrix},
\qquad
\mathrm{Q}_1 =
\begin{bmatrix}
\mathrm{I}_4 & \mathrm{I}_4 \\
\mathrm{I}_4 & -\mathrm{I}_4
\end{bmatrix}.
$$

Define the invertible $8{\times}8$ matrix Q_2 below, which is based on Q and Q^{-1} defined in (53). The similarity transform $\mathrm{Q}_2^{-1}\,\Pi_{\mathrm{EI}}\,\mathrm{Q}_2 = \Lambda_{\mathrm{EI}}$ subsequently shows that Π_{EI} is similar to Λ_{EI}, where

$$
\Lambda_{\mathrm{EI}} = \mathsf{diag}(\Lambda_1, \Lambda_2, \Lambda_3, \Lambda_4),
\qquad
\mathrm{Q}_2 =
\begin{bmatrix}
\mathrm{Q} & 0 \\
0 & \mathrm{Q}
\end{bmatrix},
$$

and the four $2{\times}2$ submatrices Λ_n, $n = 1, \dots, 4$, are given by

$$
\Lambda_1 =
\begin{bmatrix}
(A + B) + (K + L) & (C + D) \\
(E + F) + (M + N) & (G + H)
\end{bmatrix},
\qquad
\Lambda_3 =
\begin{bmatrix}
(A + B) - (K + L) & (C + D) \\
(E + F) - (M + N) & (G + H)
\end{bmatrix},
$$

$$
\Lambda_2 =
\begin{bmatrix}
(A - B) + (K - L) & (C - D) \\
(E - F) + (M - N) & (G - H)
\end{bmatrix},
\qquad
\Lambda_4 =
\begin{bmatrix}
(A - B) - (K - L) & (C - D) \\
(E - F) - (M - N) & (G - H)
\end{bmatrix}.
$$

Since $(\mathrm{M_{EI}} - \mathrm{I_{EI}})$ is similar to Π_{EI}, which is similar to Λ_{EI}, all have the same eight eigenvalues given by the four $2{\times}2$ submatrices Λ_n for $n = 1, \dots, 4$, which can be calculated according to

$$
\lambda_n^{\pm} = \tfrac{1}{2}\,\mathsf{tr}\,\Lambda_n \pm \tfrac{1}{2}\sqrt{\left(\mathsf{tr}\,\Lambda_n\right)^2 - 4\,\mathsf{det}\,\Lambda_n}.
$$

The eight eigenvalues were calculated and are listed in section 3.2. The associated eight eigenfunctions $\boldsymbol{\phi} = (\varphi_e, \varphi_i, \psi_e, \psi_i)$ are calculated from (46)–(49) and are listed compactly as four pairs of eigenfunctions in Table 3 with the pair indicated by $\pm$.

Table 3

Eigenfunctions for the linearization about the syntopic bump in the interacting pair of E-I neural fields (39) *in section* 3. *The spatial structure is determined by* $\mathbb{M}$ *and* $\mathbb{N}$ *which are even and odd functions, respectively.*

	Dual E-I—eigenfunctions for the linearization about the syntopic bump		
$\lambda^{\pm}$	$\begin{pmatrix}\Phi_n^{\pm}\\\Psi_n^{\pm}\end{pmatrix} \equiv \boldsymbol{\phi}_n^{\pm}(x) = (\varphi_e(x), \varphi_i(x), \psi_e(x), \psi_i(x))^{\mathrm{T}}$		$\boldsymbol{y}$ $\boldsymbol{v} = \mathrm{Q}\boldsymbol{y}$
$\lambda_1^{\pm}$	$\begin{pmatrix}\Phi_1^{\pm}\\\Psi_1^{\pm}\end{pmatrix} = \frac{1}{(1+\lambda_1^{\pm})}\begin{pmatrix} +\mathbb{M}_e^{loc}(x) - \mathbb{M}_i^{loc}(x) + \mathbb{M}_e^{lay}(x) \\ +\mathbb{M}_e^{loc}(x) - \mathbb{M}_i^{loc}(x) + \mathbb{M}_e^{lay}(x) \end{pmatrix}$		$\boldsymbol{y}_1^{\pm} = (\mathrm{v}_1^{\pm}, 1, 0, 0, 0, 0, 0, 0)^{\mathrm{T}}$ $\boldsymbol{v}_1^{\pm} = (\mathrm{v}_1^{\pm}, \mathrm{v}_1^{\pm}, 1, 1, \mathrm{v}_1^{\pm}, \mathrm{v}_1^{\pm}, 1, 1)^{\mathrm{T}}$
$\lambda_2^{\pm}$	$\begin{pmatrix}\Phi_2^{\pm}\\\Psi_2^{\pm}\end{pmatrix} = \frac{1}{(1+\lambda_2^{\pm})}\begin{pmatrix} +\mathbb{N}_e^{loc}(x) - \mathbb{N}_i^{loc}(x) + \mathbb{N}_e^{lay}(x) \\ +\mathbb{N}_e^{loc}(x) - \mathbb{N}_i^{loc}(x) + \mathbb{N}_e^{lay}(x) \end{pmatrix}$		$\boldsymbol{y}_2^{\pm} = (0, 0, \mathrm{v}_2^{\pm}, 1, 0, 0, 0, 0)^{\mathrm{T}}$ $\boldsymbol{v}_2^{\pm} = (\mathrm{v}_2^{\pm}, -\mathrm{v}_2^{\pm}, 1, -1, \mathrm{v}_2^{\pm}, -\mathrm{v}_2^{\pm}, 1, -1)^{\mathrm{T}}$
$\lambda_3^{\pm}$	$\begin{pmatrix}\Phi_3^{\pm}\\\Psi_3^{\pm}\end{pmatrix} = \frac{1}{(1+\lambda_3^{\pm})}\begin{pmatrix} +\mathbb{M}_e^{loc}(x) - \mathbb{M}_i^{loc}(x) + \mathbb{M}_e^{lay}(x) \\ -\mathbb{M}_e^{loc}(x) + \mathbb{M}_i^{loc}(x) - \mathbb{M}_e^{lay}(x) \end{pmatrix}$		$\boldsymbol{y}_3^{\pm} = (0, 0, 0, 0, \mathrm{v}_3^{\pm}, 1, 0, 0)^{\mathrm{T}}$ $\boldsymbol{v}_3^{\pm} = (\mathrm{v}_3^{\pm}, \mathrm{v}_3^{\pm}, 1, 1, -\mathrm{v}_3^{\pm}, -\mathrm{v}_3^{\pm}, -1, -1)^{\mathrm{T}}$
$\lambda_4^{\pm}$	$\begin{pmatrix}\Phi_4^{\pm}\\\Psi_4^{\pm}\end{pmatrix} = \frac{1}{(1+\lambda_4^{\pm})}\begin{pmatrix} +\mathbb{N}_e^{loc}(x) - \mathbb{N}_i^{loc}(x) + \mathbb{N}_e^{lay}(x) \\ -\mathbb{N}_e^{loc}(x) + \mathbb{N}_i^{loc}(x) - \mathbb{N}_e^{lay}(x) \end{pmatrix}$		$\boldsymbol{y}_4^{\pm} = (0, 0, 0, 0, 0, 0, \mathrm{v}_4^{\pm}, 1)^{\mathrm{T}}$ $\boldsymbol{v}_4^{\pm} = (\mathrm{v}_4^{\pm}, -\mathrm{v}_4^{\pm}, 1, -1, -\mathrm{v}_4^{\pm}, \mathrm{v}_4^{\pm}, -1, 1)^{\mathrm{T}}$

To express the eigenfunction $\boldsymbol{\phi}_n$ (four-dimensional vector) in a compact form highlighting its structure, we express $\boldsymbol{\phi}_n$ in terms of 2-vectors Φ and Ψ for each E-I layer as follows:

$$\boldsymbol{\phi}(x) = (\varphi_e(x), \varphi_i(x), \psi_e(x), \psi_i(x))^{\mathrm{T}} \equiv \begin{pmatrix}\Phi(x)\\\Psi(x)\end{pmatrix} \implies \Phi(x) = \begin{pmatrix}\varphi_e\\\varphi_i\end{pmatrix}, \; \Psi(x) = \begin{pmatrix}\psi_e\\\psi_i\end{pmatrix}.$$

For $n = 1, \ldots, 4$, eigenvectors $\boldsymbol{v}_n^{\pm} = (\varphi_e(-a), \varphi_e(a), \varphi_i(-b), \varphi_i(b), \psi_e(-a), \psi_e(a), \psi_i(-b), \psi_i(b))^{\mathrm{T}}$ of $(\mathrm{M_{EI}} - \mathrm{I_8})$ can be calculated from the eigenvectors $\boldsymbol{y}_n^{\pm}$ of Λ_{EI} according to $\boldsymbol{v}_{\pm} = \mathrm{Q}\boldsymbol{y}_n^{\pm}$. The values of $\boldsymbol{v}_n^{\pm}$ can then be substituted into (46)–(49) to determine the corresponding eigenfunction $\boldsymbol{\phi}_n(x) = (\varphi_e(x), \varphi_i(x), \psi_e(x), \psi_i(x))^{\mathrm{T}}$. Next, we define the following 2-vectors for $l \in \{loc, lay\}$ and $u \in \{e, i\}$ with $\alpha_e = a$ and $\alpha_i = b$:

$$\mathbb{M}_u^l(x) = \eta_u^{\pm}\begin{pmatrix} \hat{w}_{eu}^l(x+\alpha_u) + \hat{w}_{eu}^l(x-\alpha_u) \\ \hat{w}_{iu}^l(x+\alpha_u) + \hat{w}_{iu}^l(x-\alpha_u) \end{pmatrix}, \qquad \mathbb{N}_u^l(x) = \eta_u^{\pm}\begin{pmatrix} \hat{w}_{eu}^l(x+\alpha_u) - \hat{w}_{eu}^l(x-\alpha_u) \\ \hat{w}_{iu}^l(x+\alpha_u) - \hat{w}_{iu}^l(x-\alpha_u) \end{pmatrix},$$

where $\mathbb{M}_u^l(x)$ is *even-symmetric* in x and $\mathbb{N}_u^l(x)$ is *odd-symmetric* in x (since w_{uv}^l are even). Coefficient $\eta_u^{\pm}$ for $u \in \{e, i\}$ depends upon the index n of the submatrix Λ_n under consideration. For $n = 1, \ldots, 4$, the values of $(\eta_e^{\pm}, \eta_i^{\pm}) = (\mathrm{v}_n^{\pm}, 1)$, where $(\mathrm{v}_n^{\pm}, 1)^{\mathrm{T}}$ represents the two eigenvectors of submatrix Λ_n. All eight eigenfunctions are listed as four pairs $\boldsymbol{\phi}_n^{\pm}(x)$ in Table 3 along with the associated eigenvectors $\boldsymbol{y}_n^{\pm}$ and $\boldsymbol{v}_n^{\pm}$. Note that the spatial structure of the eigenfunctions is reflected in the shapes used in the symbols $\mathbb{M}$ and $\mathbb{N}$ (see Figures 5, 7, 19, 17, and 18).

0-eigenvalue associated with translation invariance. We now show that, depending on the sign of $\mathrm{tr}\,\Lambda_2$, one of the eigenvalues $\lambda_2^{\pm}$ generates the persistent 0-eigenvalue related to translation invariance of the bump. It is sufficient to show $\det \Lambda_2 \equiv 0$. To see this, define

$$m_{uv}^l(\alpha, \beta) = w_{uv}^l(\alpha - \beta) - w_{uv}^l(\alpha + \beta),$$

where $u, v \in \{e, i\}$ and $l \in \{loc, lay\}$ and express the gradients γ_e, γ_i in (50) as

$$\gamma_e = m_{ee}^{loc}(a, a) - m_{ei}^{loc}(a, b) + m_{ee}^{lay}(a, a),$$
$$\gamma_i = m_{ie}^{loc}(b, a) - m_{ii}^{loc}(b, b) + m_{ie}^{lay}(b, a).$$

Using these expressions for γ_e, γ_i, the following quantities present in $\det \Lambda_2$ simplify as follows:

$$\mathrm{D}_1 = \left[-1 + \tfrac{1}{\gamma_e}\big(m_{ee}^{loc}(a, a) + m_{ee}^{lay}(a, a)\big)\right] = \tfrac{1}{\gamma_e} m_{ei}^{loc}(a, b),$$

$$\mathrm{D}_2 = \left[-\tfrac{1}{\tau} + \tfrac{1}{\tau\gamma_i}\big(- m_{ii}^{loc}(b, b)\big)\right] = \tfrac{1}{\tau\gamma_i}\big(- m_{ie}^{loc}(b, a) - m_{ie}^{lay}(a, b)\big).$$

Thus we can express $\det \Lambda_2 = \mathrm{D}_1\mathrm{D}_2 - \mathrm{D}_3$, where

$$\mathrm{D}_3 = \tfrac{1}{\tau\gamma_e\gamma_i}\big(m_{ie}^{loc}(b, a) + m_{ie}^{lay}(a, b)\big)\big(- m_{ei}^{loc}(a, b)\big) \quad \Longrightarrow \quad \det \Lambda_2 \equiv \mathrm{D}_1\mathrm{D}_2 - \mathrm{D}_3 = 0.$$

Since $\det \Lambda_2 = 0$, the eigenvalues $\lambda_2^\pm$ can be redefined simply as $\lambda_2^+ = \operatorname{tr}\Lambda_2$ and $\lambda_2^- \equiv 0$; the eigenfunctions $\phi_2^\pm$ must then be modified accordingly.

Appendix E. Remarks on numerical simulations. Simulations were computed using either an Euler or improved Euler scheme for the temporal dynamics with the spatial integral computed using the antiderivative $W(x)$, where

$$(56) \qquad \int_{-\infty}^{\infty} w(x - y)H\big(u(y, t_n) - \theta\big)dy = W(x - a_n) - W(x - b_n)$$

and a_n and b_n track the left and right endpoints of the bump of activity at $t = t_n$. On each iteration n, points a_n and b_n are determined using linear interpolation to approximate the precise threshold crossings x^* where $u(x^*, t_n) = \theta$ based upon the two neighboring gridpoints. Although this scheme is limited to the case of a single bump of activity (in each population) above threshold over some interval (a_n, b_n), it is fast and accurate for studying activity bumps. If the activity is not a *single* superthreshold bump, the assumptions on the integral in the numerical scheme break down, and we instead approximate the integral term by a Riemann sum. Simulations were performed with 1001–20001 spatial gridpoints and time step $\Delta t \approx 10^{-2}$ to 10^{-4}.

Numerical simulations of the allotopic bump (as well as the allotopic and antisyntopic periodic bumps in section 2.2) are sensitive to the weak interlayer connections at increasingly large spatial offsets. The numerical scheme using the Riemann sum requires a high number of grid points to resolve the numeric simulations accurately enough to match the expected solution predicted by the analysis. In particular, when the spatial offset in the allotopic bump is sufficiently large, the bumps can become pinned at an incorrect spatial location. Furthermore, keeping system parameters fixed and choosing initial conditions as a localized bump in each layer with different spatial offsets on different simulation runs, the activity bumps in each layer can become pinned at different spatial locations despite lack of variation in the system parameters. Discretizations of 15000 gridpoints or more were required to alleviate the undesired pinning and ensure that the activity bumps approach the appropriate stationary allotopic bump in simulations using the Riemann sum.

Conversely, using the numerical scheme involving the antiderivative (56), spatial grids of 1000 points were often sufficient to obtain the solution predicted by the analysis.

REFERENCES

[1] S. AMARI, *Dynamics of pattern formation in lateral inhibition type neural fields*, Biol. Cybernet., 27 (1977), pp. 77–87.

[2] M. ARGENTINA AND P. COULLET, *Andronov bifurcation and sea-shell patterns*, in Pattern Formation in Biology, Vision and Dynamics, A. Carbone, M. Gromov, and Prusinkiewicz, eds., World Scientific, Singapore, 2000, pp. 133–144.

[3] M. ARGENTINA, O. RUDZICK, AND M. G. VELARDE, *On the back-firing instability*, Chaos, 14 (2004), pp. 777–783.

[4] S. ARDID, X.-J. WANG, AND A. COMPTE, *An integrated microcircuit model of attentional processing in the neocortex*, J. Neurosci., 27 (2007), pp. 8486–8495.

[5] F. G. ASHBY, S. W. ELL, V. V. VALENTIN, AND M. B. CASALE, *FROST: A distributed neurocomputational model of working memory maintenance*, J. Cognitive Neurosci., 17 (2005), pp. 1728–1743.

[6] R. BEN-YISHAI, D. HANSEL, AND H. SOMPOLINSKY, *Traveling waves and the processing of weakly tuned inputs in a cortical network module*, J. Comput. Neurosci., 4 (1997), pp. 57–77.

[7] P. BLOMQUIST, J. WYLLER, AND G. T. EINEVOLL, *Localized activity patterns in two-population neuronal networks*, Phys. D, 206 (2005), pp. 180–212.

[8] P. C. BRESSLOFF, J. D. COWAN, M. GOLUBITSKY, P. J. THOMAS, AND M. WIENER, *Geometric visual hallucinations, Euclidean symmetry and the functional architecture of striate cortex*, Philos. Trans. Roy. Soc. B., 40 (2001), pp. 299–330.

[9] P. C. BRESSLOFF AND J. D. COWAN, *An amplitude equation approach to contextual effects in visual cortex*, Neural Comput., 14 (2002), pp. 493–525.

[10] P. C. BRESSLOFF AND M. A. WEBBER, *Neural field model of binocular rivalry waves*, J. Comput. Neurosci., 32 (2011), pp. 233–252.

[11] M. V. CHAFEE AND P. S. GOLDMAN-RAKIC, *Matching patterns of activity in primate prefrontal area 8a and parietal area 7ip neurons during a spatial working memory task*, J. Neurophysiol., 79 (1998), pp. 2919–2940.

[12] C. CONSTANTINIDIS AND M. A. STEINMETZ, *Neuronal activity in posterior parietal area 7a during the delay periods of a spatial memory task*, J. Neurophysiol., 76 (1996), pp. 1352–1355.

[13] S. COOMBES, *Waves, bumps, and patterns in neural field theories*, Biol. Cybernet., 93 (2005), pp. 91–108.

[14] S. COOMBES AND M. R. OWEN, *Bumps, breathers, and waves in a neural network with spike frequency adaptation*, Phys. Rev. Let., 94 (2005), 148102.

[15] S. COOMBES AND M. OWEN, *Exotic dynamics in a firing rate model of neural tissue with threshold accommodation*, in Fluids and Waves: Recent Trends in Applied Analysis, F. Botelho, T. Hagen, and J. Jamison, eds., Contemp. Math. 440, AMS, Providence, RI, 2007, pp. 123–144.

[16] S. COOMBES AND C. R. LAING, *Instabilities in threshold-diffusion equations with delay*, Phys. D, 238 (2009), pp. 264–272.

[17] G. B. ERMENTROUT, *Neural networks as spatial pattern forming systems*, Rep. Progr. Phys., 61 (1998), pp. 353–430.

[18] G. B. ERMENTROUT AND J. D. COWAN, *Temporal oscillations in neuronal nets*, J. Math. Biol., 7 (1979), pp. 265–280.

[19] G. B. ERMENTROUT AND J. D. COWAN, *Large scale spatially organized activity in neural nets*, SIAM J. Appl. Math., 38 (1980), pp. 1–21.

[20] G. B. ERMENTROUT AND J. D. COWAN, *Secondary bifurcation in neuronal nets*, SIAM J. Appl. Math., 39 (1980), pp. 323–340.

[21] S. E. FOLIAS, *Nonlinear analysis of breathing pulses in an synaptically coupled neural network*, SIAM J. Appl. Dyn. Syst., 10 (2011), pp. 744–787.

[22] S. E. FOLIAS AND P. C. BRESSLOFF, *Breathing pulses in an excitatory neural network*, SIAM J. Appl. Dyn. Syst., 3 (2004), pp. 378–407.

[23] S. E. FOLIAS AND P. C. BRESSLOFF, *Breathers in two-dimensional excitable neural media*, Phys. Rev. Lett., 95 (2005), 208107.

[24] S. E. FOLIAS AND G. B. ERMENTROUT, *New patterns of activity in a pair of interacting E-I neural fields*, Phys. Rev. Lett., 107 (2011), 228103.

[25] S. Funahashi, C. J. Bruce, and P. S. Goldman-Rakic, *Mnemonic coding of visual space in the monkey's dorsolateral prefrontal cortex*, J. Neurophysiol., 61 (1989), pp. 331–349.

[26] P. S. Goldman-Rakic, *Cellular basis of working memory*, Neuron, 14 (1995), pp. 477–485.

[27] J. M. Fuster and G. E. Alexander, *Neuron activity related to short-term memory*, Science, 173 (1971), pp. 652–654.

[28] J. M. Fuster and G. E. Alexander, *Firing changes in cells of the nucleus medialis dorsalis associated with delayed response behavior*, Brain Res., 61 (1973), pp. 79–91.

[29] G. Gordh, G. Gordh, and D. Headrick, *A Dictionary of Entomology*, CABI Publishing, Cambridge, UK, 2001.

[30] D. Hansel and H. Sompolinsky, *Modeling feature selectivity in local cortical circuits*, in Methods in Neuronal Modeling: From Ions to Networks, 2nd ed., C. Koch and I. Segev, eds., MIT Press, Cambridge, MA, 1998.

[31] A Hutt and N. Rougier, *Activity spread and breathers induced by finite transmission speeds in two-dimensional neural fields*, Phys. Rev. E, 82 (2010), 055701.

[32] Y. Hayase and T. Ohta, *Self-replicating pulses and Sierpinski gaskets in excitable media*, Phys. Rev. E, 62 (2000), pp. 5998–6003.

[33] O. Hikosaka, M. Sakamoto, and S. Usui, *Functional properties of monkey caudate neurons* III. *Activities related to expectation of target and reward*, J. Neurophysiol., 61 (1989), pp. 814–832.

[34] Z. Kilpatrick and P. C. Bressloff, *Binocular rivalry in a competitive neural network with synaptic depression*, SIAM J. Appl. Dyn. Syst., 9 (2010), pp. 1303–1347.

[35] K. Kishimoto and S. Amari, *Existence and stability of local excitations in homogeneous neural fields*, J. Math. Biol., 7 (1979), pp. 303–318.

[36] C. R. Laing and W. C. Troy, *Two-bump solutions of Amari-type models of neuronal pattern formation*, Phys. D, 178 (2003), pp. 190–218.

[37] C. R. Laing and W. C. Troy, *PDE methods for nonlocal models*, SIAM J. Appl. Dyn. Syst., 2 (2003), pp. 487–516.

[38] C. R. Laing, W. C. Troy, B. Gutkin, and G. B. Ermentrout, *Multiple bumps in a neuronal model of working memory*, SIAM J. Appl. Math., 63 (2002), pp. 62–97.

[39] I. K. M. Morton and J. M. Hall, *Concise Dictionary of Pharmacological Agents: Properties and Synonyms*, Kluwer Academic Publishers, Dordrecht, The Netherlands, 1999.

[40] H. Mushiake and P. L. Strick, *Pallidal neuron activity during sequential arm movements*, J. Neurophysiol., 74 (1995), pp. 2754–2758.

[41] D. J. Pinto, *Computational, Experimental, and Analytical Explorations of Neuronal Circuits in the Cerebral Cortex*, Ph.D. Thesis, Dept. of Mathematics, University of Pittsburgh, Pittsburgh, PA, 1997.

[42] D. J. Pinto and G. B. Ermentrout, *Spatially structured activity in synaptically coupled neuronal networks* II. *Lateral inhibition and standing pulses*, SIAM J. Appl. Math., 62 (2001), pp. 226–243.

[43] S. Verduzco-Flores, M. Bodner, B. Ermentrout, J. M. Fuster, and Y. Zhou, *Working memory cells' behavior may be explained by cross-regional networks with synaptic facilitation*, PLoS ONE, 4 (2009), e6399.

[44] H. R. Wilson and J. D. Cowan, *A mathematical theory of the functional dynamics of cortical and thalamic nervous tissue*, Kybernetik, 13 (1973), pp. 55–80.

[45] X. Xie, R. H. R. Hahnloser, and S. Seung, *Double-ring network model of the head-direction system*, Phys. Rev. E, 66 (2002), 041902.